Modelling the Evaporation of a Binary Droplet in a Well

SETH RICHARD PRICE

How to cite:

PRICE, SETH RICHARD (2023) Modelling the Evaporation of a Binary Droplet in a Well. Doctoral thesis, Durham University.

Modelling the Evaporation of a Binary Droplet in a Well

Seth Richard Price

Abstract

While the drying behaviour of sessile droplets has been extensively studied over the last 25 years, the evaporation of droplets from wells (DiWs) has largely been neglected, especially from a mathematical modelling standpoint. Understanding a drying DiW is both important for industrial processes (such as inkjet printing and, increasingly, the manufacture of organic displays) and an interesting problem in its own right as a natural progression from sessile droplets, and we still do not have a thorough theoretical description of their evaporation.

The main aim of this project was to build an understanding of pure and binary DiWs under the lubrication approximation by constructing a simple mathematical model for the evolution of their shape. We solved the resulting partial differential equations for droplet height and composition profile numerically using the Method of Lines. In the case of a pure droplet, we found that we could control the interface shape using a single parameter ($\mathcal{C}$) based on the capillary number; the more complex binary system required two new parameters governing evaporation and surface tension differences. Comparison to experimental data was improved with the inclusion of a dynamic evaporative flux for each component that depended on the their volume fraction distribution.

These simulations offer insight into the deposit that evaporating DiWs leave behind. We have shown that the smaller $\mathcal{C}$, the more likely the DiW will cause an undesirable ring stain, but this is suppressed in binary droplets in which the more volatile component has the lower surface tension.

Modelling the Evaporation of a Binary Droplet in a Well

Seth Richard Price

A Thesis presented for the degree of
Doctor of Philosophy

SOFI CDT
Department of Physics and Department of Chemistry
Durham University
United Kingdom
February 20, 2023

Contents

List of Figures

List of Symbols

In this thesis, we sometimes work with dimensional variables and sometimes with dimensionless variables. While we clearly denote dimensional variables with a circumflex (e.g., $\hat{r}$ for dimensional radial coordinate) in the main body of the thesis, in the List of Symbols we shall forgo this practice for the sake of brevity. Each symbol is therefore given in its nondimensional representation (i.e., hatless). The symbols are arranged according to order of appearance.

ε	Well aspect ratio
h_0	Well height
R	Cylindrical well radius
Re	Reynolds number
ρ	Pure liquid density
U	Typical vertical speed
μ	Pure liquid viscosity
Ca	Capillary number
σ	Pure liquid surface tension
$\mathcal{C}$	C-parameter
r	Radial coordinate
$\mathrm{E\ddot{o}}$	Eötvös number
$\Delta\rho$	Density difference between liquid and gas
g	Acceleration due to gravity
Ar	Archimedes number
c	Vapour concentration field
c_0	Saturation concentration of vapour in air
H	Relative humidity
∇	Del operator
J	Evaporative flux
t	Time
D	Diffusion coefficient of vapour in air
$\boldsymbol{n}$	Unit normal to the droplet-air interface
$\boldsymbol{u}_{\mathrm{gas}}$	Gas velocity
z	Vertical coordinate
μ_{mix}	Viscosity of a mixture
χ	Volume fraction of less volatile component
ξ	Volume fraction of more volatile component
c_p	Specific heat of the liquid
$\tilde{T}$	Temperature field
k_T	Thermal conductivity of the liquid
$\boldsymbol{u}$	Liquid velocity vector

u	Horizontal/radial component of velocity
w	Vertical component of velocity
p	Pressure in the liquid
$\boldsymbol{T}$	Stress tensor
κ	Interface curvature
h	Droplet height
$\boldsymbol{t}$	Unit tangent to the droplet-air interface
V_n	Normal velocity of the interface
q	Liquid flux
h^*	Initial height profile of the droplet
M_m^c	Molar mass of the liquid
c_∞	Vapour concentration at infinity
x	Horizontal coordinate (2D square well)
N	Number of discretisation points in simulation
Δr	Width of discrete regions in simulation
h_i	The ith height ODE
α_{er}	Parameter that describes the decrease in error as N increases
r_{td}	Radius at which droplet first touches down
d_{td}	First fitting parameter for touchdown relationship
k_{td}	Second fitting parameter for touchdown relationship
A_{td}	Third fitting parameter for touchdown relationship
t_{td}	Time at which droplet first touches down
E	Total evaporative flux from droplet
J_i	Evaporative flux of component i in the droplet
α	Evaporation difference parameter
$D_{\chi\xi}$	Diffusivity of components χ and ξ in air
σ_i	Surface tension of component i in the droplet
β	Surface tension difference parameter
D_l	Mutual diffusion coefficient of each component in the liquid
Pe	Péclet number
$\mathcal{M}$	Marangoni number
χ^*	Initial composition profile
χ_i	The ith composition ODE
k_{χ_0}	Critical parameter for large $\mathcal{C}$ height profile
γ	Viscosity difference parameter
D_i	Diffusivity of component i in air
Z	Nondimensionalised vertical coordinate in vapour phase
R_∞	Radius at which we impose the far-field boundary condition
$\mathcal{T}$	Triangulation of space for the finite element discretisation
$\triangle$	A triangle in the triangulation
η_j	Basis function for the j^{th} vertex of a triangle
δ_{jk}	Kronecker delta for indices j and k

N_{outer}	The number of points in the mesh outside the inner unit quarter circle
N_{in}	The number of points in the mesh inside the inner unit quarter circle
h_b	The base height solution used to analyse linear stability
χ_b	The base composition solution used to analyse linear stability
k	The wavenumber of an applied perturbation
ω	The growth parameter of an applied perturbation
t_*	The frozen time at which we conduct the linear stability analysis
δ_h	The amplitude of the applied height perturbation
δ_χ	The amplitude of the applied composition perturbation
θ	The azimuthal coordinate in a fully 3D model
$\bar{v}$	The height-averaged azimuthal velocity in a fully 3D model
v	The azimuthal velocity in a fully 3D model

Declaration

I declare that I myself have composed this thesis and no part of it has been submitted for a degree in any previous application. Except where I have properly cited or, in the case of unpublished experimental work, acknowledged, this thesis is entirely my own work.

Statement of Copyright

Acknowledgments

It should go without saying (although I am of course going to say it anyway) that I owe much gratitude to my supervisor, Prof. Colin Bain for the success of this project – for his experience and knowledge to encourage my better ideas, and patience and wisdom to lead me away from my worse ones. Colin welcomed me into his research group despite my being more theoretically minded and for that I am grateful. It would also have been impossible to even start my PhD work without the mathematical expertise of Prof. Chris Breward, who has been extremely generous with his time and offered me lots of guidance. This project has been part-funded by the EPSRC and by members of the Industry Club[1] and made possible by SOFI CDT, and I am hugely thankful for their financial, academic, and administrative support, which has given me the opportunity to pursue an enjoyable and rewarding doctorate in science.

Special thanks also to Prof. Halim Kusumaatmaja and Prof. Andrew Bayly, supervisors in Durham Physics Department and Leeds Engineering Department respectively, for their assistance and advice with more specific problems and helping me to come to a broader understanding of the topic.

Additionally, I am grateful to my fellow members of SOFI Cohort 5 for their friendship and solidarity – it was wonderful to make 20 new friends at the start of the PhD programme and since then it has been fun to share our research with one another, offer and receive feedback, and become the cohort beer pong doubles champion (cheers Jordan Hobbs). I'd also like to thank the Bain group in Durham, not least Zhida and Teresa for producing experimental data for me to analyse! And Stefan, who, even while writing his own thesis, read part of mine and gave me good advice. I must also acknowledge and thank Logan, who wishes he knew as much about physics as I do about theology, for his company and conversation in Durham and Hartlepool.

I am also very thankful to all my extended family, to my church families at St Nic's Durham, All Saints' Stranton, and St Peter's Bentley for their prayers and support, and to Durham City Hockey Club for our unbeaten season.

Lastly, I would like to offer my most heartfelt thanks to my family for their unwavering love and care for me while I have been completing this PhD. To Finn, because of his companionship in our year in Durham together; to Milly, because of her kind words and visits to Doncaster; to my Mum, because she is my biggest fan; and to my Dad, because our Thursday morning conversations sustained me in some of the more challenging moments; to Jon, Helen, and Laura, who often provided me with welcome distractions of football, live rugby, and language challenges; to all of these for their prayers.

---

[1] specifically in Evaporative Drying of Droplets and the Formation of Micro-structured and Functional Particles and Films.

Final and special thanks go to Rachel, my wife. About halfway through the PhD she finally clocked that the application of my work was **not** about droplets evaporating from TV screens *while they were in use*, rather that it was to do with their manufacture. Since that lightbulb moment, she has been positively enthusiastic to explain my work at weddings, parties, and friendship gatherings in order to lift the responsibility from me. Indeed, alleviating the inevitable burdens of such a significant and demanding piece of work has been proven to be one of her many skills over the last four years. I would not have had a hope of doing it without her.
In and through all this I'm thankful to our creator God, of whose intricate creation it has been my delight to explore a little corner over the past four years.

For he draws up the drops of water…

Job 36:27

Chapter 1

Introduction

During the course of this PhD I have often been asked to describe my research to the well-meaning lay-person, who may let slip that they dropped physics and chemistry “as soon as possible at school”. I proceed to tell them that my aim is to model and simulate the evaporation of a droplet in a well (DiW) mathematically, to probe the processes and patterns involved in the formation of somewhat unexpected droplet shapes, and to build an understanding to the point at which I can make predictions of such droplets in the real world. The wittiest and boldest of them have, on occasion, retorted that “it’s like watching paint dry then?”.

Far from it! But the onus is on the PhD student to prove the value of his own work to the lay-listener. So I might challenge my conversation partner to, next time she has a coffee, intentionally spill a drop on the table and let it dry; we should be surprised at the dense, brown outline it leaves on her table. We physicists and chemists know this phenomenon as Deegan’s coffee ring [4]. This specific example is well understood today, but to what extent can we use to it to understand droplets of various liquids evaporating from wells? And what if they’re very thin and several orders of magnitude smaller than even an espresso?

I may ask whether she has a modern smartphone with an organic light emitting diode (OLED) display – there has been interest in recent years in printing active materials onto OLED displays to avoid some of the problems associated with vacuum-coating [3, 5]. If I simply reconceptualise my wells as pixels of a screen I can begin to ask whether there’s any way of controlling the behaviour of the droplet as it dries in a pixel – can I isolate the variables that make it evaporate more uniformly or more quickly?

Having been cornered with these conversations at a number of weddings, another illustration I choose to deploy is that of wine – giving me an excuse to partially fill my glass once more. Wine (in fact any alcoholic drink) in a glass will exhibit the Marangoni effect manifesting in ‘tears of wine’ [6]; an imbalance in surface tension due to the alcohol-water mixture provokes liquid at the edge to climb the inside of the glass and visibly drop back down under gravity. The Marangoni effect emerges in droplets composed of two or more liquids – what about the evaporation of binary droplets from wells? What impact do surface tension gradients have on the droplet as it dries?

In summary, this research project is a mathematical and computational investigation into the evaporation of picolitre-sized droplets[1] from thin cavities. I am primarily interested in the shape of the droplet–air interface as it evaporates, specifically the complex and mutually dependent roles that a number of fluid mechanics variables play in the droplet's behaviour. This study departs from extensive existing research on sessile droplets – much has already been said about Deegan's coffee-ring effect and other observable drying patterns [7, 8], pinned and moving contact lines [9, 10, 11], the evaporative flux of sessile droplets [12, 13, 14], computational simulations of evaporating thin films [15, 16], and the impact of Marangoni effects [7, 17, 18] – to look at the comparatively less researched area of printed droplets evaporating from wells.

This is not to say that no research has been performed in this area. This study sits upon previous work on experimental techniques for investigating droplets in wells [19, 20], the consequences of contact line pinning [21, 22] and Marangoni forces [23], as well as some theoretical studies on droplets in different shaped wells [1, 24], with a variety of evaporation models [25], and a few instances of joint experimental and theoretical work [3] that intend to create a complete mathematical model to compare with real-world results.

The first aim of this project is to build a simple model for the evolution of a tiny, pure droplet evaporating in a well and to investigate its behaviour under variations in certain key parameters. It will be important to demonstrate the impact of surface tension, viscosity, evaporative flux, and well geometry on the shape of the droplet-air interface, its touchdown, and the fluid velocity profile inside the droplet. Critically, I will also have the opportunity to compare the mathematical model to experimental data and qualify the predictive power of the model. We shall see that the pure model is able to produce three types of droplet shape, two of which have not yet been observed in numerical works. These two new shapes are known to appear experimentally and in industrial applications, but have not been studied theoretically yet.

Although useful for certain industrial applications, I will not explicitly attempt to model the sedimentation of solid or colloidal material suspended in a pure droplet as it dries. However it will be interesting to explore droplets composed of two liquids, so-called binary droplets. Binary droplets open the door to Marangoni forces, due to the surface tension gradients inherent to fluid mixtures. We will see that simply adding a second liquid component will complexify the system considerably, changing the drying shape, droplet curvature, and velocity profile evolution. I will demonstrate that the binary model has the capacity to both suppress and enhance dimple shapes via Marangoni forces, which has not been shown before from a theoretical or numerical point of view.

I will write in more detail about evaporation rate in chapter 2, but have already alluded to the uncertainty about the evaporative flux from a droplet inscribed in a well compared to one sessile on a substrate. This project will permit some exploration into models for and assumptions about the evaporation rate and its variation across the surface of a droplet. It is well understood by now that diffusion-limited evaporation is a solution to Fick's law for the vapour concentration (itself dependent on a mixed boundary condition expression of Poisson's equation) at the surface of

---

[1] Although we work in non-dimensional space, we shall later apply the lubrication approximation and neglect gravity, both of which impose upper limits on the size of the droplet. Moreover, we will make comparisons with experimental data taken from picolitre-sized droplets.

the droplet; I will attempt to compare some of the analytical approximations for evaporation with simulated solutions.

Finally, having been interested in a colleague's unexpected discoveries while performing an evaporation experiment, I will begin to investigate the stability of the droplet under a small asymmetric perturbation, analysing the conditions under which it grows and shrinks in order to determine whether certain systems will become unstable. This will be relatively easy for a two-dimensional droplet in a square well, but will prove much harder for a full three-dimensional droplet in a cylindrical well, the model for which includes proper treatment in all three cylindrical coordinates and whose simulation is beyond the scope of this project. Despite this, we will see some interesting results in the 2D cartesian case that may give us some useful qualitative information.

The main practical application of this field of research is inkjet printing. Consider a scenario in which we want to deposit a layer of material into a small cavity with a desired distribution: an efficient method is to spray a liquid containing a solution of the deposit into the cavities such that the liquid evaporates from them and leaves behind a desired thin layer. While vacuum-coating methods can sometimes also be used to achieve this, they do not work well for many materials (particularly larger molecules) [26] and can also encounter technical problems [27] that inhibit the ability to scale the process up (usually to do with the mask that vacuum coating requires). Inkjet printing, by contrast, can be used to print with polymers and other organic molecules, has no need of a mask, and can be scaled up much more efficiently [26, 28, 29, 30]. One of the fastest accelerating industrial applications of inkjet printing in recent years is in the manufacture of the aforementioned OLED display [5, 29]; the device architectures of all types of OLED displays comprise several different layers of active materials, some of which (depending on the OLED type) can now be inkjet printed into pixels in the substrate.

From an industrial point of view, it is very important to understand the behaviour of the droplets evaporating from the pixels. It is valuable to be able to predict and control the deposit distribution in the well – often a uniform deposit is desirable; that is, it is necessary to be able to suppress Deegan's coffee-ring effect in a well [31, 32]. Despite the significance of this understanding, there are no complete mathematical models describing this problem in the literature, except for the study by D'Ambrosio *et al* [3], in which they treat the capillary number as small. In this thesis, therefore, one of my aims is to build a predictive model for the behaviour of pure droplets as they evaporate from pixels of different shapes and to investigate the conditions – specifically variation of the capillary number and well geometry – under which the coffee-ring effect can be suppressed, enhanced, or otherwise altered. I will extend this analysis to binary droplets, exploring the role of the solutal Marangoni effect in the pixel deposit; crucially, we will ask whether the Marangoni effect has the ability to eliminate industrially undesirable deposit features in a pixel.

Beyond industrial and practical applications, there remain more fundamental questions about the predictive capabilities of lubrication models applied specifically to DiWs. To what extent are we able to represent an experimental droplet accurately? Using a simple mathematical model, is our analysis restricted to generic, qualitative features, or can we have success in reproducing droplet shapes? Can we go one step further and design a quantitatively predictive model for DiWs?

The main result of this work has been the construction of a basic model that qualitatively describes what we observe of droplets evaporating from wells: it can, through the control of a single parameter (quantifying the surface tension, viscosity, evaporation rate, and well geometry), adjust the shape of a droplet from printing to touchdown and can accurately reproduce both the W- and U-shaped droplets we see in experiments. Extending it to include the consequences of binary solvents leads to more exotic and complex behaviour under the control of two more parameters (quantifying the evaporation rate and surface tension differences respectively).

In chapter 2, we offer a review of the literature on the evaporation of droplets: an overview of our understanding of sessile droplets with pinned or unpinned contact lines; a more comprehensive analysis of droplets in cavities and the state of both the experimental and theoretical work on their evaporation; the Marangoni effect in droplets (due to both temperature variations and mixed composition); the discussion in the literature about the evaporative flux; and numerical methods for solving thin fluid film type problems.

Chapter 3 concerns the behaviour of the pure droplet in my simulation. We set up the problem mathematically and derive the equations for the cylindrical well before presenting the solution and exploring its behaviour. We will inspect the model over a few orders of magnitude of the key parameter, $\mathcal{C}$, and finally compare it to some experimental data.

In chapter 4, we begin to add complexity to the model in terms of binary droplets, again setting up the mathematical problem and deriving the relevant equations. We will investigate some important regions of the now three-dimensional parameter space, extracting useful information about the behaviour of the droplet, and then compare to experimental data again.

In chapter 5, the static evaporative flux will be replaced by a dynamic one – we will solve a two-sided model in order to better reflect the real evaporation of two components.

Chapter 6 will comprise a linear stability analysis of a 2D droplet in a square well and a short investigation into the corresponding stability analysis of a full 3D model.

In all these chapters, we will see that we are able to control the shape of a DiW and influence its deposit through just a few important parameters, including a total elimination of dimples with the Marangoni effect.

Chapter 2

Literature Review

2.1 Introduction

In this chapter we will get to grips with the literature in the field of droplet drying. Starting with general thin films (of which small droplets are an example) and sessile droplets, we will briefly take a dip into the wealth of research on basic drying principles and Deegan's pioneering work on the coffee-ring effect. After this, we will focus on the topics more specifically related to the work in this thesis, that is literature on the Marangoni effect, evaporative flux models, and droplets printed in wells. Finally, we will take a look at the most widely-used numerical methods for modelling problems of fluid dynamics, comparing their advantages and disadvantages in order to select the most appropriate for our purposes.

2.2 Sessile Droplets and Thin Films

The word 'sessile' is used to describe droplets that lie on a planar surface (literally a 'seated' droplet). Although in this work we will be studying the evolution of droplets printed in wells, the wealth of literature on sessile droplets can shed some light on how to proceed with DiWs, given they are somewhat more niche and less studied. In this section we shall take a look at the areas of similarity and key differences between sessile droplets and DiWs.

Oron *et al.*'s 1997 review on thin liquid films [33] discusses a number of topics that pertain to the evaporation of droplets. They describe lubrication theory (also called long-wave theory, but this specifically refers to the wavelengths of perturbations in a generic thin film; the word 'lubrication' is perhaps more relevant to our application), a theory of thin films pioneered by Osborne Reynolds in 1886 [34] in which the ratio of the vertical to horizontal length scales is taken to be very small,

$$\varepsilon = \frac{h_0}{R} << 1 \tag{2.1}$$

where h_0 is a characteristic height and R is a characteristic horizontal length (often a radius). Clearly, this approximation restricts a model to very thin films, in which the height is much smaller than the width of the system. In our derivation in the next chapter, we shall apply the lubrication approximation by neglecting terms in the parameter ε.

They describe two other important dimensionless quantities, the Reynolds number and the capillary number,

$$\mathrm{Re} = \frac{\rho U h_0}{\mu}\,, \tag{2.2}$$

$$\mathrm{Ca} = \frac{U\mu}{\sigma}\,, \tag{2.3}$$

where ρ is the liquid density, U is a characteristic velocity, μ is the liquid viscosity, and σ is the liquid surface tension.
They detail two possible lubrication approximations, but the latter is the important one; they take $\mathrm{Re} = O(\varepsilon)$ and $\mathrm{Ca}\,\varepsilon^{-3} = O(1)$ in order to preserve surface tension effects. This leads to a system in which the inertial terms in the Navier-Stokes equations are neglected and the thin film can be described instead by the Stokes equation; this limits the model to situations in which viscous forces dominate inertial forces.
This second approximation uses the reduced capillary number; in this work we will concern ourselves with its inverse

$$\mathcal{C} = \frac{\sigma\varepsilon^3}{\mu U}\,. \tag{2.4}$$

Applying the lubrication limit of small aspect ratio, ε, brings some aspects of sessile droplets and DiWs into similarity – on the scale of the horizontal length they now have the same vapour field and, therefore, evaporative flux [3] (see section 2.6).
At about the same time as Oron *et al.* published this review, Deegan *et al.* published a study into the so-called 'coffee-ring effect' (CRE) [4]. The work provoked an explosion of research into thin droplets, their evaporation, and their deposition patterns. The CRE comprises the concentration of deposited material from an evaporating sessile droplet along its perimeter, like the stain we get if we let a drop of coffee dry on a table (hence the name). Their proposed mechanism is that evaporating droplets feature a capillary flow born of an evaporative flux that diverges to infinity near the contact line; this capillary flow replenishes material lost from areas with a higher evaporation rate. Additionally, they argue that the droplet's contact line must be pinned for this to happen – otherwise the higher evaporation at the edge would just lead to a retraction of the contact line and outward capillary flows would be much weaker. Another group [35] studied the behaviour after the detachment of the contact line, finding that the CRE effectively stops when the contact line recedes. However, Deegan writing alone later [36] claims that sessile droplets cannot remain pinned by themselves; solid deposit at the contact line is actually a prerequisite for it to pin. He refers to this bootstrapping paradox as 'self-pinning' and promptly solves it by acknowledging preexisting imperfections on the substrate that allow pinning to take hold. This phenomenon differs from the pinning we observe in the DiW case, which mostly happens at the corner of the well. We will investigate more about well pinning and the conditions under which it occurs in section 2.3.

2.3 Droplets Evaporating from Wells

While sessile droplets have enjoyed, and continue to enjoy, a large amount of scientific attention over the last few decades, much less research has been done on droplets evaporating from wells. On the experimental side, early techniques for investigating droplets evaporating from small wells were developed by van den Doel and van Vliet in a cuboidal well [19] and by Rieger and the same authors in a cylindrical well [20]. They used interference-contrast microscopy to measure the depth of the liquid droplet dynamically and observed the evolution of the droplets from printing as a convex meniscus (noting that the fringes propagate towards the droplet centre) until it broke at the bottom of the well (noting that the fringe contrast increased as droplet height decreased).

In the second paper, they argue that, due to the impermeability of the substrate vertically and horizontally, the initial droplet behaves identically to an identical sessile droplet, provided that the droplet starts out life taller than the well. This leads to them accepting the Deegan/Popov evaporation model (see section 2.6) for droplets in a well; they proceed to show experimentally that, because of the linear relationship between evaporation rate and well radius, the evaporation process in a well is diffusion limited and Popov's evaporation rate is valid and independent of elapsed time over the duration of the evaporation. Moreover, they observed consistent contact line (well rim) pinning; these are two of the conditions stated by Deegan *et al.* [4, 12, 36] as being responsible for the formation of the ring stain. Additionally, they show that in their experiment (using a large piece of silicon as the substrate) evaporative cooling is negligible.

Chen *et al.* [37] performed experiments on nanolitre droplets in cylindrical wells, also observing strong pinning at the well edge as well as the evaporation rate's linear relationship with well radius. In a later paper [21] they demonstrate that the wettability of the substrate has a significant impact on the evolution of the droplet; wells made of hydrophilic material maintain the pin at the well lip, while droplets in hydrophobic wells run down the edge of the well. They show that the degree of this slip depends on the wettability contact angle of the material; the higher the contact angle, the more flat the droplet as it evaporated from the well (until touchdown, which is also delayed in more hydrophobic wells). Jung *et al.* [22] studied polymer solution droplets (more on droplets of binary composition in section 2.7) evaporating from cylindrical wells in order to remove some complications related to sessile droplets, namely the motion of the contact line. They studied the solid deposit left by the solution and found that solidification starts at the edge and propagates towards the centre. The conclusions of all these pieces of work are unanimous – the late-stage shape of the free surface determines the pattern of the deposit, with the initial touchdown point, critically, being the eventual location of highest density solid material [21, 22, 23, 37, 38].

Theoretical work on droplets evaporating from wells has also been done. Okuzono *et al.* [24] applied the lubrication approximation for a polymer solution droplet evaporating uniformly from a square well. They modelled the liquid alongside non-evaporative gel at the edges of the well and investigated the final deposit. They identified three different final shapes and categorised droplets into them as a phase space of the initial central height of the droplet and initial polymer concentration. The basin and crater shapes appeared in all cases, while large diffusion of the polymer was required to produce a mound shape – they note that this makes sense because diffusion tends to homogenise the polymer concentration field, whereas capillary flow causes an inhomogeneous distribution.

The shape of the well is another factor that has been shown to have an impact on the evolution of the droplet and its deposit. Eales *et al.* [1] simulated droplet evaporation from wells with soft bottom edges; they designed a substrate function with control over the trough depth and bank extent with variables X_1 and X_2 respectively,

$$h_{\text{sub}} = \begin{cases} X_1(\operatorname{arctanh}(r \tanh(1)))^{X_2} \ \text{ for } \ 0 \leq r < 1\,, \\ X_1 \ \text{ for } \ r \geq 1\,. \end{cases} \tag{2.5}$$

Figure 2.1 shows some variations of these shapes. They discovered that increasing either of these variables contributes towards the formation of a coffee ring, using a variable they call CR $= \frac{h_p}{h_c}$, the ratio of the depth at the droplet centre to the maximal liquid depth, as a proxy for magnitude of the CRE (also used in similar work on sessile droplets [39, 40]).

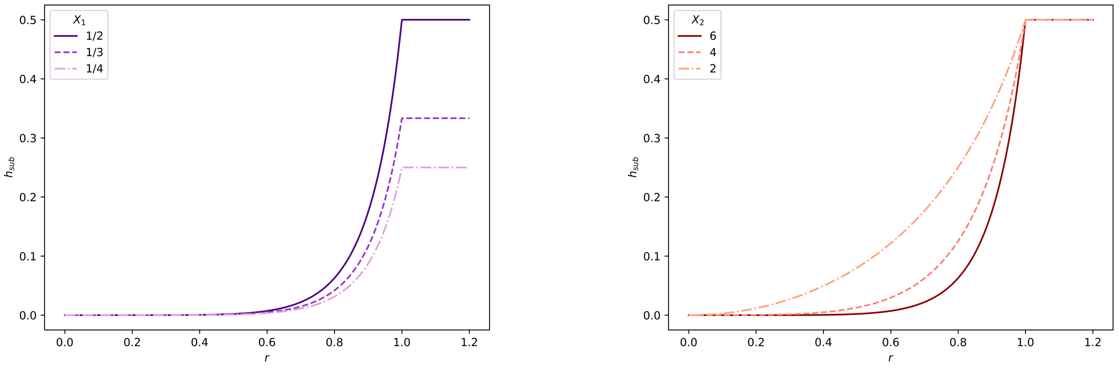

(a) Increasing parameter X_1 increases the trough depth.

(b) Decreasing parameter X_2 decreases the bank extent.

Figure 2.1: Examples of the substrates used in theoretical work by Eales *et al.* [1].

Their work goes some way to demonstrating the significant impact well geometry can have on the CRE, however it also highlights one of the principal challenges for a theorist investigating the CRE – that is, to move from a purely fluid dynamical model and understanding of a problem to a precise prediction of the solid deposit left behind by an evaporating droplet. This specific area of study is somewhat lacking in the literature; how can we use fluid dynamics to better quantify the magnitude of ring deposits? In section 2.7 we will learn more about the suppression of the CRE and its mechanisms and how we can use them to predict and study solid deposits.

Most recently, D'Ambrosio *et al.* investigated DiW evaporation in the limit of small capillary number [3]. In our work, we instead vary the capillary number over several orders of magnitude, finding the C-shaped droplet as in their paper, but also discovering two new shapes for DiWs: namely W- and U-shaped interfaces.

2.4 Droplet Size

The size of an evaporating droplet can have a large impact on its behaviour. One of the more intuitively obvious effects is that larger droplets are more influenced by gravity – the Eötvös (Bond) number quantifies this relationship,

$$\mathrm{E\ddot{o}} = \frac{\Delta\rho g R^2}{\sigma}, \tag{2.6}$$

where $\Delta\rho$ is the difference in density of the liquid and the gas, g is acceleration due to gravity, R is a characteristic length scale (in our case the radius of the well), and σ is the surface tension. However, some studies have recently challenged the exclusion of gravity from droplet models; Li *et al.* published a paper investigating the effect of gravity and evaporation in micro-litre binary droplets (sessile and pendant), concluding that gravitationally-induced "natural convection can readily dominate the flow" [41]. They argue that most studies disregard this effect because they assume a small Eötvös number automatically kills off all gravitational impact. Other papers come to similar conclusions [18, 42]; in all of them the mechanism for gravity-driven flow is the convection of components in a mixture due to their density differences. Therefore, while the Eötvös number is still relevant to describe the competition between gravity and surface tension (for example, the interface shape in all the above citations remains a spherical cap because Eö << 1), buoyancy forces can be described with a so-called Archimedes number,

$$\mathrm{Ar} = \frac{g h_0^3 \rho_0 \Delta\rho_m}{\mu}, \tag{2.7}$$

where h_0 is the characteristic height of the droplet, ρ_0 is a reference density, $\Delta\rho_m$ is the difference in density between the two components, and μ is the mixture viscosity. For very thin binary droplets, then, this is unlikely to be large enough that gravity play a significant role in the flow.

2.5 Flow Velocity

We have already seen (section 2.2) that Deegan *et al.* explained the CRE by invoking outward capillary flows; the flow field inside an evaporating droplet is critical to the drying process and, if we are able to acquire it, can be used as a predictive tool for dry deposits. Marín *et al.* showed that there is a sharp transition in the ordering of crystal deposits that occurs after a spike in flow velocity [43], which often takes place in the final moments of the process (they also coin the term 'rush-hour' to describe this effect in droplet drying). They explained this behaviour by recognising that the evaporation rate doesn't decrease even as the droplet gets very thin [13], meaning the outward radial capillary flow remains constant through a fast diminishing area [44].

Li *et al.* suggested that the final deposit is in part governed by the flow field [45] – they associated dramatic increases in flow speed with emergence of coffee-ring (or coffee-eye, depending on the direction of flow) deposits, with the particles often being drawn along the streamlines of high velocity to settle.

Ooi *et al.* described the typical flow conditions for the CRE: radially outward flow, speed is higher near the edge, and rush-hour occurs in the final stages of the evaporation [17]. They attempted to suppress the CRE by controlling their velocity fields; by including cellulose nanofibres (CNFs) they forced the fluid velocity to be higher in the centre of the droplet than at the edge and also managed to inhibit rush-hour. Although their study focuses on the large anisotropy of the CNFs, they frustratingly do not offer a robust mechanism for the change in flow due to the CNFs – they end by suggesting that the CNF concentration increased near the end of the drying, which formed a hydrophilic assembly and mechanically hindered the flow of liquid.

2.6 Evaporative Flux

It is common practice [9, 46, 47, 48, 49] in the study of lubrication-limited evaporation to invoke the argument that the vapour-phase relaxation timescale is much smaller than that for changes in droplet size, shape, or composition
In fact, Hu and Larson [9] argued that this ratio can be approximately expressed by $c_0(1-H)/\rho$, where c_0 is the saturation concentration of vapour in the gas and H is the relative humidity of ambient air. Since they were using water, they took $c_0 = 2.32 \times 10^{-5}$ g/cm^3, $H = 0.4$, and $\rho = 1$ g/cm^3, and showed that the diffusion timescale is on the order of 10^5 times smaller than the evaporation timescale. Therefore the vapour concentration field, $\hat{c}$, is considered a solution of the Laplace equation,

$$\hat{\nabla}^2 \hat{c} = 0\,, \tag{2.8}$$

rather than the time-dependent diffusion equation, with appropriate boundary conditions that linearise the droplet surface onto $z = 0$, send the concentration to zero in the far field, and do not permit vapour flux across the substrate. The evaporative flux is, by Fick's law, given as

$$\hat{J}(\hat{r}, \hat{t}) = -D\hat{\nabla}\hat{c} \cdot \hat{\boldsymbol{n}}\,, \tag{2.9}$$

where D is the diffusion coefficient of $\hat{c}$ in the gas and $\hat{\boldsymbol{n}}$ is the unit normal to the interface (circumflex denotes dimensional variables).
However, the approximation of a rapidly changing vapour field is not without controversy; it is not necessarily true that Hu and Larson's calculations hold in all scenarios. For example, although they show that the relaxation of the vapour phase is very fast in comparison to the evaporation of the droplet, it may not be so fast in comparison to the rate of change of spatial composition of binary droplets. Furthermore, Shahidzadeh-Bonn *et al.* hypothesised that buoyancy creates convection above an evaporating droplet whose vapour is less dense than air (e.g. water) [50]. As Dunn *et al.* point out [51], this model requires that one exchange the simple diffusion equation (equation 2.8) for a quasi-steady convection-diffusion equation

$$D\hat{\nabla}^2 \hat{c} = \hat{\boldsymbol{u}}_{\text{gas}} \cdot \hat{\nabla}\hat{c} \tag{2.10}$$

and the evaporative flux (equation 2.9) for an equation that accounts for gas/vapour velocity ($\hat{\boldsymbol{u}}_{\text{gas}}$)

$$\hat{J} = -D\hat{\nabla}\hat{c} \cdot \hat{\boldsymbol{n}} + (\hat{\boldsymbol{n}} \cdot \hat{\boldsymbol{u}}_{\text{gas}})\hat{c}\,. \tag{2.11}$$

Back with non-convective vapour transport, the analytical solution of equation 2.8 is highly non-trivial, requiring an analogy to the electrostatic potential of a charged conductor [4, 13] in the shape of the droplet plus its reflection in the substrate (to eliminate the substrate boundary conditions) and a transformation to toroidal coordinates in fully infinite space. This method results in a vapour field described (now nondimensionalised) by the equation [3]

$$c(r,z) = \frac{2}{\pi}\sin^{-1}\left(\frac{2}{\sqrt{(1+r)^2+z^2}+\sqrt{(1-r)^2+z^2}}\right), \tag{2.12}$$

which leads to the evaporative flux as used in Deegan's and Popov's works [4, 13], among others, for flat droplets,

$$\hat{J} = \frac{2}{\pi}\frac{D(c_0 - c_\infty)}{\sqrt{R^2-\hat{r}^2}}\,. \tag{2.13}$$

This form diverges at the contact line (in this work, the location of the well pin, $r = 1$), which is to be expected from an analogy to electrostatic potential at a sharp point; this is somewhat problematic when considering a sessile droplet with movable contact line, but we should recognise that the singularity is integrable and does not result in an infinite flux over the surface of the droplet. As Saxton *et al.* [49] note, however, it does engender an unphysical singularity in the height-averaged velocity at the contact line. Fischer [14] attempts to deal with this problem by introducing a new function and assuming exponential decay of evaporation near the contact line,

$$J = \frac{1}{h+K}\left(1 - e^{-A(1-r)^2}\right), \tag{2.14}$$

with the dependence on h and dimensionless constant K coming from work by Anderson [52]. A comparison between Deegan/Popov's (nondimensionalised) and Fischer's models is depicted in figure 2.2, with the parameters adjusted so their integrated flux over the surface of the droplet is the same.

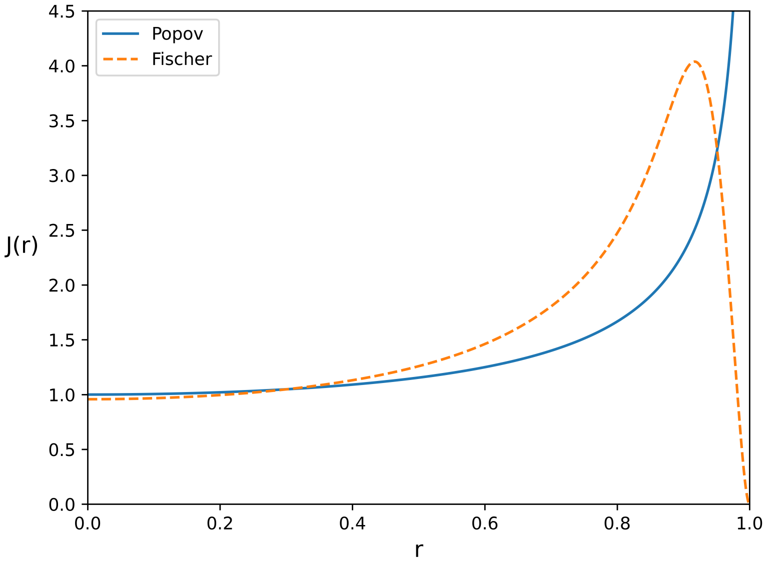

Figure 2.2: Evaporative flux models from Popov (blue) and Fischer (orange, dashed). Here $K = 0.044$, $A = 250$, and $h(r) = 1 - r^2$.

Saxton *et al.* [49] propose to address the issue with a 'kinetics-based evaporation model'; they assume that the vapour just above the droplet is not in equilibrium and mass flux through the interface can be described by the Hertz-Knudsen equation,

$$\hat{J} = M_m^c v_k (c_e - c_0)\,, \tag{2.15}$$

where M_m^c is the molar mass of the vapour, v_k is some velocity scale, c_e is the equilibrium vapour concentration, and c_0 is the vapour concentration at the droplet surface. They solve the Laplace equation while imposing a Neumann condition along the droplet surface instead of a Dirichlet condition, which leads to an evaporative flux that looks qualitatively similar to the Popov form, but with a finite value at $r = 1$, and the total mass flux depending on a dimensionless parameter they call the 'kinetic Péclet number', Pe_k.

They make sure to note that, given that the singularity is integrable, 'physically reasonable predictions for the evolution of the drop volume are obtained even without regularization of the mass-flux singularity'; that is, we should be more careful when performing calculations with the fluid velocity near the contact line, but problems concerning the height in general may be reasonable even with the Popov form and its singularity.

Other people have worked on problems with non-constant vapour concentration along the surface of the droplet too, particularly in the case of a spatially varying temperature. Work by Dunn *et al.* [46], Sefiane *et al.* [53], and Schofield *et al.* [54] are examples of this area of research, in which the constant Dirichlet boundary condition on $z = 0$ becomes a function of T or, in the latter case, a Robin boundary condition[1] dependent on T.

There are also a few works that investigate this same effect, but originating from multiple components [18, 55]. Pahlavan *et al.* [56] report theoretical and experimental results using binary sessile droplets with saturation concentration a function of χ, the species volume fraction in the droplet. This is used to explain the formation of flat pancake shapes and relaxation to spherical cap shapes that they observe in small multicomponent droplets.

2.7 Binary Mixtures and the Marangoni Effect

The Marangoni effect was first documented and explained by James Thompson in the 1850s as a 'curious' phenomenon observed on the surface of wine [57, 58] – in wine (other alcoholic drinks are available) the evaporation of alcohol leads to non-uniform surface tension and enables the liquid to crawl up the inside of the glass and it eventually drips back down after growing to a certain size. Italian physicist Carlo Marangoni studied the effects of surface tension gradients in general for his doctorate thesis [59], whence the phenomenon derives its name.

Until the mid 2000s a lot of research on Marangoni flows was concerned with thin films and pools (particularly spreading enhancement and inhibition [33, 60], Bénard convection [61, 62, 63] and special types of instability [64, 65]), though Marangoni effects in droplets had been studied somewhat (particularly due to non-isothermal phenomena occuring in evaporation or imposed from the environment [52, 66, 67] and experimental work mixing solvents [30]).

---

[1] a Robin condition is a linear combination of a Dirichlet and a Neumann condition

Hu and Larson were the first to derive and solve a model for the velocity field with thermal Marangoni stress in a sessile droplet [68]; they used finite element analysis (FEA) to determine the temperature gradient along the surface of a droplet and proceeded to find the coupled thermal and velocity fields, and also provided an analytical solution under the lubrication approximation. In their next paper published a year later [7], they conclude that Marangoni flows act to suppress the aforementioned droplet coffee-ring phenomenon in favour of a more uniform deposit, a desirable outcome for a wide variety of scientific and industrial applications [31, 69, 70]. The mechanism by which it does this, they argue, is that the surface tension gradients drive a 'recirculating flow' radially inward along the interface that 'plunges' surface particles down near the centre of the droplet, affording them a greater probability of adsorbing onto the substrate inside the contact line. This confirmed earlier research that suggested that Marangoni flows can influence the pattern of the dry deposit [71], and the suppression effect has been corroborated by many others since [23, 31, 69, 72].

CRE suppression is not the only feat the Marangoni effect is capable of, however – Hu and Larson also proposed the existence of reverse flows (that is, when Marangoni forces act to produce a flow radially outward along the interface) [68]. These were observed by Ristenpart *et al.* [8], who also established that the flow direction is determined by the ratio between droplet and substrate thermal conductivities, as well as the contact angle.

Van Gaalen *et al.* have published a number of papers in recent years on mathematical models of the Marangoni effect in macroscopic sessile droplets. They argue for a slip model (over a precursor film model) when Marangoni effects are present in a droplet with moving contact line [73], provide numerical results that show that strong evaporation and bulk diffusion (among other factors) counteract Marangoni flows [74], and compare solutal to thermal Marangoni effects, concluding that when both are included together Marangoni effects can be suppressed [75]. Diddens *et al.* [55] built a sophisticated numerical model for binary sessile droplets specifically, validating the use of the quasi-steady limit for vapour diffusion of a droplet mixture (see section 2.6 for more on evaporative flux) and reporting Marangoni induced shape deformation and the recirculating currents observed by experimentalists intending to suppress the CRE.

However, Marangoni-induced CRE suppression is not yet completely understood [31]. Despite a wealth of evidence that the Marangoni effect increases deposit uniformity, some authors report varying degrees of effectiveness. Kim *et al.* studied ethanol/water droplets from which the deposit was nonuniform, in spite of Marangoni forces [76]. They needed to enhance the Marangoni effect by adding surfactants and polymers in order to achieve a uniform deposit, though they also observed single malt whisky forming unprompted uniform circular deposits. Talbot *et al.* found ring stains from binary droplets due to capillary forces outlasting temporary Marangoni forces [77, 78] and also cases in which the Marangoni effect resulted in a central blob stain instead of a contact line ring [79].

Some work on binary droplets in wells has been done, notably by Jung *et al.* [22] and Kajiya *et al.* [23], see section 2.3 for details about how Jung *et al.*'s work relates to wells specifically. The former studied straightforward polymer solution, the latter surfactant-enriched polymer solution; both report Marangoni effects that act to flatten the droplet profile, the latter stronger effects that depended on the concentration and type of surfactant used (though the droplet surface is affected by even a small amount of surfactant). Their work shows that coffee-ring suppression by Marangoni flows is not limited to sessile droplets.

We are able to offer new theoretical and numerical evidence that support these conclusions; we shall demonstrate later that Marangoni forces can indeed act to reduce the conditions associated with the CRE. We will also show, however, that the Marangoni effect does not solely function to flatten interfaces, but can be used to have finer control over their shapes in both directions.

In this section we have seen that much research has already been undertaken into the nature of the Marangoni effect and its application in reducing the impact of the CRE (particularly for sessile droplets). However, nobody has attempted to provide a universal predictive mechanism for the suppression of the CRE. Instead, experiments often identify relevant and successful, yet isolated, incidences of ring stain suppression due to Marangoni forces, while theorists are hindered from developing a complete mathematical model for it by the CRE proxy problem we encountered in section 2.3. We can be certain that the Marangoni effect leads to a more uniform deposit under specific conditions and that it has something to do with the recirculating flows that it produces; beyond that more investigation is required.

Dealing with binary mixtures raises problems unrelated to the Marangoni effect. Although the viscosities of liquids are readily available (within reason), it is not entirely clear how to determine the viscosity of a general mixture of two (or more) liquids.

The majority of researchers studying binary alcohol droplets take the total viscosity to be a linear function of the volume fraction [40, 56],

$$\mu_{\text{mix}} = \mu_\chi \chi + \mu_\xi \xi \, , \tag{2.16}$$

where χ and ξ represent the volume fractions of the two liquids and μ_i their respective viscosities. Another common model for mixture viscosity is the Arrhenius relation [80] (or Grunberg-Nissan model [81], if you include their small correction factor) using logarithms:

$$\ln\mu_{\text{mix}} = \chi \ln\mu_\chi + \xi \ln\mu_\xi \, ; \tag{2.17}$$

both these models work well if the two components have similar molar masses. Katti *et al.* proposed a slightly more sophisticated model using the partial molar volume of each component, V_l,

$$\ln(\mu_{\text{mix}} V_{l\,\text{mix}}) = \chi \ln(\mu_\chi V_{l\,\chi}) + \xi \ln(\mu_\xi V_{l\,\xi}) \, . \tag{2.18}$$

This mathematical uncertainty has not deterred experimental researchers from investigating the effect of variable viscosity on drying droplets. Both Shi *et al.* [31] and Talbot *et al.* [32] assert that viscosity changes in aqueous polymer solution droplets are too small to suppress the CRE. The elastic properties of complex fluids are apparently more significant, however: ‘sol-gel’ transitions, in which a stable colloidal suspensions start exhibiting elastic behaviour, have been shown to at least reduce radial convection [82, 83] and, in some well controlled cases, completely get rid of the ring stain [32, 79]. In these latter examples, the authors ensured that the droplet’s gelation, which starts at the contact line and moves inwards, be perfectly timed in order to suppress the CRE and also prevent a central dome deposit.

2.8 Thermal Effects

For any theoretical study intending to model droplet evaporation the theoretician must decide whether to include thermal effect or not. A large body of work opts not to [3, 4, 12, 36, 84, 85, 86]; Eggers and Pismen articulate this decision with reference to local thermodynamic equilibrium: they argue that in the case of diffusion-limited evaporation and fast thermal relaxation, the droplet-substrate system has a constant and uniform temperature [15].

Other researchers choose to include an analysis of heat transfer between the substrate and the droplet. Most notably, Hu and Larson state that many experiments exhibit strong evidence of thermal-affected flow, thereby justifying the inclusion of an equation for the conservation of energy [68],

$$\rho c_p\Big(\frac{\partial \tilde{T}}{\partial t} + \hat{\boldsymbol{u}} \cdot \hat{\nabla}\tilde{T}\Big) + k_T \hat{\nabla}^2 \tilde{T} = 0\,, \tag{2.19}$$

where c_p is the specific heat, k_T the thermal conductivity, and $\tilde{T}$ is the temperature field (with tilde to prevent confusion with time scale factor later). In fact, in their particular case, they showed that their Stanton number was sufficiently large that they could approximate this equation with a simple Laplace equation for temperature,

$$\hat{\nabla}^2 \tilde{T} = 0\,. \tag{2.20}$$

They fix the temperature as a constant on the substrate as a bottom boundary condition and no conductive or convective heat loss across the droplet-air interface. Many of these works concern themselves with phenomena such as thermal Marangoni effects (as in Hu and Larson's paper, see section 2.7 for more) [8, 87, 88] or thermally-driven evaporation [52, 89, 90].

A central intention of this work is to replicate numerically a simple experiment in which there is no indication of large temperature gradients between substrate and droplet. Although thermal effects will, no doubt, be present, we will follow the former assumption (constant temperature) throughout.

2.9 Theoretical and Numerical Methods

There are many methods that theorists use to attack problems of thin-film fluid dynamics.

2.9.1 Method of Lines (MoL)

Partial differential equations (PDEs), like lubrication equations derived from the Navier-Stokes equations can be very difficult to solve. In the method of lines, the intention is to discretise all the dimensions (usually the spatial ones) but one (usually time) of an equation, leaving a number of ordinary differential equations (ODEs). The derivatives in the PDE are often discretised by a finite difference approximation. The ODEs can then be solved numerically, each solution corresponding to the evolution of the desired variable at a spatial location in the system. This is an attractive feature of the method because of the wealth of existing numerical methods for solving ODEs. It is also flexible and versatile – it is easy to deal with complicated and nonlinear boundary/initial conditions in MoL [91] – and, thanks to its separation of space and time, it can be applied with numerical stability to many kinds of problems [92]. Furthermore, it is computationally efficient (provided the programmer picks the right ODE solver) – it requires significantly less computational effort than, for example, techniques that keep track of the location and momentum of many particles.

Droplet evaporation problems have been solved in the past using MoL. Fischer (also mentioned in section 2.6) investigated sessile droplets under the lubrication approximation, modelling their evolution with a PDE for height and solving it with MoL, using second-order centred difference approximations to the derivatives. He set the capillary number at a relatively low Ca = 0.01 and measured the resulting flow fields he acquired, noting their tendency to point towards the contact line (see section 2.2 for Deegan's explanation of this phenomenon). Another work is that of Maki *et al.*, who also numerically solved the lubrication equation for a sessile droplet [93]. Their droplets carried a colloidal suspension; while the droplet profile was indeed solved with MoL, the particle transport required a more sophisticated approach due to a moving domain – for this they employed the method of moving overset grids.

2.9.2 Lattice Boltzmann Method (LBM)

The Lattice Boltzmann Method imagines fluid 'particles' to lie on a regular lattice and evolves the system timestep by timestep, applying acceleration to particles based on the forces (collisions, streaming) present. It is used widely in fluid dynamics problems, including the simulation of droplets. This is partly due to its ability to bridge the gap between micro- and macroscopic physics through retention of molecular-scale probability distributions while including body forces and ensuring mass and momentum are conserved over large systems (certainly better and faster than molecular dynamics simulations [94]). It is also because the LBM has been shown to be able to cope with complex systems – immiscible binary fluids [95], flow in porous media [96], and multiphase simulation [97] are just some of the proven applications of the LBM that are relevant to droplets. Some pieces of LBM work on droplets specifically include sessile/patterned substrate evaporation [98, 99], contact-line hysteresis [100], gas-propelled spreading [101], and collision with a scratch by Al-Ghaithi *et al.* [102].

One of the downsides to LBMs is the computational power required - it can be expensive to keep track of the large number of particles that the simulation requires; this is especially true when dealing with some kinds of thin-film multiphase systems because of the over-resolution thanks to the uniform mesh.

2.9.3 Finite Element Method (FEM)

The FEM is another method often used in problems to do with fluid dynamics. The solution space is subdivided into small shapes (finite elements), often triangles or quadrilaterals, that vary in their exact size and shape in order to represent geometries of complex objects accurately. PDEs can be solved by determining weak formulations of the governing equations: the simulator may define a set of test functions for which the equations weakly hold, meaning they do not necessarily hold universally. The solution is then a finite linear sum of these functions. One of the draws of FEM in droplet simulations is that it can be employed with invoking the lubrication equation; Diddens explains that this enables him to extend his model to droplets with large contact angles [103]. It is a versatile and powerful technique and can keep track of many different quantities simultaneously while evaporating the droplet, such as heat and mass transfer [104], deformation and elasticity of the substrate [105], and humidity in the gas phase [106].

Another of its applications, which we will find particularly helpful, is in solving elliptic boundary value problems with mixed boundary conditions. Alberty *et al.* offer a useful FEM implementation for solving the heat (and of course Poisson's, and Laplace's, etc.) equation, among other, more complicated PDEs [107]. They prove it to be flexible and fast to use FEM for these kinds of systems – it can easily be adapted for different geometries and a variety of (Dirichlet, Neumann, Robin, mixed) boundary conditions.

COMSOL is a popular finite element software; it is often been used to solve the vapour part of the two-sided droplet-gas problem [51, 108, 109, 110].

2.9.4 Molecular Dynamics (MD)

Despite its computational cost and almost reductive simplicity, MD has remained an option for simulating certain fluid dynamical processes since the 1990s. This is probably, in fact, because the concept is so fundamental – the simulator takes a certain number of particles (representing molecules or even atoms) in a certain shape, applies an appropriate potential, and allows them to interact. It is clear that MD simulations become increasingly expensive with more particles; as computational power has increased over the last few decades so too has MD system complexity. A few examples of droplet evaporation demonstrate this clearly: in 1996, Long *et al.* reported a MD simulation comprising 2,048 atoms [111]; just seven years later in 2003, Consolini *et al.* performed one with 5,662 atoms [112]; and in 2019, Xiao *et al.* managed to model a system with 106,143 atoms. All of these three examples, and most other droplet MD processes, are evaporations of spherical droplets suspended in a gas phase; that is they do not involve a substrate or any kind of mixed boundary conditions. This kind of simulation can be challenging, especially in three-dimensions, because surface tension can be difficult to include [113] – a simulator would normally choose a force field to describe behaviour in the bulk rather than at the surface. A notable example, however, is work by Zhang *et al.* [114], who built a three-phase MD simulation of a droplet in vapour (27,000 atoms combined) evaporating from a substrate ($8 \times 5{,}000$ atoms). They wanted to investigate the effect of substrate heating on the evaporation and found that they could control the evaporative mass flux by changing the hydrophilicity of the substrate.

All of the above works concern very small droplets – the largest, with $\sim 10^5$ atoms, could only model a droplet with a diameter of 43 nm. This is a common feature of MD simulations, because in each case the simulator must keep track of the properties of individual atoms/molecules and therefore the computational cost is prohibitive to large systems. LBMs are preferred in general when dealing with mesoscopic fluid physics (see section 2.9.2).

2.9.5 Direct Numerical Simulations (DNS) and Volume of Fluid (VoF)

DNS and VoF are often discussed together because they are often implemented together too; VoF is not so much a standalone algorithm, rather it is an interface advection scheme, tracking the features of interfaces in the simulation, while DNS is a method for finding a numerical solution to the Navier-Stokes equations. It is often used to produce complete, exact simulations of flows, even with a high degree of turbulence; for this reason DNS is very costly and is not used for general purpose [115].

VoF tracks an interface by measuring the amount of substance in a mesh cell – when the fraction function is zero the cell is empty (or full of gas phase, depending on how you look at it), when it is one the cell is full. Any value in-between indicates that the cell contains a part of the interface; these cells can be refined to increase accuracy in determining the properties of the interface. This is illustrated in figure 2.3.

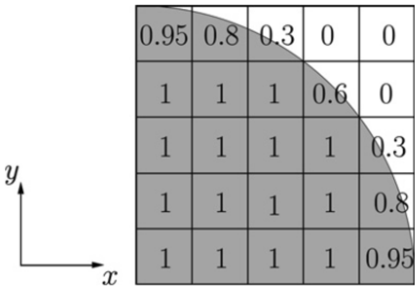

Figure 2.3: Illustration of VoF interface tracking from work by Schlottke and Wiegand [2].

Research that uses DNS to simulate evaporating droplets used to focus on turbulent (or otherwise highly complex) flow; to use it on a small droplet with low Reynolds number would be a bit like using the James Webb to spy on your neighbours. Relevant pieces of older work include research by Schlottke and Wiegand, who use DNS and VoF to model an evaporating droplet of one phase in a region of high flow of another phase (air) [2]. They successfully modelled droplets with low and high evaporation rates, including the Stefan flow related to the moving interface, and identified complex flows in three dimensions in the wake of the droplet.

However, in recent years DNS has been applied to a larger variety of droplet problems, including in a paper by Sáenz *et al.* on sessile evaporation in three dimensions, which picks up on internal flow vortices [116], one by Reutzsch *et al.*, which applies DNS to evaporating droplets in a large number of ambient conditions to simulate many aspects of the droplet's evaporation to a high degree of accuracy, including high evaporation rates, supercooling, and oscillating droplets [117], and work by Shang *et al.* with a droplet-vapour solver that reveals "minute details of the complex characteristics associated with droplet evaporation".

2.10 Conclusion

This first chapter has provided an overview of the currently available literature related to the evaporation, Marangoni effect, and well behaviour of droplets. It has also detailed some of the theoretical and numerical methods that have been employed to attempt to solve problems of droplet and thin film evolution.

Most significantly, we note that there is a large body of work on the CRE in sessile droplets; Deegan's important study and publication paved the way for researchers to investigate the world of droplets and the multitude of patterns they create when drying. The factors and conditions affecting the deposit distribution from pure sessile droplets have been studied to within an inch of their lives over the last 25 years to the point that we are confident that we understand why the CRE and other deposit effects occur in so many scenarios. The mechanisms of radial flow, evaporation rush-hour, and contact-line (self) pinning are well understood.

It is a different story, however, when reading contributions towards more specific situations of droplet drying; the dynamics of multi-component droplets and DiWs are much less thoroughly researched and, although the basic principles of pure sessile drying apply in general to these more complicated arrangements, it is clear that we do not fully understand all their details, especially not in the intersection of the two. For example, it is easy to find contradictory claims about the efficacy of Marangoni flows in suppressing the CRE. Some, such as Kim *et al.*, even report that they were unable to achieve it at all using the Marangoni effect alone and required additional additives to enhance its strength. As for droplets printed in wells, we have begun to understand how well geometry influences the evaporation, but still lack a theoretical link between the interface shape in the well and its deposit. This says nothing of the cross-effects of droplets both situated in a well and being composed of two components.

Another important, but largely neglected, problem in mixed composition droplets is the evaporative flux. While we seem to have a solid grasp on a theoretical functional form for the flux through the surface of a pure droplet, a binary droplet's evaporative flux depends on the composition of the droplet, which itself evolves in time and space – this factor makes the binary problem more challenging, indeed difficult enough that there are not many attempts to treat binary flux fully in the literature.

In this work, we shall begin to contribute to a theoretical link between pure and binary droplets drying in wells and the impact of these factors on the shape of the droplet and its deposit. We shall use some of the numerical methods we have outlined above, namely MoL and FEM, and the well-understood features present in sessile droplets, such as the recirculating flow profiles and evaporative flux, to build a picture of the mechanisms involved in a binary droplet evaporating from a well and how they influence its overall shape.

Chapter 3

Pure Droplet

We begin the construction of our model by considering the simplest possible non-trivial situation. In our case, that is a pure droplet evaporating in a 2D square or 3D cylindrical well; in this chapter we will set up the problem and derive the governing equations for a 3D axisymmetric droplet, will state the corresponding equation in the 2D case, and analyse and compare simulated results from both of them.

This model will allow us to investigate some fundamental features of an evaporating DiW: its shape near the end of the drying, which plays a large role in influencing the deposit distribution of droplets containing particles; the behaviour of the touchdown point as we change the well geometry and physical properties; and the velocity field during the drying process. For the first time we will be able to reproduce and investigate W- and U-shaped droplets in a numerical simulation, these shapes having been previously observed experimentally.

We will finish by assessing the cylindrical model's accuracy to experimental data and show that the model is good at predicting overall shape behaviour; indeed even quantitative agreement can be found using a best fit over the $\mathcal{C}$ parameter. This does, however, mean there is some discrepancy between experimental and theoretical expectations of $\mathcal{C}$.

3.1 Problem Description

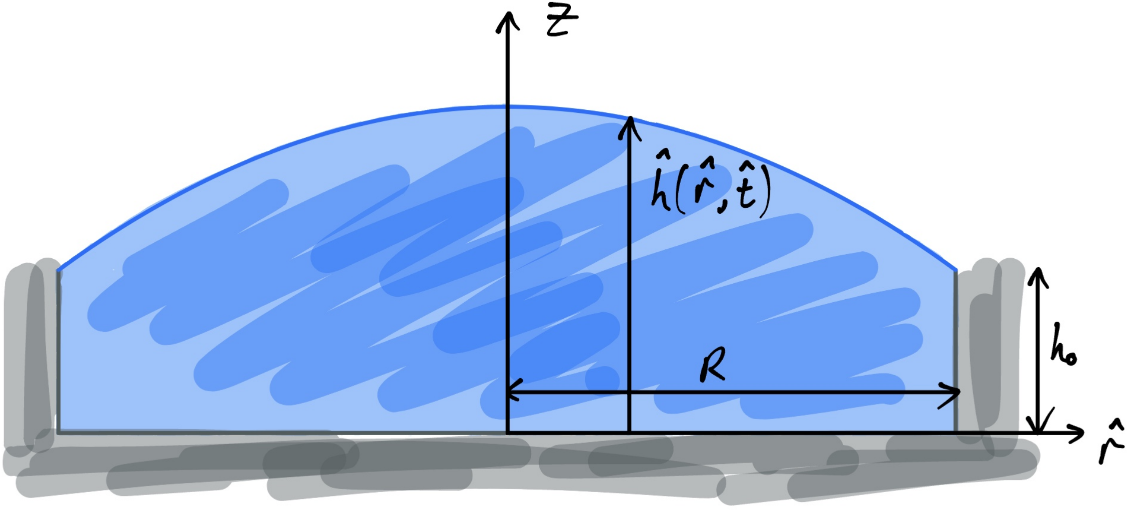

Figure 3.1: A droplet in a cylindrical well.

Consider a droplet in coordinate system $(\hat{r}, \hat{z})$[1] evaporating from a cylindrical well with vertical walls of height h_0 and radius R (see figure 3.1). The droplet's free surface is located at $\hat{z} = \hat{h}(\hat{r}, \hat{t})$ and is pinned to the edge of the well at the point (R, h_0).

The droplet is composed of a single, incompressible liquid of surface tension σ, viscosity μ, and density ρ; we assume it is Newtonian, the Reynolds number is small, and gravity can be neglected in favour of viscous, capillary, and evaporative forces. We also assume that heat transfer can be neglected and the temperature is constant everywhere and always. (See chapter 2, sections 2.4 and 2.8 for discussions on the importance of droplet size and thermal effects respectively.)

3.2 Fluid Dynamics

In this section we will derive the equation of motion for the evaporating droplet-air interface, starting with the fundamental equations for fluid dynamics and applying the appropriate assumptions and boundary conditions for a thin DiW.

We assume that the liquid obeys both mass continuity and the Navier-Stokes equations for an incompressible fluid, namely

$$\hat{\nabla} \cdot \hat{\boldsymbol{u}} = 0, \tag{3.1}$$

and

$$\rho \frac{D\hat{\boldsymbol{u}}}{D\hat{t}} = -\hat{\nabla}\hat{p} + \mu\hat{\nabla}^2\hat{\boldsymbol{u}}, \tag{3.2}$$

---

[1] Circumflex denotes a dimensional variable.

respectively, where $\hat{\boldsymbol{u}} = (\hat{u}, \hat{w})$ is the liquid velocity (radial, vertical) and $\hat{p}$ is the pressure in the liquid[2]. We take the limit of low Reynolds number, under which the Navier-Stokes equations reduce to the Stokes equations,

$$\hat{\nabla}\hat{p} = \mu\hat{\nabla}^2\hat{\boldsymbol{u}}. \tag{3.3}$$

The free surface is subject to stress balance conditions in the normal and tangential directions;

$$\hat{\boldsymbol{n}} \cdot \hat{\boldsymbol{T}} \cdot \hat{\boldsymbol{n}} = \sigma\kappa \ \text{ at } \ \hat{z} = \hat{h} \tag{3.4}$$

where $\hat{\boldsymbol{n}}$ is the unit normal to the interface, $\hat{\boldsymbol{T}}$ is the stress tensor, and $\kappa(r)$ is the mean surface curvature,

$$\kappa = \hat{\nabla} \cdot \frac{\hat{\nabla}\hat{h}}{\sqrt{1 + |\hat{\nabla}\hat{h}|^2}}, \tag{3.5}$$

and

$$\hat{\boldsymbol{t}} \cdot \hat{\boldsymbol{T}} \cdot \hat{\boldsymbol{n}} = \hat{\boldsymbol{t}} \cdot \hat{\nabla}\sigma \ \text{ at } \ \hat{z} = \hat{h} \tag{3.6}$$

where $\boldsymbol{t}$ is the unit tangent to the interface. In this chapter we ignore the possibility of surface tension gradients because we assume the droplet to comprise a single liquid in a constant and stable temperature field.

Material transfer occurs across the interface, described by the kinematic condition,

$$(\hat{\boldsymbol{u}} \cdot \hat{\boldsymbol{n}} - \hat{V}_n) = \frac{1}{\rho}\hat{J}(\hat{r}, \hat{t}) \ \text{ at } \ \hat{z} = \hat{h} \tag{3.7}$$

where $\hat{V}_n = \frac{\hat{h}_{\hat{t}}}{\sqrt{1+\hat{h}_{\hat{r}}^2}}$ is the normal velocity of the interface and $\hat{J}(\hat{r}, \hat{t})$ is the evaporative flux across the free surface. The kinematic condition relates the normal component of the droplet interface's velocity and the normal component of the fluid's velocity to the rate of mass transfer due to evaporation.

There are other boundary conditions: we impose no-slip and impermeability conditions at the base of the well and at the wall and we assume that the droplet is symmetrical about the line $\hat{r} = 0$,

$$\hat{u} = 0 \ \text{ at } \ \hat{z} = 0\,, \tag{3.8}$$

$$\hat{w} = 0 \ \text{ at } \ \hat{z} = 0\,, \tag{3.9}$$

$$\hat{q} = 0 \ \text{ at } \ \hat{r} = 0, R\,, \tag{3.10}$$

where $\hat{q} = \frac{1}{\hat{h}}\int_0^{\hat{h}} \hat{u} \; d\hat{z}$ is the liquid flux. The reader may notice that we have not included no-slip and impermeability at $\hat{r} = R$; these conditions are not useful for us once we have non-dimensionalised and applied the lubrication approximation (section 3.3). In fact, we will see a small outworking of this decision when considering the liquid velocity vector plots in section 3.8.5.

---

[2] $\frac{D}{D\hat{t}}$ is the material derivative

Finally, we assume that the initial profile is prescribed, so that

$$\hat{h} = \hat{h}^*(\hat{r}). \tag{3.11}$$

3.3 Non-Dimensionalisation

We non-dimensionalise the model through the following scaling relations, where dimensionless variables are denoted by the absence of circumflex:

$$\begin{aligned} \hat{r} &= Rr\,, & \hat{z} &= h_0 z\,, & \hat{h} &= h_0 h\,, \\ \hat{t} &= Tt\,, & (\hat{u}, \hat{w}) &= U(u, \frac{h_0}{R}w)\,, & \hat{p} &= \frac{\mu U R}{h_0^2}p\,, \\ \hat{J} &= \rho U \varepsilon J\,, & \hat{q} &= h_0 U q\,, \end{aligned}$$

where $T = \frac{R}{U}$ and U is an intrinsic velocity scale pertaining to the evaporative flux. We will see in section 3.4 that U can be expressed as

$$U = \frac{2DM_m^c(c_0 - c_\infty)}{\pi R \rho}\,, \tag{3.12}$$

where D is the diffusion coefficient of the liquid in air, c_0 is the concentration of liquid vapour in the air immediately above the interface, c_∞ is the concentration infinitely far from the droplet, and M_m^c is the molar mass of the liquid.
Under these scalings the model can be expressed in terms of two dimensionless quantities: the aspect ratio,

$$\varepsilon = \frac{h_0}{R}, \tag{3.13}$$

and the reduced inverse capillary number, given by

$$\mathcal{C} = \frac{\sigma \varepsilon^3}{\mu U}. \tag{3.14}$$

We expand the variables u, w, and p as perturbation series in ε (as in [33]),

$$u = u_0 + u_1\varepsilon + u_2\varepsilon^2 + ..., \tag{3.15}$$

$$w = w_0 + w_1\varepsilon + w_2\varepsilon^2 + ..., \tag{3.16}$$

$$p = p_0 + p_1\varepsilon + p_2\varepsilon^2 + ..., \tag{3.17}$$

and apply the lubrication approximation $\varepsilon \to 0$, while maintaining $\mathcal{C} = \mathcal{O}(1)$ (the former is justified by requirement to imitate experimental procedure; for example in work by D'Ambrosio et. al. the average aspect ratio was about 0.04 [3]. The latter is vital for preserving surface tension terms in the resulting equations [33]). This means neglecting terms of $\mathcal{O}(\varepsilon)$ and smaller, which leaves the model

$$\frac{1}{r}\frac{\partial}{\partial r}[ru_0] + \frac{\partial w_0}{\partial z} = 0, \tag{3.18}$$

$$\frac{\partial^2 u_0}{\partial z^2} = \frac{\partial p_0}{\partial r}, \tag{3.19}$$

$$\frac{\partial p_0}{\partial z} = 0, \tag{3.20}$$

with boundary conditions

$$p_0 = -\frac{\mathcal{C}}{r}\frac{\partial}{\partial r}\left[r\frac{\partial h}{\partial r}\right] \;\text{ at }\; z = h\,, \tag{3.21}$$

$$\frac{\partial u_0}{\partial z} = 0 \;\text{ at }\; z = h\,, \tag{3.22}$$

$$w_0 = \frac{\partial h}{\partial t} + u_0\frac{\partial h}{\partial r} + J(r) \;\text{ at }\; z = h\,, \tag{3.23}$$

$$u_0 = w_0 = 0 \;\text{ at }\; z = 0\,, \tag{3.24}$$

$$q = 0 \;\text{ at }\; r = 0\,,1\,, \tag{3.25}$$

$$h = 1 \;\text{ at }\; r = 1\,, \tag{3.26}$$

$$h = h^*(r) \;\text{ at }\; t = 0\,. \tag{3.27}$$

We now drop the subscripts for brevity. As we mentioned in chapter 2 section 2.2 applying the lubrication approximation in this way restricts our analysis to only those droplets that are very shallow and have small contact angles. Therefore we are very likely to be dealing with long, thin pools of liquid in a well made of particular material for which the liquid wets the solid perfectly.

3.4 Evaporative Flux

It is not immediately clear what form the evaporative flux should take; a number of different evaporation models have been proposed for diffusion-limited evaporation of sessile droplets in the literature [13, 14, 84].
The choice of form of evaporative flux in this work will depend on the geometry of the system being modelled. It is important to note that a droplet in a well does not necessarily have evaporative flux identical to that of a sessile droplet; an ideal form would be to find the vapour concentration field ($\hat{c}$) due to the droplet and use Fick's law to find the evaporation rate,

$$\hat{J}(\hat{r},\hat{t}) = -DM_m^c\hat{\nabla}\hat{c}(\hat{r},\hat{t})\cdot\boldsymbol{\hat{n}}, \tag{3.28}$$

where D is the vapour diffusion coefficient. We will discuss this approach in greater detail in chapter 5; initially it is pragmatic simply to choose an appropriate functional form for the evaporative flux. As detailed in section 2.6, it is common practice to assume that the vapour concentration in the gas above a pure droplet may be described by Laplace's equation,

$$\hat{\nabla}^2 \hat{c} = 0, \tag{3.29}$$

with mixed boundary conditions

$$\hat{c} \to 0 \;\text{ as }\; \hat{r}^2 + \hat{z}^2 \to \infty \tag{3.30}$$

$$\hat{c} = c_0 \;\text{ on }\; \hat{z} = 0 \;\text{ for }\; 0 < \hat{r} < R \tag{3.31}$$

$$\frac{\partial \hat{c}}{\partial \hat{z}} = 0 \;\text{ on }\; \hat{z} = 0 \;\text{ for }\; \hat{r} > R. \tag{3.32}$$

The evaporative flux for a thin (lubrication approximated) sessile droplet with small contact angle is found to be (see [13] for full derivation)

$$\hat{J}(\hat{r}) = \frac{2}{\pi} \frac{D M_m^c (c_0 - c_\infty)}{\sqrt{R^2 - \hat{r}^2}}, \tag{3.33}$$

and it is this form that we shall use, at least initially and in the cylindrical geometry. While such a method is useful for determining the evaporative flux of a stationary system with a thin, flat droplet, it is less useful when considering a more dynamic system, such as a droplet with binary composition that evolves over the lifetime of the droplet. It also neglects to account for the droplet-vapour coupling in more exotic scenarios, for example, in which negative concentration gradients in the gas emerge along certain regions of the interface. In these cases it is desirable to have a full vapour phase simulation and to use equation 3.28 to calculate the evaporation profile.

After nondimensionalisation, the evaporative flux in the dimensionless model becomes

$$J(r) = \frac{1}{\sqrt{1 - r^2}}\,. \tag{3.34}$$

3.5 Deriving a Lubrication Equation

We can derive an expression for the velocity in the liquid phase by integrating equation 3.19 twice, using equations 3.21 and 3.24a as boundary conditions:

$$u(r,z) = -\mathcal{C} \frac{\partial}{\partial r}\left[\frac{1}{r}\frac{\partial}{\partial r}\left[r\frac{\partial h}{\partial r}\right]\right]\left(\frac{1}{2}z^2 - zh\right). \tag{3.35}$$

We then integrate equation 3.18 over the height of the droplet and use the impermeability of the substrate to find the vertical velocity at the interface

$$w(h) = -\int_0^h \frac{1}{r}\frac{\partial}{\partial r}[ru]\, dz, \tag{3.36}$$

and insert this into the mass transfer condition, equation 3.23,

$$\frac{\partial h}{\partial t} + u(z=h)\frac{\partial h}{\partial r} + J + \int_0^h \frac{1}{r}\frac{\partial}{\partial r}[ru]\, dz = 0. \tag{3.37}$$

Using the Leibniz integral rule and the no-slip boundary condition, the final term in equation 3.37 can be expressed

$$\int_0^h \frac{1}{r}\frac{\partial}{\partial r}[ru]\;dz = \frac{1}{r}\frac{\partial}{\partial r}\int_0^{h(r,t)} u\;dz - u(z=h)\frac{\partial h}{\partial r}\,, \tag{3.38}$$

which simplifies equation 3.37 to

$$\frac{\partial h}{\partial t} + \frac{1}{r}\frac{\partial}{\partial r}\int_0^{h(r,t)} ru\;dz + J = 0\,. \tag{3.39}$$

Equations 3.35 and 3.39 combine to give a lubrication equation for height evolution,

$$\frac{\partial h}{\partial t} = -\frac{\mathcal{C}}{3r}\frac{\partial}{\partial r}\left[rh^3\frac{\partial}{\partial r}\left[\frac{1}{r}\frac{\partial}{\partial r}\left[r\frac{\partial h}{\partial r}\right]\right]\right] - \frac{1}{\sqrt{1-r^2}}\,. \tag{3.40}$$

The droplet's cylindrical symmetry means that

$$\frac{\partial h}{\partial r} = \frac{\partial^3 h}{\partial r^3} = 0 \;\text{ at }\; r = 0 \tag{3.41}$$

and it is pinned at $(1,1)$, so

$$h = 1 \;\text{ at }\; r = 1\,. \tag{3.42}$$

The no-flux wall condition means that the height averaged velocity at the wall vanishes,

$$\frac{\partial}{\partial r}\left[\frac{1}{r}\frac{\partial}{\partial r}\left[r\frac{\partial h}{\partial r}\right]\right] = 0 \;\text{ at }\; r = 1\,, \tag{3.43}$$

and we choose a simple initial condition that adheres to the boundary conditions,

$$h^*(r) = a + (1-a)r^2\,, \tag{3.44}$$

which is the equilibrium shape for an interface with small aspect ratio in the absence of gravity. Unless otherwise stated, we will take $a = 1.5$.

3.6 Two-Dimensional Version

The preceding derivation was performed for a three-dimensional axisymmetric droplet in a cylindrical well; it is worth also stating the results for a strictly two-dimensional droplet in a square well (width $2L$) also, as we will discuss both models in later chapters. However, the reader should assume we are referring to the three-dimensional axisymmetric model unless otherwise stated.

The main difference for the 2D model is that the pressure has a slightly different form,

$$p = \mathcal{C}\frac{\partial^2 h}{\partial x^2}\,, \tag{3.45}$$

then following the analogous logic for a two-dimensional droplet in a square well (in cartesian coordinates (x,z)) leads to a similar system:

$$\frac{\partial h}{\partial t} = -\frac{\mathcal{C}}{3}\frac{\partial}{\partial x}\left[h^3 \frac{\partial^3 h}{\partial x^3}\right] - J(x)\,, \tag{3.46}$$

$$\frac{\partial h}{\partial x} = \frac{\partial^3 h}{\partial x^3} = 0 \ \text{ at } \ x = 0\,, \tag{3.47}$$

$$h = 1 \ \text{ at } \ x = 1\,, \tag{3.48}$$

$$\bar{u} = \frac{\mathcal{C}}{3} h^2 \frac{\partial^3 h}{\partial x^3} = 0 \ \text{ at } \ x = 1\,, \tag{3.49}$$

$$h^*(x) = a + (1-a)x^2\,. \tag{3.50}$$

For the evaporation we use the same functional form as equation 3.34,

$$J(x) = \frac{1}{\sqrt{1-x^2}}\,. \tag{3.51}$$

We note that this is not the correct functional form for a 2D droplet with diffusion-limited evaporation in a 2D half-space. Schofield *et al.* [118] discovered that the closed-form solution to that problem is non-trivial, requiring the far-field ambient condition be imposed on the edge of a large ellipse of semi-minor axis Ψ:

$$\hat{J} = \frac{1}{\arcsin(\Psi/L)}\frac{1}{\sqrt{L^2 - \hat{x}^2}}\,. \tag{3.52}$$

There is no closed form of the 2D steady state vapour solution with an infinite boundary. Because we are concerned more with comparisons to the cylindrical case in this work, we will retain the simpler version, equation 3.51.

3.7 Numerical Methods

We solved the PDE using the method of lines with Mathematica's NDSolve function. We discretised the spatial component of each equation and applied the relevant boundary conditions at each end of the simulation domain to obtain height evolution ODEs for each point along the droplet.

3.7.1 Cylindrical Well

The domain in the cylindrical well is defined between $r = 0$ and $r = 1$, split into N regions of width Δr. We discretise the spatial component of equation 3.40 in two parts, first approximating the first level of the derivative halfway between grid points (at $i + \frac{1}{2}$) with a finite difference expression, then writing the full equation as a second order finite difference scheme for first derivatives. It is important to be especially careful with the point at $i = 0$, given that equation 3.40 has an apparent singularity at the origin – of course, this is purely an artefact of the cylindrical coordinates, and so the singularity does not actually exist. We differentiate out the brackets

$$g(r) = rh^3 \frac{\partial}{\partial r}\left[\frac{1}{r}\frac{\partial}{\partial r}\left[r\frac{\partial h}{\partial r}\right]\right] = rh^3\Big(\frac{\partial^3 h}{\partial r^3} + \frac{1}{r}\frac{\partial^2 h}{\partial r^2} - \frac{1}{r^2}\frac{\partial h}{\partial r}\Big) \tag{3.53}$$

and only then discretise,

$$g_{i+\frac{1}{2}} = \frac{(i+\frac{1}{2})(h_{i+1}+h_i)^3}{8\Delta r^2}\Big((h_{i+2}-3h_{i+1}+3h_i-h_{i-1}) \\ +\frac{1}{2i}(h_{i+2}-h_{i+1}-h_i+h_{i-1})-\frac{1}{i^2}(h_{i+1}-h_i)\Big). \quad (3.54)$$

The full ODE for height evolution in cylindrical geometry is, then,

$$\frac{\partial h_i}{\partial t} = -\frac{\mathcal{C}}{3i\Delta r^2}(g_{r,i+\frac{1}{2}}-g_{r,i-\frac{1}{2}})-\frac{1}{\sqrt{1-(i\Delta r)^2}}. \quad (3.55)$$

We need to deal with the special cases at grid points $i=0$, $i=1$, and $i=N-1$ (the droplet pin again prevents evolution at point $i=N$). Particular care at $i=0$ is needed to avoid the singularity; we start by fully expanding the triple derivative expression,

$$\frac{1}{r}\frac{\partial}{\partial r}\Big[rh^3\frac{\partial}{\partial r}\Big[\frac{1}{r}\frac{\partial}{\partial r}\Big[r\frac{\partial h}{\partial r}\Big]\Big]\Big] = \\ \frac{h^3}{r}\frac{\partial^3 h}{\partial r^3}+3h^2\frac{\partial h}{\partial r}\frac{\partial^3 h}{\partial r^3} \\ +h^3\frac{\partial^4 h}{\partial r^4}+\frac{3h^2}{r}\frac{\partial h}{\partial r}\frac{\partial^2 h}{\partial r^2} \\ +\frac{h^3}{r}\frac{\partial^3 h}{\partial r^3}-\frac{3h^2}{r^2}\Big(\frac{\partial h}{\partial r}\Big)^2+\frac{h^3}{r^3}\frac{\partial h}{\partial r}-\frac{h^3}{r^2}\frac{\partial^2 h}{\partial r^2}. \quad (3.56)$$

For $h(r,t)$ to be bounded at $r=0$, all terms multiplying a $\frac{1}{r}$ must vanish; that is

$$\frac{\partial h}{\partial r}=\frac{\partial^2 h}{\partial r^2}=\frac{\partial^3 h}{\partial r^3}=0 \text{ at } r=0. \quad (3.57)$$

We can now use l'Hôpital's rule on each term repeatedly until the $\frac{1}{r}$ terms are eliminated; however, given equation 3.57, the only terms that will survive necessarily have the form

$$\frac{1}{r^\lambda}\frac{\partial^{4-\nu}h}{\partial r^{4-\nu}}, \text{ with } \lambda \geq \nu, \quad (3.58)$$

meaning terms 2, 4, and 6 on the right hand side of equation 3.56 drop out immediately. After applying l'Hôpital's rule, the triple derivative finally becomes

$$\frac{1}{r}\frac{\partial}{\partial r}\Big[rh^3\frac{\partial}{\partial r}\Big[\frac{1}{r}\frac{\partial}{\partial r}\Big[r\frac{\partial h}{\partial r}\Big]\Big]\Big]\Big|_{r=0} = \frac{8}{3}h^3\frac{\partial^4 h}{\partial r^4}. \quad (3.59)$$

The partial difference approximation of a fourth-order derivative at $i=0$ refers to ghost points at $i=-1$ and $i=-2$; these are given by symmetry arguments across the centre so the discretisation at $i=0$ is

$$\frac{\partial h_0}{\partial t} = -\frac{16}{9\Delta r^2}\mathcal{C}h_0^3(h_2-4h_1+3h_0)-1. \quad (3.60)$$

At $i=1$ the first order symmetry removes dependence on a ghost point,

$$\frac{\partial h_1}{\partial t} = -\frac{\mathcal{C}}{24\Delta r^4}\Big(\frac{1}{2}(h_2+h_1)^3\Big(4h_3 - \frac{34}{3}h_2 + \frac{28}{3}h_1 - 2h_0\Big) - (h_1+h_0)^3\Big(h_2 - 4h_1 + \frac{3}{2}h_0\Big)\Big) - \frac{1}{\sqrt{1-(\Delta r)^2}}. \quad (3.61)$$

For the equation at $i = N-1$, we will need an expression for the ghost point h_{N+1}, which can be derived from the vanishing fluid flux at $r = 1$; writing equation 3.43 as a finite difference expression evaluated at $i = N$ gives

$$h_{N+2} + h_{N+1}(-2 + 2\Delta r - \Delta r^2) + 4\Delta r + h_{N-1}(2 + 2\Delta r + \Delta r^2) - h_{N-2} = 0, \quad (3.62)$$

and we use the lubrication equation, equation 3.40, at $r = 1$ to eliminate h_{N+2} (remembering that at the pin we have $h = 1$, $\bar{u} = 0$, and $h_t = 0$). Finally, after neglecting terms in Δr^2 and smaller,

$$h_{N+1} = (-3\Big(1 + \frac{2}{3}\Delta r\Big) + h_{N-1}(3 + \Delta r) - h_{N-2})(1 + \Delta r)^{-1}. \quad (3.63)$$

We now have a height ODE in time for each point along the droplet and can proceed with NDSolve to simulate its evolution. The two-dimensional system, equations 3.46 - 3.50, can be discretised analogously.

3.8 Results

We are left with N ODEs for height evolution in time, one for each gridpoint along the droplet. We plot the solution of the equation as a cross section of the droplet, with evolution over time represented by a series of lines. The simulation stops when the droplet touches down, that is, when the fastest decreasing of the height values reaches a predetermined minimum value. The reason we decided to arrest the simulation at touchdown is that the physics of the droplet changes as soon as touchdown is reached; the touchdown point becomes a receding contact line [3] and a liquid ring shoulder emerges (if the DiW forms a W-shape, a sessile droplet in the centre of the well also appears; see section 3.8.3 for more details). While we could change the boundary conditions at that point and continue to simulate the evolution of an annulus (+ inner sessile droplet), we deemed it more important to thoroughly understand the physics that drives the initial drying until touchdown. The annulus has already been studied analytically in the limit of large $\mathcal{C}$ [3].

3.8.1 Simulation Convergence

Before diving into analysis of the results it is important to confirm that the simulation converges as the number of grid points becomes large. In order to verify numerical convergence we simulated the droplet evolution for increasing spatial resolution ($\log_2(N) = (3, 4, 5, 6, 7, 8, 9)$) and determined the residual from the previous iteration for each point at 10 equally spaced time intervals. We then took the mean of all these points in order to acquire a measure for the average difference per point as N increases.

We have also addressed the problem of mass conservation, quantifying the natural mass loss of the simulation and comparing it to the spatial discretisation and resolution.

The convergence data in the following paragraphs are from the axisymmetric droplet in a cylindrical well simulation, but they apply equivalently to the square well case. Figure 3.2 shows that the simulation converges for $\mathcal{C} = 0.2$ – the black dots represent the residual error associated with multiplying the number of points by 2; that is, for each n, we have taken the mean height difference per point between a simulation with 2^n grid points and one with 2^{n-1} grid points.

The orange line is an exponential that fits the data,

$$\text{Error}(n) = E_0 e^{-\alpha_{\text{er}} n}, \tag{3.64}$$

where α_{er} is positive.

The total error from the 'true' solution, then, can be thought of as the integral

$$\text{Error}_{\text{tot}}(n) = \int_n^\infty \text{Error}(n')dn', \tag{3.65}$$

given that we might expect to find the 'true' solution at $n = \infty$. Written in terms of the number of points, this has the form

$$\text{Error}_{\text{tot}}(N) = \frac{1}{\alpha_{\text{er}}} N^{-\frac{\alpha_{\text{er}}}{\ln 2}}, \tag{3.66}$$

hence the simulation converges sensibly for large N.

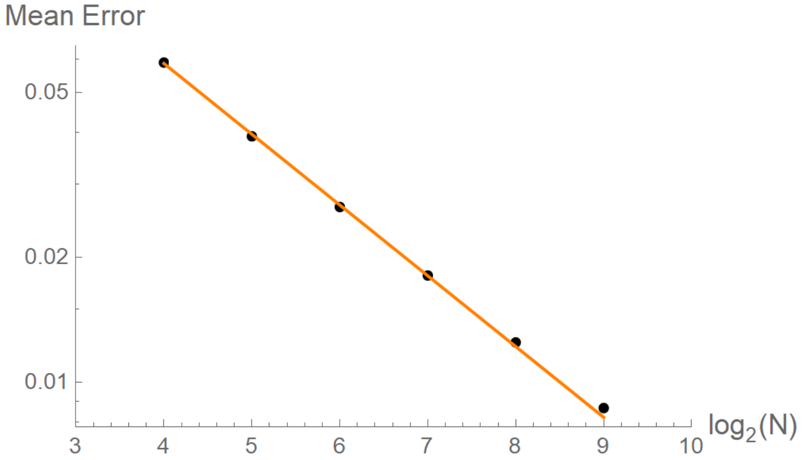

Figure 3.2: A log plot of the mean residual per point, black dots, as a function of number of grid points, N, for $\mathcal{C} = 0.2$. An exponential function (orange line) fits the points.

We present in figure 3.3 the same data for values of $\mathcal{C}$ of different orders of magnitude, showing that this kind of simulation convergence is independent of the $\mathcal{C}$ parameter.

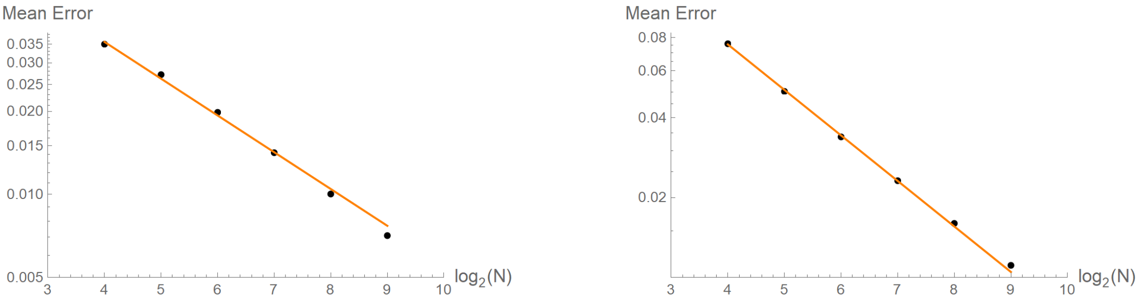

(a) $\mathcal{C} = 0.02$ (b) $\mathcal{C} = 2$

Figure 3.3: The mean residual per point as a function of the number of grid points.

The other factor to consider is the mass conservation of the simulation; we should expect that mass is conserved to within a certain precision that depends on the resolution of discretisation. Mass inside the droplet at time t is given by

$$M_r(t) = 2\pi \int_0^1 rh(r,t)dr. \tag{3.67}$$

Figure 3.4 is a diagram of the droplet mass (per equation 3.67), evaporated mass,

$$M_{\text{evap}}(t) = 2\pi t, \tag{3.68}$$

and total mass,

$$M_{\text{tot}}(t) = M_r(t) + M_{\text{evap}}(t) \tag{3.69}$$

The figure shows that, in the eyeball norm and on the scale of the whole droplet, any loss in mass is small; nonetheless, it is useful to quantify the conservation of mass over the lifetime of the droplet.

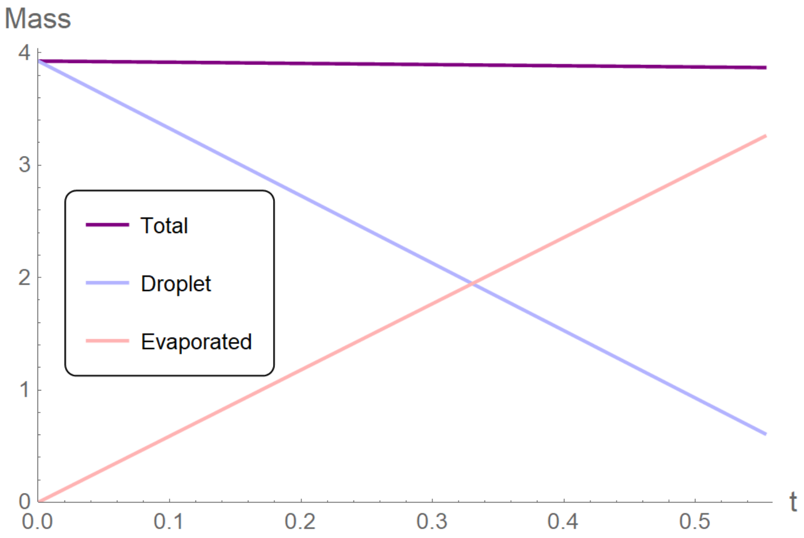

Figure 3.4: Mass conservation over time for a droplet with $N = 2^9$ points and $\mathcal{C} = 0.2$.

Figure 3.5 shows the variation in total mass loss, $\delta M = \frac{M_{\text{tot}}(t_f)}{M_{\text{tot}}(0)}$, as a function of the resolution of the simulation. The fitted (purple) function is of the form

$$\delta M \sim dr^{0.65}. \tag{3.70}$$

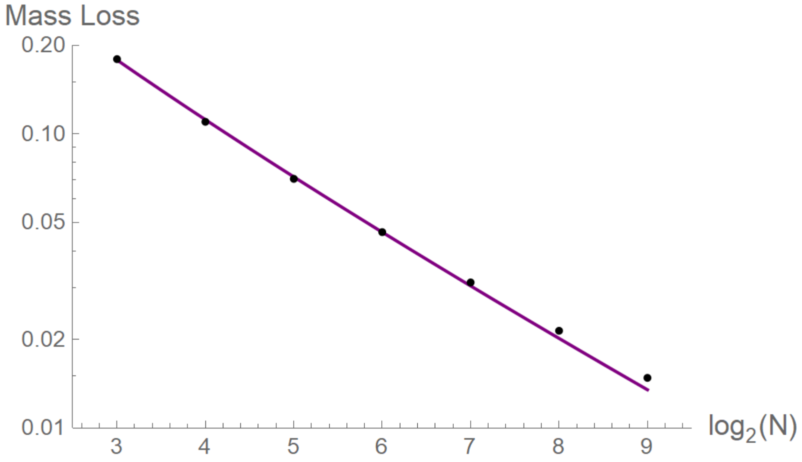

Figure 3.5: Mass loss fraction plotted against the number of points. $\mathcal{C} = 0.2$.

3.8.2 Droplet Profiles

Cross section solutions of the lubrication equation for a droplet evaporating from a 2D square well are presented in figure 3.6 and from a cylindrical well in figure 3.7, both in order of increasing $\mathcal{C}$. Time increases in equal steps as each droplet evaporates down and is also indicated by the colour of the line: orange to yellow to green. Only the positive half is shown in each figure, symmetry about the vertical axis is implied.

These figures demonstrate the extent of control one can exert over a droplet's shape through the $\mathcal{C}$ parameter; each of them (except figure 3.6c, the square well with the largest $\mathcal{C}$) features a half lens type shape towards the end of the evaporation, whose exact size, shape, and formation time are determined by $\mathcal{C}$. Until touchdown, the lens is connected to the wall liquid by a thinner section, which 'pinches' upon touchdown. The simulation ends at this point, because a new set of boundary conditions would be required to describe the two newly formed contact lines. Additionally, one of the main aims of this project is to compare the model to experimental data, which becomes harder to acquire after touchdown – there is uncertainty about the permanence of the pin and the interferometry data analysis is hindered by finely spaced fringes [3].

The differences between cartesian and cylindrical simulations are not immediately obvious. However, there are small differences between touchdown locations and times, and the curves are qualitatively slightly different too. Nevertheless, the qualitative similarity between the two models will be useful for analysis of asymmetry in a later chapter, where full 3D simulations are prohibited by large computational cost.

Regardless of well geometry, increasing $\mathcal{C}$ over several orders of magnitude flattens out the lens observed at small values of $\mathcal{C}$; the larger it is, the less prominent the lens until, at some critical value, it disappears altogether. This phenomenon will be quantitatively explored in section 3.8.3.

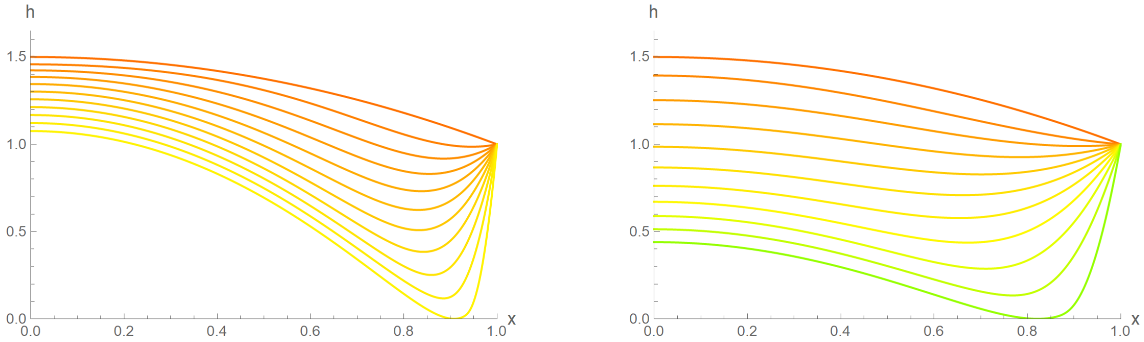

(a) $\mathcal{C} = 0.02$, touchdown occurs at $(x, t) = (0.91, 0.46)$

(b) $\mathcal{C} = 0.2$, touchdown occurs at $(x, t) = (0.83, 0.71)$

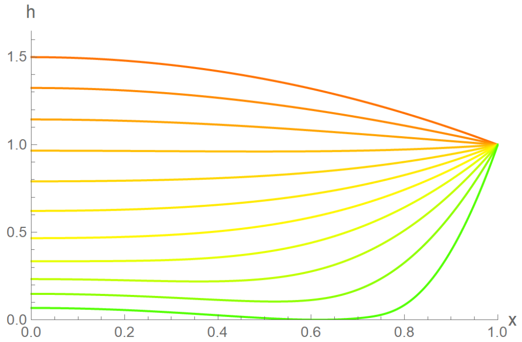

(c) $\mathcal{C} = 2$, touchdown occurs at $(x, t) = (0.62, 0.80)$

Figure 3.6: Cartesian simulation results of droplets evaporating. The colours represent time as it increases – the curves are orange at $t = 0$ and become yellow and finally green at late times.

The touchdown time and location also depend on $\mathcal{C}$; the location of touchdown is another feature we will explore quantitatively in this chapter.
The eagle-eyed reader will notice that, although the solutions are sampled at equal time intervals, the curves in figure 3.7a appear compressed between the first three time points and near $r = 0$. This effect is unexpected. Recognising that it occurs at a low value of $\mathcal{C}$, we can express h as a series expansion in powers of $\mathcal{C}$,

$$h = \tilde{h}_0 + \mathcal{C}h_1 + \mathcal{C}^2 h_2 + \dots, \tag{3.71}$$

and find the lubrication equation at leading order:

$$\frac{\partial \tilde{h}_0}{\partial t} = -\frac{1}{\sqrt{1 - r^2}}\,. \tag{3.72}$$

We would therefore expect the droplet to decrease at a constant rate, $\tilde{h}_0 = h^*(r = 0) - t$, at its centre (with an error on the order of $\mathcal{C}$); figure 3.8 confirms that there is a small kink near the beginning of the evaporation (after the kink, however, the height at the centre does indeed decrease at rate t). This compression of curves is a numerical artefact that appears at the beginning of simulations with very low $\mathcal{C}$; we shall address it more thoroughly in section 3.8.5 of this chapter.

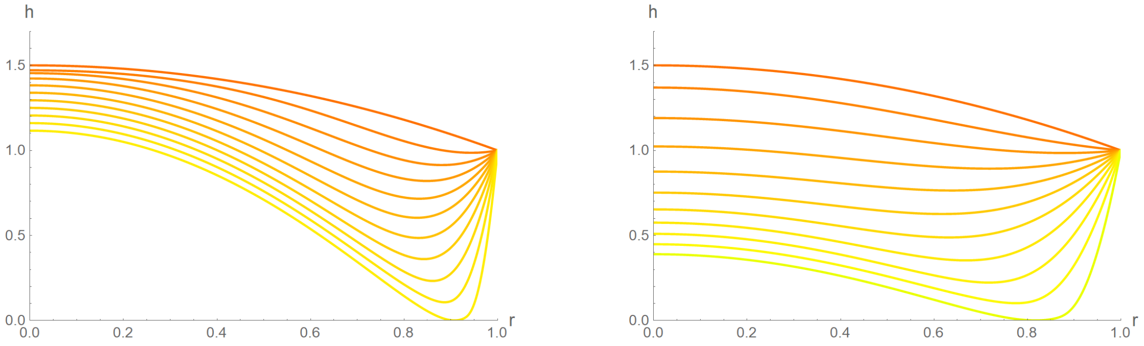

(a) $\mathcal{C} = 0.02$, touchdown occurs at $(r, t) = (0.91, 0.42)$

(b) $\mathcal{C} = 0.2$, touchdown occurs at $(r, t) = (0.82, 0.55)$

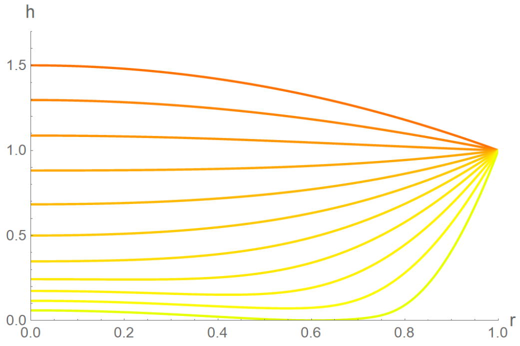

(c) $\mathcal{C} = 2$, touchdown occurs at $(r, t) = (0.61, 0.56)$

Figure 3.7: Cylindrical simulation results of droplets evaporating. The colours represent time as it increases – the curves are orange at $t = 0$ and become yellow and finally green at late times. These are all examples of W-shaped droplets, having dimples at late times that mean the touchdown point is not at $r = 0$.

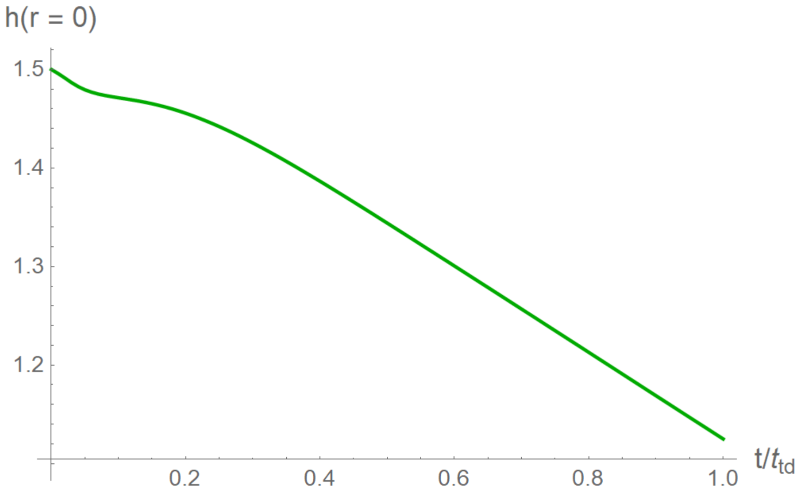

Figure 3.8: The evolution of the height at the centre of the droplet for $\mathcal{C} = 0.02$. Note the presence of a kink at the beginning, which is caused by the numerical artefact we explain in section 3.8.5.

3.8.3 Curvature at Origin

Intuitively, it makes sense that the dimple should shrink as $\mathcal{C}$ increases due to the roles of surface tension, viscosity, evaporative flux, and well geometry (described in equation 3.14).

Surface tension acts to minimise surface area; it resists the pulling-apart of local points on the surface and changes in surface curvature and makes it harder for the droplet to form a dimple shape.

Viscosity acts against surface tension in the sense that it resists fluid motion and slows the flow. Crudely described, capillary forces in the droplet tend to suck fluid towards the more quickly depleting region near the edge [4, 12]; the slower flow associated with higher viscosity impedes this effect and encourages a more prominent lens.

$\mathcal{C}$ is highly sensitive to variations in well geometry, $\mathcal{C} \sim \varepsilon^3$. The wider the droplet compared to its height, the further liquid has to flow under capillary forces to replenish the depletion at the edge and the more prominent the dimple shape.

Finally, greater evaporative flux naturally means shorter evaporation time. Therefore the fluid in the droplet, while having the same horizontal component of velocity, will have less time to correct for the formation of the dimple.

Because of the symmetry condition imposed across the origin, the height $h(0, t)$ will always necessarily be an extremum, meaning we can establish information about the droplet's evolution to a lens shape by examining the curvature at $r = 0$. In the 3D cylindrical case:

$$\kappa(r = 0) = \frac{\partial^2 h}{\partial r^2}\bigg|_{r=0}. \tag{3.73}$$

We show the 3D curvature evolution in figure 3.9, which contains data for values of $\mathcal{C}$ between 0.4 and 16. There are three clear regimes, indicated by the colours blue, red, and black: 1. the curvature does not change sign; 2. the curvature changes sign twice; and 3. the curvature changes sign just once. The dashed lines represent the $\mathcal{C}$ values ($\mathcal{C}_1 = 0.76$ and $\mathcal{C}_2 = 14.3$) on the border between two regimes.

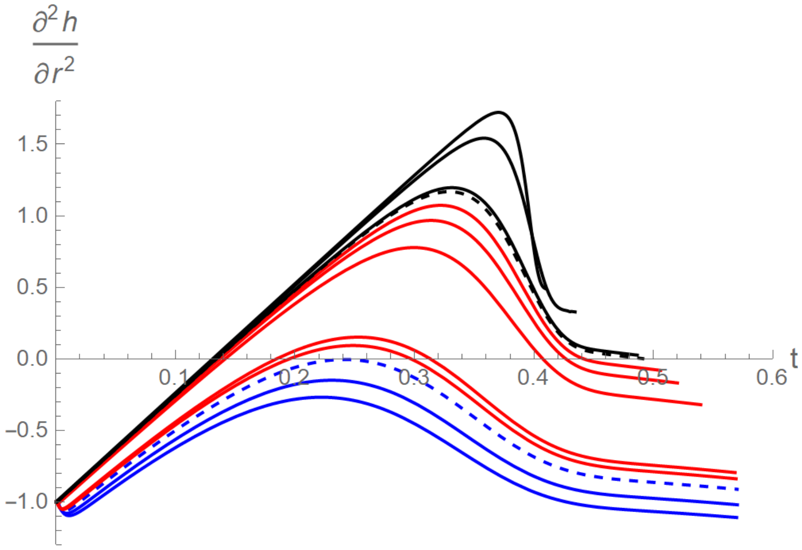

Figure 3.9: The evolution of the curvature of the droplet at $r = 0$. From bottom to top, $\mathcal{C} = 0.5, 0.6, 0.76, 0.9, 1, 4, 7, 10, 14.3, 16, 100, 500$. Colours denote the three lens-formation regimes described below and dashed lines denote the transition between two regimes (at $\mathcal{C} = 0.76$ and $\mathcal{C} = 14.3$ respectively).

The three regimes are given by

1. $\mathcal{C} < \mathcal{C}_1$ and the lens forms straightforwardly (blue);
2. $\mathcal{C}_1 < \mathcal{C} < \mathcal{C}_2$ and the lens does not form initially (rather the droplet tends to be flatter), but subsequently does form (red);
3. $\mathcal{C} > \mathcal{C}_2$ and the lens does not form at all (black).

It is helpful to ascribe shapes to the three regimes: droplets in regimes 1 and 2 all strictly form a W-shape (while those in regime 1 consistently have a W-shape when $h(r = 0) < 1$, those in regime 2 spend some time as a spherical bowl), as can be seen in all three subfigures in figure 3.7; droplets in regime 3 all strictly form a C-shape, visible in figure 3.10b; droplets close to the border between regimes 2 and 3 form what could be described as a U-shape, i.e. a nearly flat-bottomed C-shape, as shown in figure 3.10a.

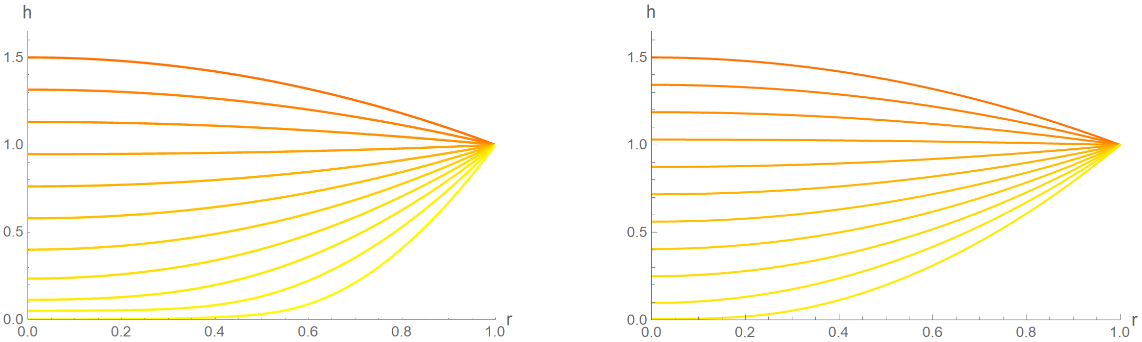

(a) $\mathcal{C} = 16$, touchdown occurs at $(r, t) = (0, 0.49)$. U-shape.

(b) $\mathcal{C} = 500$, touchdown occurs at $(r, t) = (0, 0.41)$. C-shape.

Figure 3.10: The evolution of U-shaped and C-shaped droplets in cylindrical coordinates. Time increases from orange to yellow, with colour consistent across both figures. U-shaped interfaces are characterised by a flatter bottom than C-shaped ones, which are approximately quadratic.

The curvature evolution across the whole droplet is shown in figure 3.11 for two values of $\mathcal{C}$, both in regime 1 (blue). The curvature is negative near the centre and, after a short amount of time, sharply becomes positive towards the edge. The equation for curvature is

$$\kappa = \frac{1}{r}\frac{\partial}{\partial r}\left[r\frac{\partial h}{\partial r}\right]. \tag{3.74}$$

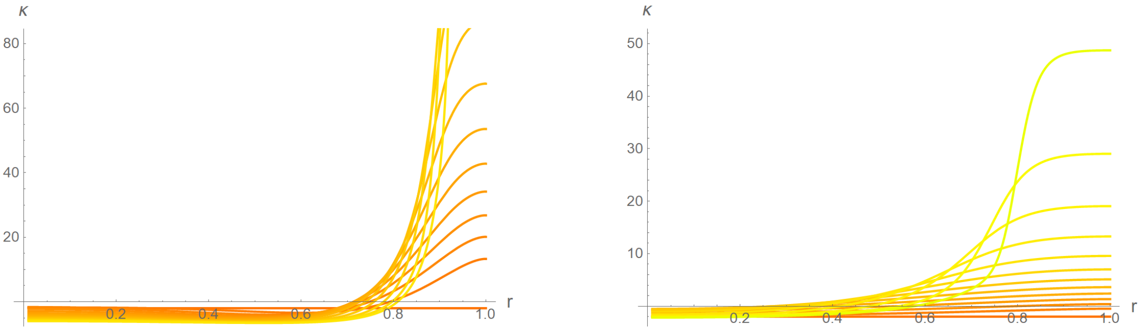

(a) $\mathcal{C} = 0.01$

(b) $\mathcal{C} = 0.5$

Figure 3.11: Curvature evolution across the whole droplet. Time increases from orange to yellow, with colour consistent across both figures.

We stated earlier that surface tension acts to pull local height points together and to maintain a constant curvature; this effect can be seen more clearly in figures 3.11 and 3.12, which contain data for droplets in regime 1. Figure 3.12 shows the evolution of the height difference between the highest point of the lens (that is, we have excluded the shoulder on the outside because the constant pin at $r = 1$ would interfere with the late-time results) and the lowest points of the droplet (excluding the shoulder is not important for the lowest point) for a range of values of $\mathcal{C}$. As $\mathcal{C}$ (and so too σ) increases, the height difference decreases, indicating that surface tension does indeed play a role in controlling the height extrema. However, at low values of $\mathcal{C}$ the final height range does not actually decrease as $\mathcal{C}$ increases – instead, although the range rates decrease, the fact that they have longer before touchdown means their height range has more time to reach the same value. Figure 3.11 demonstrates the same effect. It is clear that the curvature has a smaller range for the larger value of $\mathcal{C}$; the larger surface tension acts to reduce the maximum curvature (always located at the pinned contact line) and flattens the curvature out near the edge.

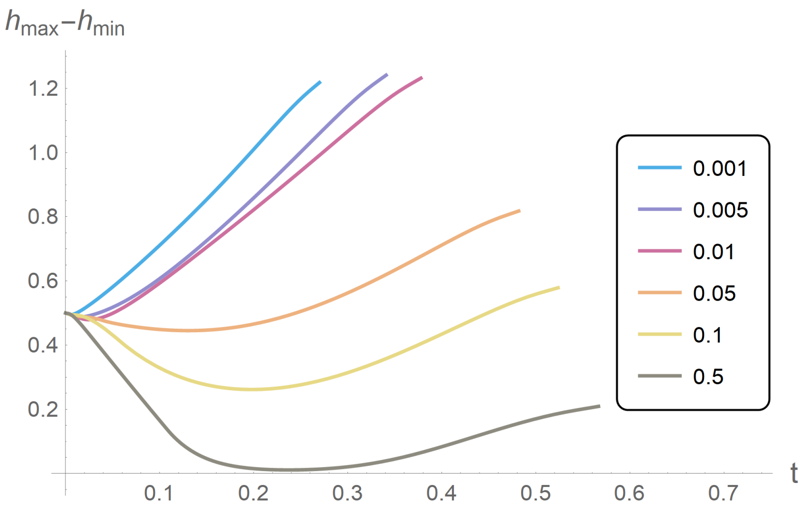

Figure 3.12: Height span of the droplet lens as it evaporates. Those droplets with smaller values of $\mathcal{C}$ consistently exhibit a lens with much larger range in height, because of the lower surface tension and larger viscosity. The colours refer to the corresponding value of $\mathcal{C}$ given in the legend. The case with $\mathcal{C} = 0.5$ has a height range of approximately 0 for some time, which indicates that the interface is briefly completely horizontal.

3.8.4 Touchdown

$\mathcal{C}$ also influences the location and time of touchdown, that is when the droplet surface first comes into contact with the substrate. In our simulations, the droplet never strictly touches down, because we end the simulation before any of the heights reaches zero (the exact condition is to break the simulation when the minimum height reaches 10^{-3}). For the purpose of concision, we shall consistently use the term ‘touchdown’ in this work to refer to a simulated droplet tending towards touchdown. Because we are much more interested in the behaviour of the droplet interface before touchdown, we have not included in this thesis a discussion of the Hamaker constant and the intermolecular forces between the droplet’s surface and the substrate. In order to determine the exact behaviour **at** and immediately **after** touchdown, we would need to consider the stability of the droplet interface as it reaches the substrate.

Figure 3.13a is a log-log graph of the radius of touchdown, r_{td} (here displaced by some constant d_{td}), as a function of $\mathcal{C}$ with a model fit imposed on top.

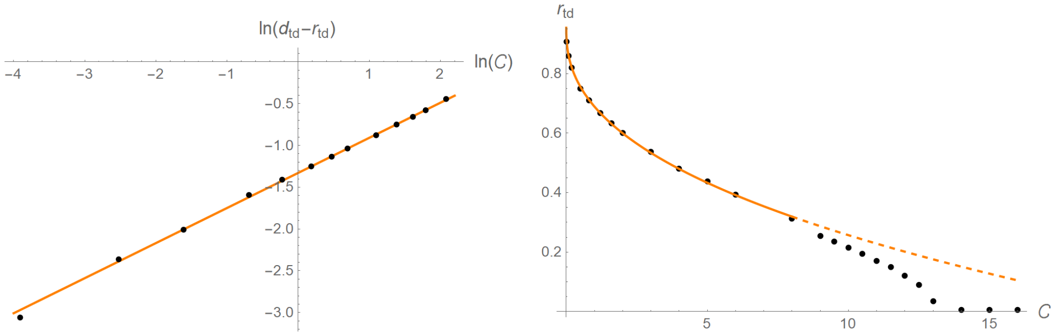

(a) Log plot (b) Linear plot

Figure 3.13: A log plot and a linear plot of touchdown radius against $\mathcal{C}$ (black points) and the power law fit (orange line). The log plot reveals the power law fit for the range of $\mathcal{C}$ values between 0.02 and 8.

The log-log plot reveals a straightforward power law of the form

$$r_{\text{td}} = A_{\text{td}}\mathcal{C}^{k_{\text{td}}} + d_{\text{td}}, \tag{3.75}$$

and in this case $A_{\text{td}} = -0.265 \pm 0.006$, $k_{\text{td}} = 0.419 \pm 0.008$, and $d_{\text{td}} = 0.954 \pm 0.005$. Increasing $\mathcal{C}$ beyond a certain point, however, reveals that the touchdown point does not continue to follow this power law indefinitely, as can be seen in figure 3.13b. Instead, there is a transition between touchdown described by a power law and touchdown occurring exclusively at $r = 0$. The transition is complete at $\mathcal{C} \approx 13.5$, which is consistent with the boundary between origin curvature regimes 2 and 3 in figure 3.9.

We note that figures 3.13a and 3.13b do not give any information about the boundary between regimes 1 and 2.

As we discussed in chapter 2 and section 3.4 of this chapter, it is not entirely clear what mathematical form a droplet's evaporative flux should take for the specific case of a DiW, despite the popularity of the Popov/divergent form that we have been using (which is derived for sessile droplets). One of the benefits of performing simulation analysis of the problem is that we can try out other forms of the evaporative flux, for example a spatially uniform function, $J(r) = 1$.

Performing the same computation for a uniform evaporation on a cylindrical droplet returns figures 3.14a and 3.14b, which also reveal a power law relationship, now with $A_{\text{td}} = -0.940 \pm 0.008$, $k_{\text{td}} = 0.52 \pm 0.02$, and $d_{\text{td}} = 0.88 \pm 0.01$.

Touchdown occurs closer to the origin for the same $\mathcal{C}$ compared to the Popov form, but the qualitative behaviour of the touchdown point is the same: r_{td} follows a power law until a certain value of $\mathcal{C}$, then drops quickly as the W-U-C shape phase change occurs.

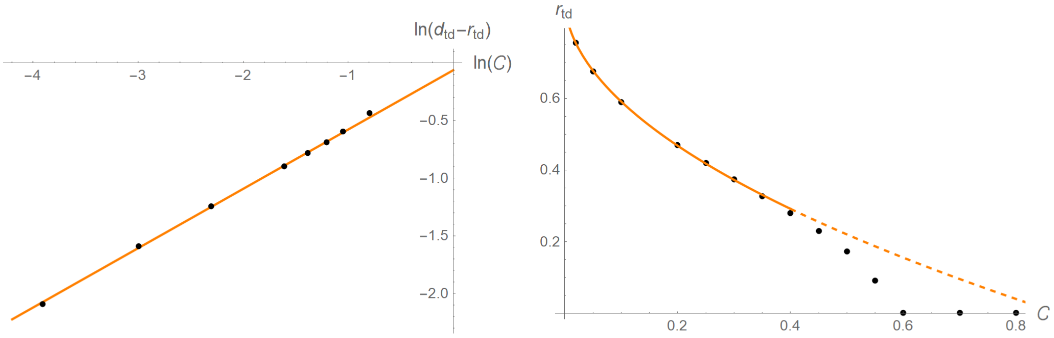

(a) Log plot (b) Linear plot

Figure 3.14: A log plot and a linear plot of touchdown radius against $\mathcal{C}$ (black points) and the power law fit (orange line) for uniform evaporation.

We observe similar behaviour in the 2D square well; here the power law parameters are $A_{\text{td}} = -0.248 \pm 0.006$, $k_{\text{td}} = 0.43 \pm 0.01$, and $d_{\text{td}} = 0.952 \pm 0.005$ and the touchdown plot is figure 3.15.

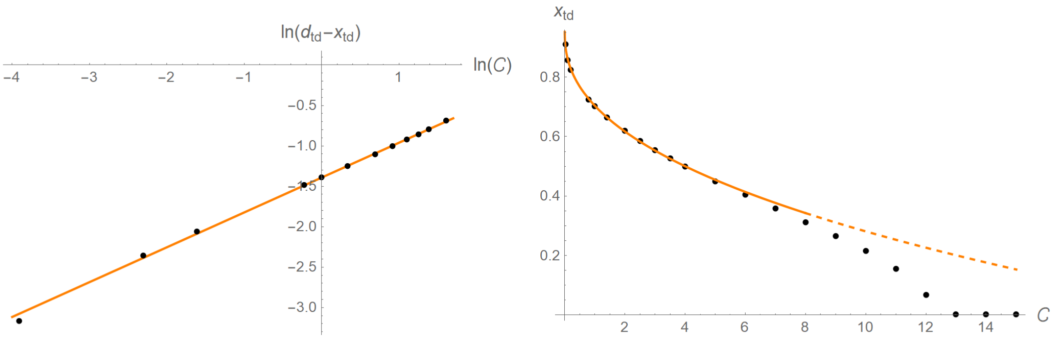

(a) Log plot (b) Linear plot

Figure 3.15: The touchdown radius as a function of $\mathcal{C}$ (black points) with a model fit (orange line) superimposed. This is for a 2D square well with Popov's divergent evaporation.

Finally we show the touchdown relationship for a 2D droplet evaporating uniformly in figure 3.16. This one has parameters $A_{\text{td}} = -0.92 \pm 0.01$, $k_{\text{td}} = 0.59 \pm 0.03$, and $d_{\text{td}} = 0.86 \pm 0.01$.

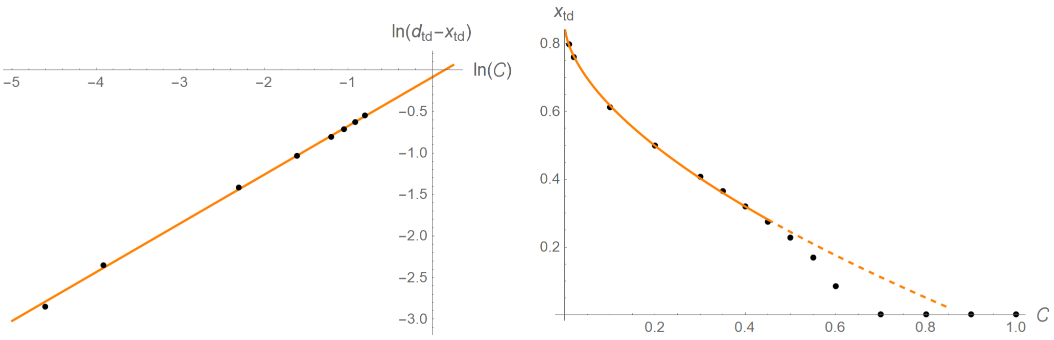

(a) Log plot (b) Linear plot

Figure 3.16: The touchdown radius as a function of $\mathcal{C}$ (black points) with a model fit (orange line) superimposed. This is for a 2D square well with uniform evaporation.

A comparison between different droplets can be seen in figure 3.17; in orange are the droplets with divergent evaporation, in blue are those with uniform evaporation. This plot reinforces our previous analysis of the similarities between the models – switching between 2D cartesian and 3D cylindrical does not have a large quantitative effect on the simulation, however changing the evaporative flux model **does** have a significant effect.

The physical interpretation of parameter d_{td} is obvious: it represents the touchdown point in the hypothetical limit of $\mathcal{C} \to 0$. For this reason, we might be surprised to see that it is not 1 in any of our four cases, which would be the natural prediction for a droplet with no capillary flow (the physical meaning of $\mathcal{C} = 0$) evaporating from a well. However, we can temper our surprise by realising that this situation would raise an inconsistency – a DiW with a pinned contact line must have flow that acts to maintain the pin. Since we always assume the DiW to be pinned to the edge of the well, our model *must* have a finite value for $\mathcal{C}$.

The other interesting parameter is k_{td}. In each case it is suspiciously close to 0.5, although usually does not equal 0.5 within statistical error (the exception being for uniform evaporation in a cylindrical well). This indicates that there may be a square-root relationship between touchdown radius and $\mathcal{C}$; the obvious question is: what does this relationship tell us about the physics? Simply rearranging equation 3.75 (with $k_{\text{td}} = 0.5$) reveals that $\mathcal{C}$ would be proportional to the area of the circle defined by the touchdown radius, but it is unclear why this ought to be the case.

Another suggestion is that $k_{\text{td}} = \frac{3}{7}$, which would fall within the estimated error for the 3D, Popov flux case. There is some precedent for this power: it has been reported before, notably in a droplet injection (rather than evaporation) paper as the relationship between the droplet height and time (which, in the authors' model, has the capillary number nondimensionalised into it) [119].

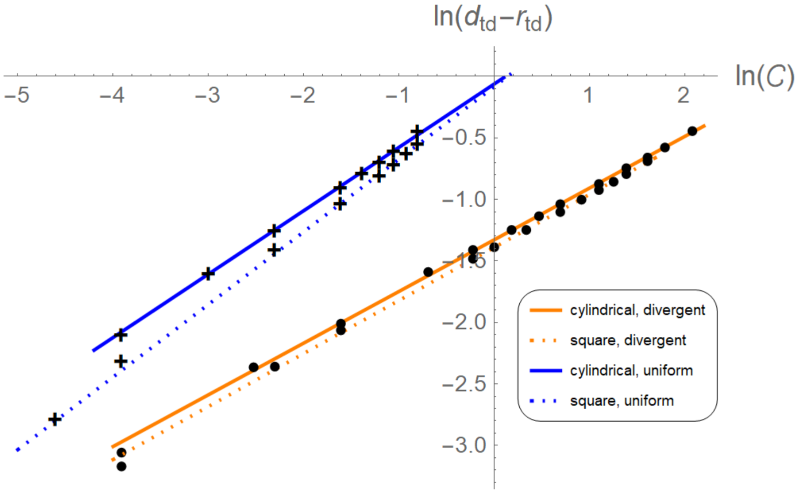

Figure 3.17: A touchdown point comparison of the four different models of DiW evaporation – cylindrical (solid lines) vs square (dotted lines) wells, and divergent (orange) vs uniform (blue) evaporative flux models.

The touchdown time, i.e. the value of t when the interface first touches the surface, is another variable that depends on parameter $\mathcal{C}$. We show the touchdown time behaviour in figure 3.18; the overall trend is that t_{td} increases with $\mathcal{C}$ sharply, then starts to decrease again slowly.

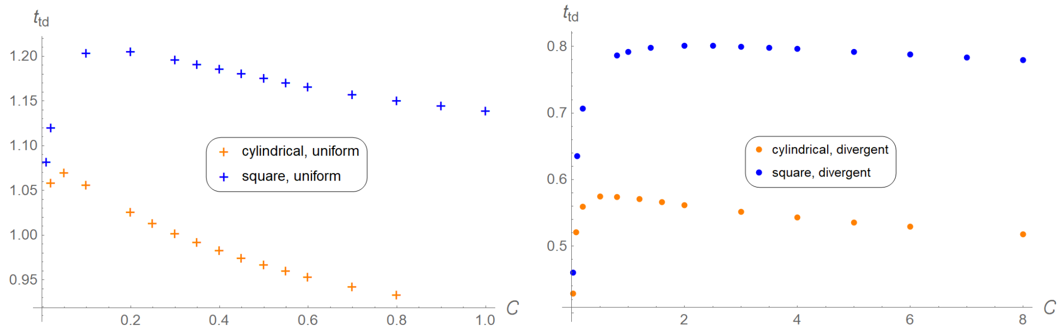

(a) Uniform evaporation (b) Popov evaporation

Figure 3.18: The relationship between touchdown time and $\mathcal{C}$ for droplets in the 2D simulation and 3D simulation and for uniform and divergent evaporation.

3.8.5 Velocity Field

The velocity field inside the droplet offers a different perspective and some new information for analysing the evolution of the droplet; for more information see chapter 2 section 2.5.

The velocity field of the droplet is given in equation 3.35, from which the height-averaged velocity can be derived,

$$\bar{u}(r,t) = \frac{\mathcal{C}h^2}{3}\frac{\partial}{\partial r}\left[\frac{1}{r}\frac{\partial}{\partial r}\left[r\frac{\partial h}{\partial r}\right]\right]. \tag{3.76}$$

We plot the average velocity as a function of r as lines evolving in time, using the time points from the corresponding height evolution plots (e.g. figures 3.19a and 3.19b use time points from figure 3.7a). We split each plot into two to emphasise the two different modes of the average velocity: it grows initially, then the fluid closer to the centre stagnates while the fluid near the edge continues to flow.

For very small values of $\mathcal{C}$, the fluid near to the centre actually flows radially inwards at the beginning of the evaporation, as can be seen in figure 3.19a. This reverse flow is an unexpected result, but is related to the compression of curves we noticed at the end of section 3.8.2, which we stated was due to a numerical artefact. Indeed, our use of a non-continuous evaporative flux (i.e. forcing the droplet to remain pinned at $r = 1$) introduces an error that propagates back through the droplet.

Because we start with a height profile that satisfies $\frac{\partial}{\partial r}\left[\frac{1}{r}\frac{\partial}{\partial r}\left[r\frac{\partial h}{\partial r}\right]\right] = 0$, the initial evolution function is just $\frac{\partial h}{\partial t} = -J(r)$, which is discontinuous at $r = 1$. However, as soon as the evaporation begins, the profile leaves its equilibrium state and the evolution function 'corrects' itself such that it becomes continuous.

Crucially, this correction propagates inwards along the droplet like a shockwave, temporarily hindering the evaporation as it does so, figure 3.20. Comparing across two orders of magnitude in $\mathcal{C}$ reveals that the shockwave dies out much more quickly (compared to the touchdown time of the droplet) when $\mathcal{C}$ is larger, figure 3.21; we recall that $\mathcal{C} \sim \mu^{-1}$ and recognise that information travels faster in a less viscous droplet, allowing it to 'correct' for the discontinuity at a faster rate. We tried to fix this problem by imposing a smoothing function to equation 3.34 (e.g. see Fischer's evaporative flux functions in chapter 2, section 2.6); although this succeeded in reducing the size of the shockwave, it was impossible to find a functional form that retained the integrated flux and maintained $J(r = 0) = 1$. Effectively, this would be a completely different DiW model.

While this shockwave does indeed represents a numerical error, we will see in section 3.8.6 that we never need to use $\mathcal{C} < 0.1$ to match the simulation to experimental data and so should not expect it to be too detrimental to our real-world comparisons. However, it is a timely reminder that simulations can sometimes sneak convincing-looking phenomena through the proverbial back door of a mathematical model.

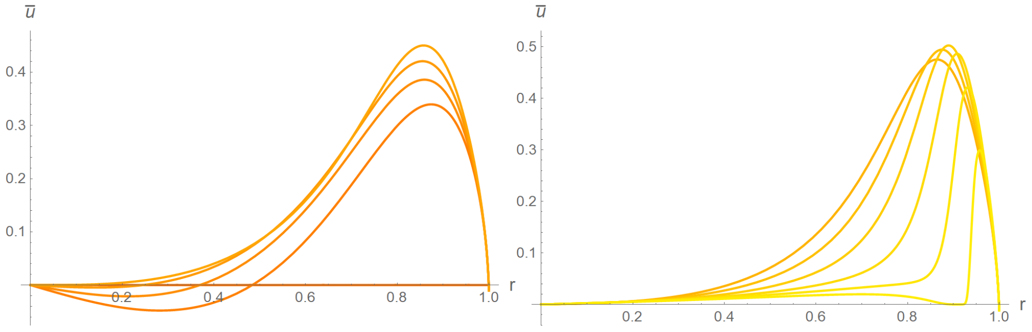

(a) $t < 0.5t_{\text{td}}$ (b) $t \geq 0.5t_{\text{td}}$

Figure 3.19: The height-averaged fluid velocity for $\mathcal{C} = 0.02$ at early and late times. Note the numerical artefact in figure (a) manifesting itself as a negative velocity at very early times.

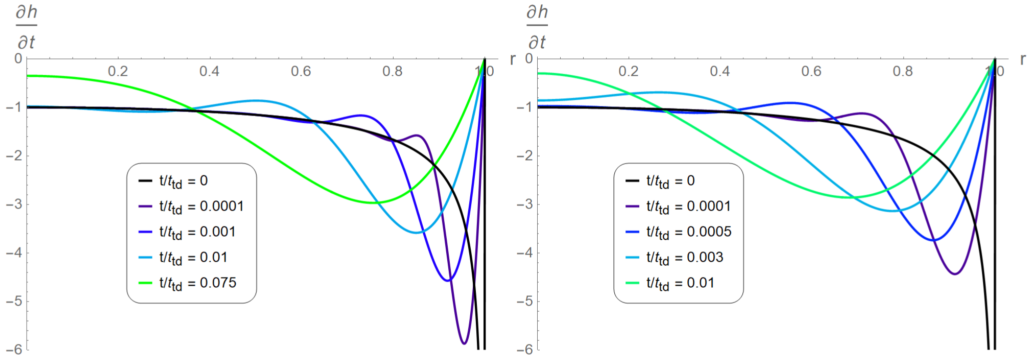

(a) $\mathcal{C} = 0.02$ (b) $\mathcal{C} = 0.2$

Figure 3.20: Early in the evaporation we observe a ‘correction shockwave’ in the height evolution equation that propagates from $r = 1$ to $r = 0$.

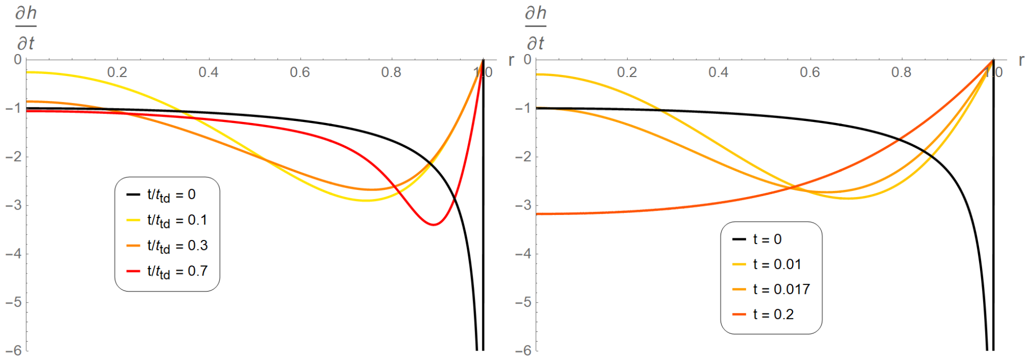

(a) $\mathcal{C} = 0.02$ (b) $\mathcal{C} = 0.2$

Figure 3.21: Later in the evaporation the shockwave disappears, but more slowly when $\mathcal{C}$ is smaller.

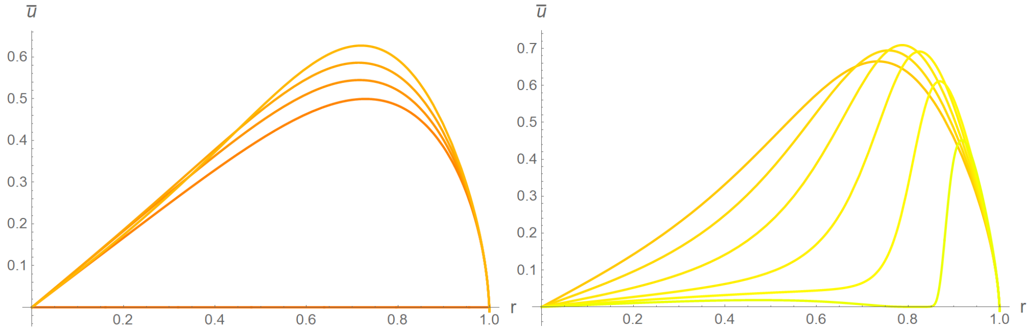

(a) $t < 0.5t_{\text{td}}$ (b) $t \geq 0.5t_{\text{td}}$

Figure 3.22: The height-averaged fluid velocity for $\mathcal{C} = 0.2$ at early and late times.

For $\mathcal{C} = 2$ the average velocity starts to decrease at about $t = 0.7t_{\text{td}}$, figure 3.23, and at about $t = 0.8t_{\text{td}}$ for $\mathcal{C} = 16$, figure 3.24.

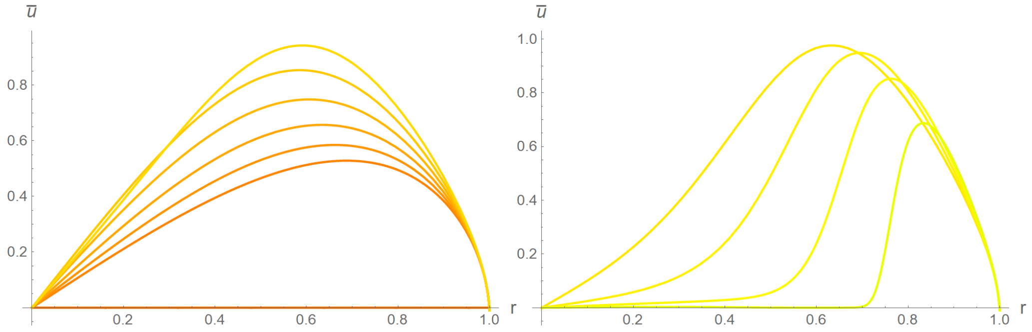

(a) $t < 0.7t_{\text{td}}$ (b) $t \geq 0.7t_{\text{td}}$

Figure 3.23: The height-averaged fluid velocity for $\mathcal{C} = 2$ at early and late times.

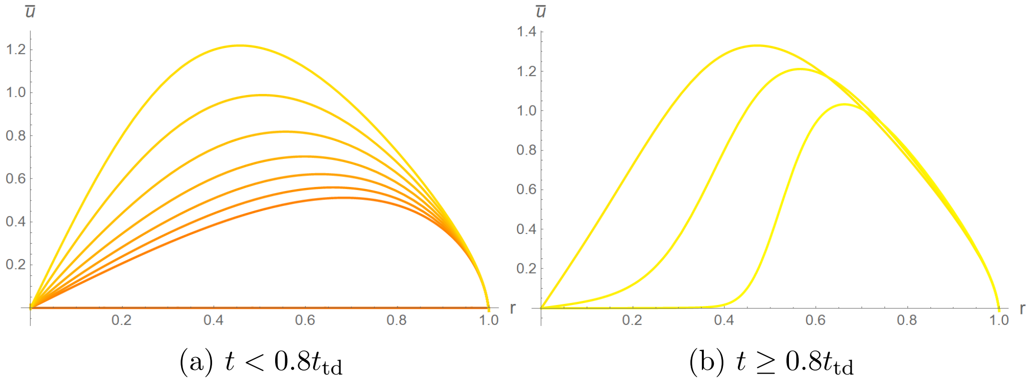

(a) $t < 0.8t_{\text{td}}$ (b) $t \geq 0.8t_{\text{td}}$

Figure 3.24: The height-averaged fluid velocity for $\mathcal{C} = 16$ at early and late times.

These graphs reveal that total fluid velocity increases slowly with $\mathcal{C}$ – from 0.02 to 16 the maximum height-averaged fluid velocity only increases by a factor of about 2.5. However, increasing $\mathcal{C}$ is associated with a more uniform velocity profile throughout the evaporation; this is evident comparing the late stage evaporation velocities, figures 3.19b with 3.24b. Central stagnation is also delayed by increasing $\mathcal{C}$; in figure 3.24 the droplet is 80% of the way to touchdown before the fluid in the centre slows down, compared to figure 3.19, where stagnation begins before the halfway point. This stagnation delay makes sense when we consider that larger $\mathcal{C}$ is associated with smaller viscosity and a lower resistance to flow.

Figures 3.25 to 3.28 are vector plots of the full velocity field for a range of droplets. The arrow direction shows the direction of the flow, while the arrow colour represents the magnitude of the horizontal component[3]. The vertical velocity can be calculated directly from the continuity equation, equation 3.18,

$$w(r,z) = \frac{\mathcal{C}}{2}\left(\left(\frac{\partial^4 h}{\partial r^4} + \frac{2}{r}\frac{\partial^3 h}{\partial r^3} - \frac{1}{r^2}\frac{\partial^2 h}{\partial r^2} + \frac{1}{r^3}\frac{\partial h}{\partial r}\right)\left(\frac{1}{3}z^3 - z^2 h\right) - z^2\frac{\partial h}{\partial r}\left(\frac{\partial^3 h}{\partial r^3} + \frac{1}{r}\frac{\partial^2 h}{\partial r^2} - \frac{1}{r^2}\frac{\partial h}{\partial r}\right)\right). \quad (3.77)$$

It is, of course, impossible to determine that a flow is nondivergent by visual inspection; however there are some suspicious looking points on some of these vector plots that should receive some additional attention. At the centre ($r = 0$) and edge ($r = 1$), we might expect the radial velocity to vanish and may be surprised to see that the figures below do not seem to reflect this. In fact, instead of imposing a zero velocity boundary condition everywhere, we have set the *average* velocity to zero at $r = 0$ and $r = 1$ (equation 3.43). This means that the model does indeed allow liquid to pass through the wall, as long as $\bar{u}$ vanishes; this is why some of the arrows in the vector plot point through $r = 1$. We must choose this kind of boundary condition in the lubrication model – choosing $u = 0$ would undesirably force the interface curvature at the boundaries. We have, however, chosen to set both components of velocity to zero at the floor. A second caveat is that the 1:1 aspect ratio in the nondimensional model visually hides information about the true aspect ratio of the

---

[3] u is the important and interesting variable here, rather than w. Additionally, w is a factor of ε smaller than u in the dimensional system and this would not be well reflected if the vector plots were coloured by velocity magnitude.

real droplet – for example, the following vector plots make it look like the vertical velocity is much steeper than it is in the long thin experimental droplets. The general trend revealed by the vector plots is that the velocity is consistently maximal near the touchdown point (this is expected due to the highly convex shape), continues to be large in the shoulder, and fluid flows in the outward radial direction nearly everywhere (the exception being for the case mentioned above, near the centre of droplets for which $\mathcal{C}$ is very small). This fits with Deegan's explanation [4] of fluid flow in a droplet with a pinned contact line, indicating that the DiW also exhibits a capillary flow that replenishes the fastest depleting material – in the case, at the contact line pin. The following figures do not each have the same colour scale for the velocity in order to maximise the range of speeds displayed by each plot.

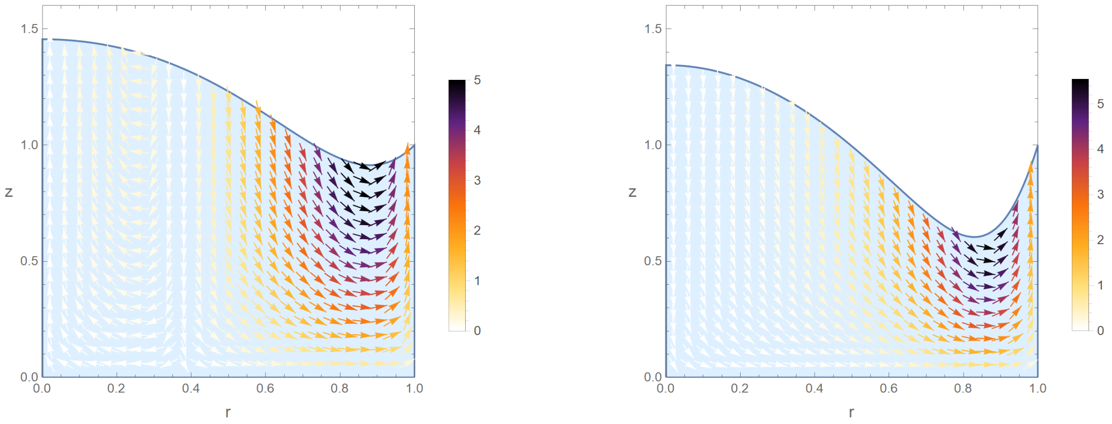

(a) $t = 0.2t_{\text{td}}$ (b) $t = 0.5t_{\text{td}}$

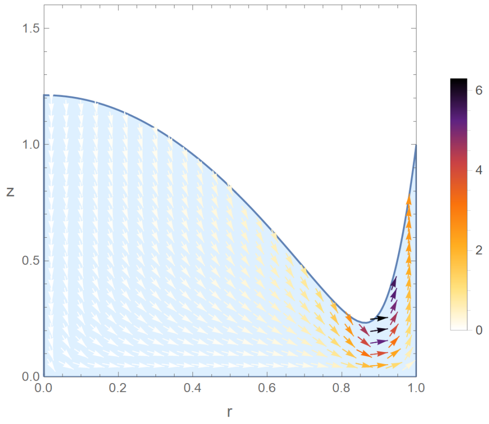

(c) $t = 0.8t_{\text{td}}$

Figure 3.25: A vector plot of the fluid velocity in a cylindrical droplet with $\mathcal{C} = 0.02$ at various times. The flow is concentrated around the dimple point, where the speed increases at later times. This is a small example of the rush hour effect.

As shown in figure 3.25, at very low values of $\mathcal{C}$ the liquid mostly moves quite slowly overall, speeding up slightly at the end of the drying and near the touchdown point and pin. This is an example of the rush-hour effect (admittedly a small example) that is described and held responsible for the CRE in a number of experimental works [17, 43, 44, 45]. While experimental questions remain as to how to quantify the rush-hour effect and its impact on the deposit (e.g. is the most important factor the absolute speed increase? Or the spatial extent of the speed increase? Or the time at which it begins to occur?), the authors report that the presence of rush-hour is key.

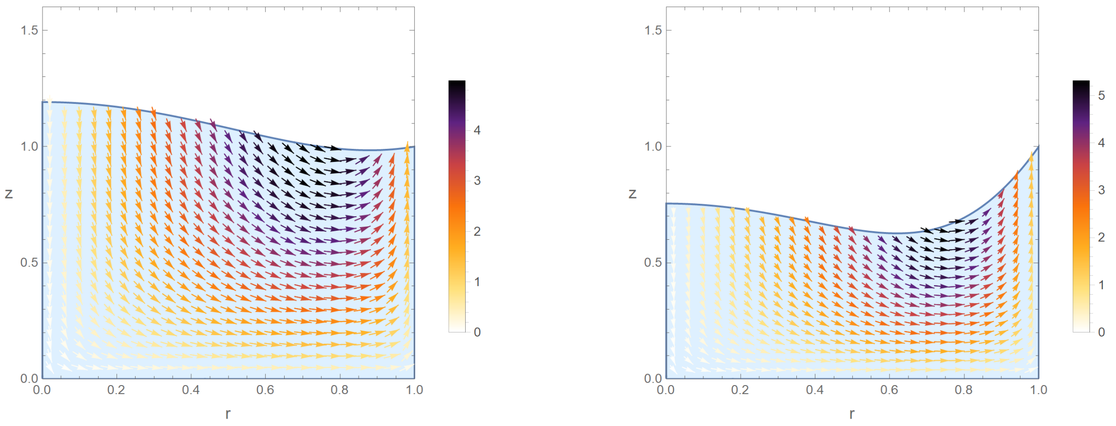

(a) $t = 0.2t_{\mathrm{td}}$

(b) $t = 0.5t_{\mathrm{td}}$

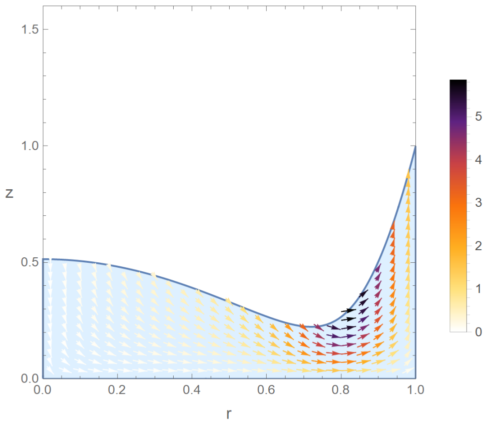

(c) $t = 0.8t_{\mathrm{td}}$

Figure 3.26: A vector plot of the fluid velocity in a cylindrical droplet with $\mathcal{C} = 0.2$ at various times. The increase in speed near the end of drying is smaller than in figure 3.25.

Figure 3.26 is similar: the droplet exhibits a small rush-hour effect near the end, localised at the edge of the well. The story is different, however, beyond $\mathcal{C} = 0.2$; in figures 3.27-3.28 rush-hour mostly disappears and the velocity at late times is instead spread out over the droplet. Its magnitude also barely increases. The loss of late-stage outer flow coincides with the transformation of the W-shaped profile to a U-shape, which fits with our understanding of the CRE.

In figures 3.27a and 3.27b, we also observe that the flow loops down and back up near the droplet surface (also visible in figure 3.28), which is a phenomenon consistent with Hu and Larson's calculations on sessile droplets with small contact angles [84]. This effect likely emerges in simulations with larger $\mathcal{C}$ because the flow is less inhibited across the droplet and liquid must flow to the pinned contact line in order to replenish material lost due to the enhanced evaporation there.

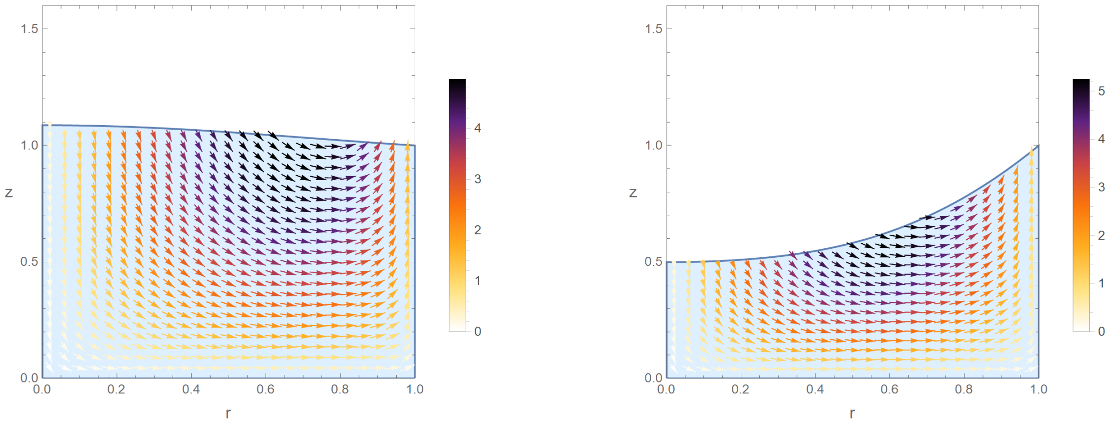

(a) $t = 0.2t_{\text{td}}$ (b) $t = 0.5t_{\text{td}}$

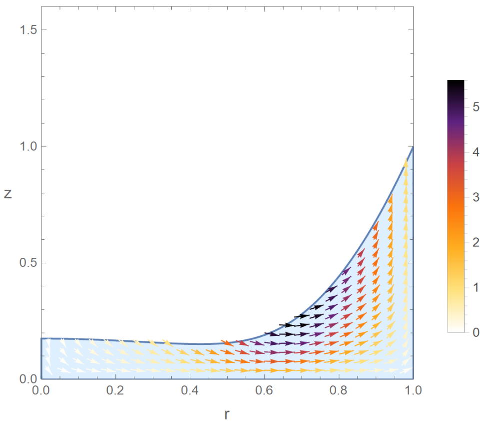

(c) $t = 0.8t_{\text{td}}$

Figure 3.27: A vector plot of the fluid velocity in a cylindrical droplet with $\mathcal{C} = 2$ at various times.

These plots potentially offer us more insight into the CRE in pure DiWs. It is evident that the smaller $\mathcal{C}$ droplets have flow that is localised to the edge of the droplet, particularly near the end of the drying process (see figure 3.25c); the regions of highest velocity move towards the centre as we increase $\mathcal{C}$ and the distribution of flow is spread out more evenly (compare figures 3.19-3.24). All this indicates that the CRE is likely to decrease as $\mathcal{C}$ gets bigger because it is associated with high velocity at the edge (see section 2.5), which is in agreement with what we already know about W-, U-, and C- shape profiles.

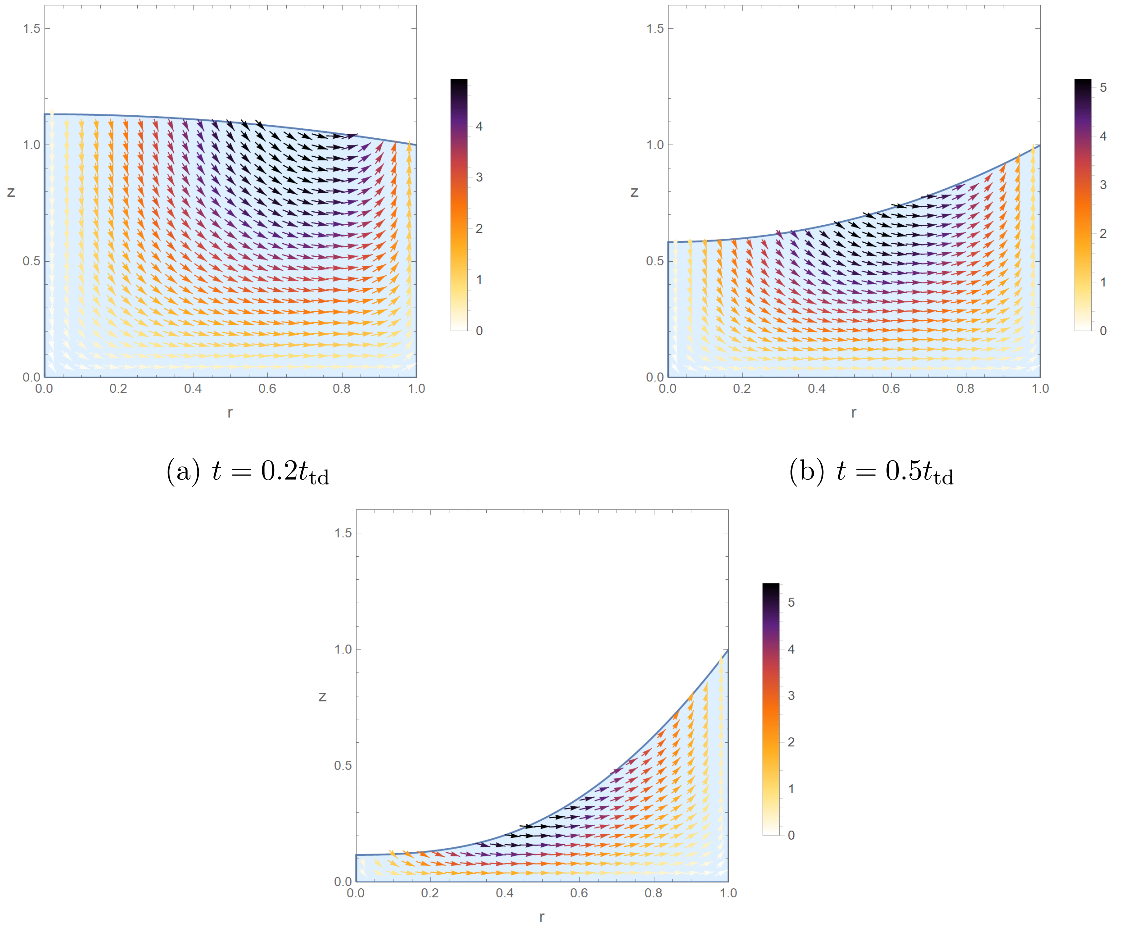

(a) $t = 0.2t_{\text{td}}$

(b) $t = 0.5t_{\text{td}}$

(c) $t = 0.8t_{\text{td}}$

Figure 3.28: A vector plot of the fluid velocity in a cylindrical droplet with $\mathcal{C} = 16$ at various times. The flow is no longer concentrated at a single point near the end of drying, but is instead spread out across the whole droplet. There is also nearly no increase in flow speed.

3.8.6 Comparison to Experimental Data

Experimental analogues of this simulation were performed by Zhida Huang and Teresa Colosimo – while it is beyond the scope of this project to go into detail about the experiments, it is worth briefly outlining the process they took to acquire the data.

The experimentalists deposited picolitre size droplets (of pure or mixed composition) into shallow cylindrical wells. The droplets were allowed to evaporate under ambient conditions (normal atmospheric pressure, normal air composition, controlled room temperature between 10°C and 25°C) and illuminated from below by a cold, monochrome light source. They used thin-film interferometry to measure the height profile of the droplet during its evaporation. A schematic diagram of the experimental set-up is found in figure 3.29, taken from [3].

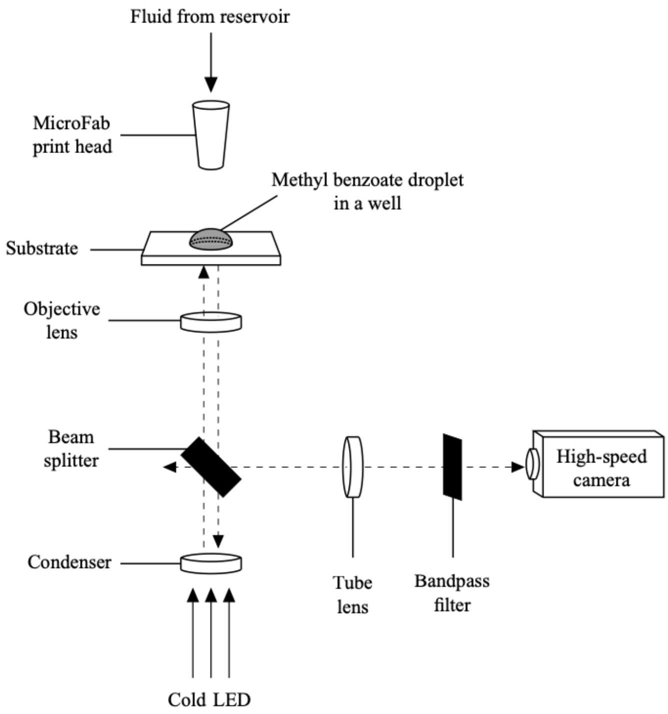

Figure 3.29: Experimental set-up used in Bain group lab, which used interferometry techniques to measure the height profile of DiWs [3].

The assumptions of the model are consistent with the method used in the experiments, so it is possible to compare the two. In this section we will present a few experiment-theory comparisons for pure droplets and discuss their significance. In each case, the experiment starts at a time $t = 0$ when the fringes first become clearly visible (importantly, this is in general **not** immediately after being printed) and we determine the time-offset with the model by fitting the curves to the data at $r = 0$. First, figure 3.30 shows experimental data for the evaporation of anisole at 10°C (crosses) plotted against a simulation (solid lines). At this temperature the anisole-air interface has surface tension $\sigma = 36.9\ \mathrm{mN} \cdot \mathrm{m}^{-1}$, anisole has viscosity $\mu = 1.31$ mPa · s, and the overall evaporative flux was $E = 1.02\,\mu\mathrm{m} \cdot \mathrm{s}^{-1}$. The well used for this experiment had dimensions $R = 75\,\mu\mathrm{m}$ and $h_0 = 1.12\,\mu\mathrm{m}$, meaning the aspect ratio was $\varepsilon = 0.01493$ and $\mathcal{C} = 1.38$.

A simulation with a fitted value of $\mathcal{C} = 0.55$ (figure 3.30) shows good agreement with the experimental data. The discrepancy between the fitted and experimental values of $\mathcal{C}$ could be a result of a number of a factors, but perhaps the most important is the shape of the well. We can see that our model is strongly dependent on the aspect ratio; ε is raised to the third power in $\mathcal{C}$. Therefore, any small error in the manufacture or measurement of the well will propagate to the third power. The interferometry depth measurements also become increasingly difficult towards the edge of the well (and impossible at the very edge), meaning it is hard to determine the precision of the pin – does contact line depinning ever occur? If so, the aspect ratio of the well will not exactly match that of the droplet, another possible source of $\mathcal{C}$-parameter discrepancy. D'Ambrosio et al. point out in their similar model that their good experimental-theoretical agreement points to minimal de-pinning of the contact line [3]; it may be that our numerical discrepancy indicates some de-pinning in the experiments. De-pinning and problematic edge measurements might

also explain the small disagreement between experiment and theory that we see in the shoulder of the droplet towards to end of the drying.
It is clear that, despite these discrepancies, the simulation is largely accurate and predicts the droplet shape well, particularly the lens shape in the centre.

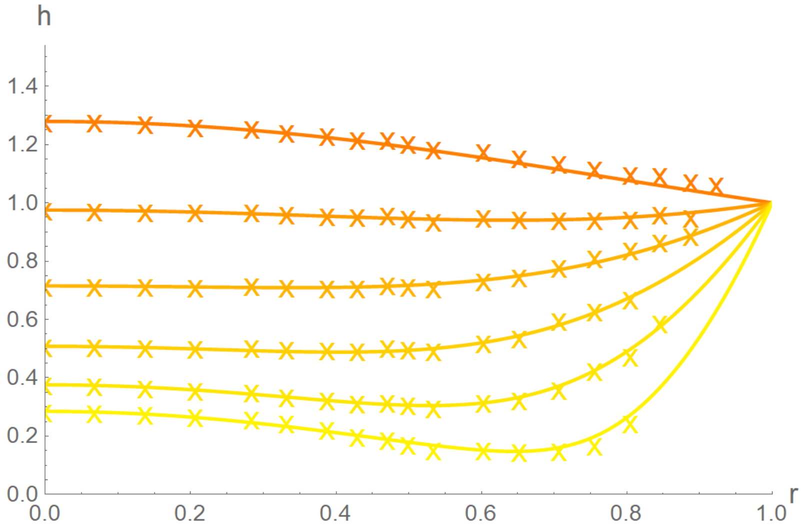

Figure 3.30: Simulation (lines) superimposed on experimental data (crosses) for anisole at 10°C.

The discrepancy in $\mathcal{C}$ is apparent in other examples too; figure 3.31 is anisole again, this time with data taken at 25°C. In this case the parameters are $\sigma = 35.0\ \mathrm{mN} \cdot \mathrm{m}^{-1}$, $\mu = 1.00\ \mathrm{mPa} \cdot \mathrm{s}$, $E = 2.69\,\mu\mathrm{m} \cdot \mathrm{s}^{-1}$, $R = 75\,\mu\mathrm{m}$, $h_0 = 1.13\,\mu\mathrm{m}$, ε =0.01507, and $\mathcal{C}$ =0.67. The simulation that best matches the data has $\mathcal{C} = 0.25$.
Again, the shape of the central lens is well preserved by the simulation, while there remains some slight disagreement towards the edge of the well. This time it is the other way around: the simulated droplet appears to evaporate too quickly (most clearly visible in the final line).

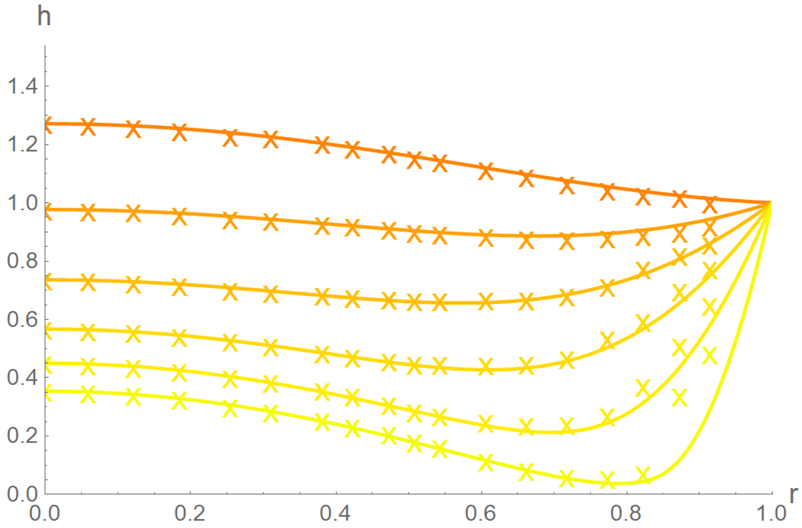

Figure 3.31: Simulation (lines) superimposed on experimental data (crosses) for anisole at 25°C.

Figure 3.32 shows data for methyl anisole at 25°C ($\sigma = 32.9$ mN $\cdot$ m^{-1}, $\mu = 1.08$ mPa $\cdot$ s, $E = 0.98\,\mu\text{m} \cdot \text{s}^{-1}$, $R = 75\,\mu\text{m}$, $h_0 = 1.10\,\mu\text{m}$, ε =0.01467, and $\mathcal{C}$ =1.43) and demonstrates that the model predicts the droplet shape even up to and including the moment of touchdown. Once again, the lens shape is accurately predicted by the model, but the shoulder near the edge features some slight disagreement and we have fitted $\mathcal{C} = 0.56$.

The $\mathcal{C}$-parameter discrepancy in these three examples is consistently a factor of about 2.5. If we estimate that the aspect ratio of the well has a small error of 3%, the total $\mathcal{C}$-parameter error would be approximately 9% – not nearly enough to explain the large divergence we observe between predicted and experimental values. Even ascribing the same magnitude of error to the other parameters – due to measuring the evaporation rate and thermal/humidity fluctuations affecting surface tension and viscosity – we are not able to fully account for such a large gap.

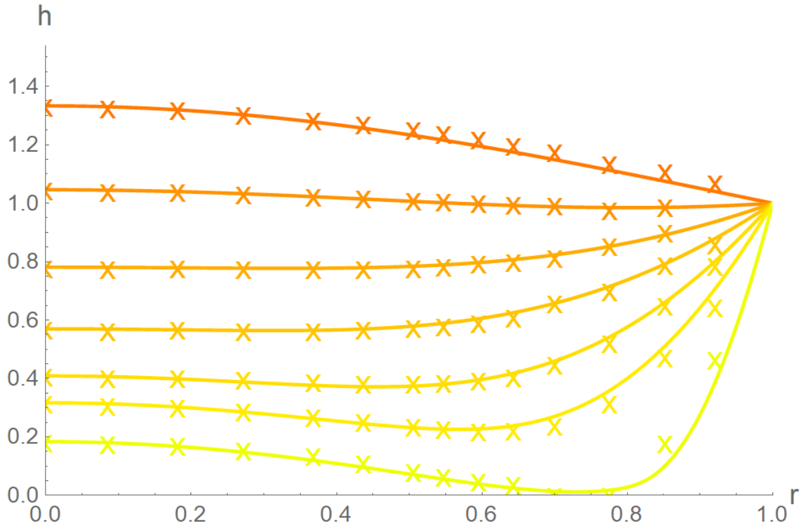

Figure 3.32: Simulation (lines) superimposed on experimental data (crosses) for methyl anisole at 25°C.

We have already shown that the simulation can produce a droplet that never forms a lens shape, which corresponds to a situation with larger $\mathcal{C}$. Figure 3.33, with data taken from methyl benzoate at 10°C ($\sigma = 37.3$ mN $\cdot$ m^{-1}, $\mu = 1.96$ mPa $\cdot$ s, $E = 0.31\,\mu\text{m} \cdot \text{s}^{-1}$, $R = 75\,\mu\text{m}$, $h_0 = 1.28\,\mu\text{m}$, $\varepsilon = 0.01707$, and $\mathcal{C}$ =5.20), demonstrates this; here the simulation has $\mathcal{C} = 9$, the only instance of the simulated parameter being larger than the experimental one.

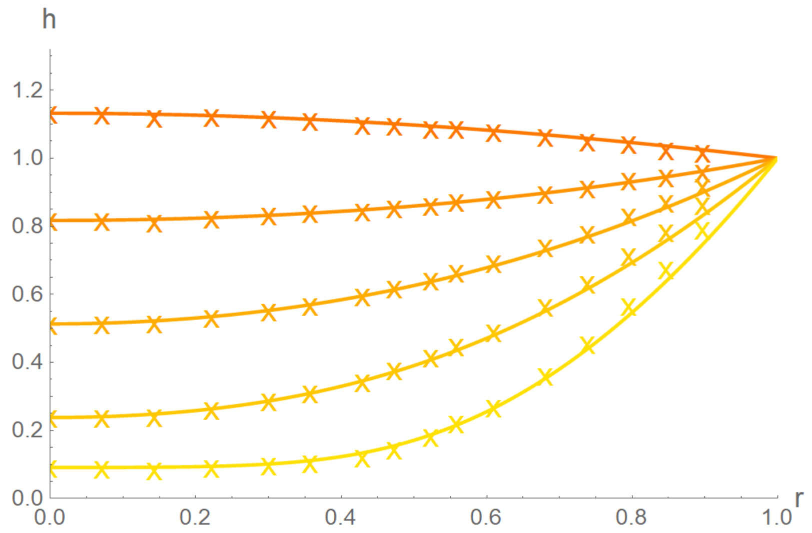

Figure 3.33: Simulation (lines) superimposed on experimental data (crosses) for methyl benzoate at 10°C.

As these figures show, the model is qualitatively very accurate: it predicts the general shape trends well, particularly the suppression of the lens with increasing $\mathcal{C}$. We also find good quantitative agreement with an adjusted value of $\mathcal{C}$.

3.9 Conclusion

In this first chapter we have built a simple model for a droplet evaporating from a well, starting with the Navier-Stokes and continuity equations to construct a lubrication PDE. Applying the lubrication approximation afforded us analytical progress, but limits the model to very shallow wells, small contact angles (largely hydrophilic surfaces), and laminar flow.

We discretised it using a finite difference scheme, and solved the resulting system of ODEs using Mathematica. We tested its numerical stability and found its cumulative error to approach zero as the number of discretisation points approached ∞.

We discovered that the pure droplet forms three types of shape as it dries, depending on the size of the $\mathcal{C}$ parameter: for small $\mathcal{C}$ W-shapes, for larger $\mathcal{C}$ U-shapes, and for larger $\mathcal{C}$ again, C-shapes. We discussed why this makes intuitive sense based on the size of the well, the surface tension and viscosity of the liquid, and the evaporation rate. We documented some important features of the DiW simulation, including the surface curvature, touchdown point, and velocity fields across a range of values of $\mathcal{C}$.

Importantly, the velocity field plots revealed that the flows in the droplets are largely behaving as we would expect: we have reproduced strong, outward flows that Deegan investigated and the rush-hour phenomenon in droplets with small $\mathcal{C}$-parameter, both of which contribute to the CRE.

Finally, we compared the simulations to experimental data, showing that we can achieve good agreement, but only if we modify the $\mathcal{C}$ parameter. The most probable explanations for this discrepancy are the imperfections in well geometry and unexpected droplet behaviour at the corners of the well. However, the experimental data show the same kinds of curvature that we can produce in our simulations; there is no behaviour that we are unable to reproduce.

We would now like to extend the model to include droplets composed of two liquids, or binary droplets, in order to investigate the effects of surface tension gradients, variable evaporation, and changing viscosity on the evolution of a DiW. In the next chapter we shall derive the equations we need to do this and simulate their evaporation in a similar way to the pure droplets in this chapter.

Chapter 4

Binary Droplet

Having investigated the evolution of pure DiWs and documented some of their properties as they dry, we can start to add complexity to the model; in this chapter we will derive equations for an evaporating droplet of binary composition, focusing on the important quantities of surface tension and evaporative flux for each of the two components, and examine the simulation solutions. It will become clear that, although the model may initially look similar, the inclusion of Marangoni flows and variable composition can lead to somewhat exotic effects.

We will see that the preferential evaporation at the edge of the droplet will lead to regions of enrichment and depletion that, in turn, give rise to complex flow patterns and different interface shapes. We will be able to examine the effects of including involatile components to give some insight into the deposition patterns created by DiWs; we will find it useful also to be able to adjust the viscosity to account for a wider variety of materials, including polymers.

Using the same velocity field plots as in chapter 3, we can investigate the conditions under which we observe inward and, occasionally, recirculating flows, as reported in the literature for systems with Marangoni effects. Such currents are often considered critical in the the battle against the CRE, so it will be important to identify if our model can reproduce them.

These new shapes, inward/recirculating flows, and Marangoni-induced rush hour suppression and enhancement are here observed in a numerical DiW simulation for the first time; all of these phenomena can be used to control the behaviour of the CRE and influence the uniformity of the deposit in a pixel.

Finally, just as in the previous chapter, we can compare the binary DiW model to experimental data in order to determine the extent of its qualitative predictive power.

4.1 Problem Description

We consider a droplet inscribed in a cylindrical well now composed of two miscible liquids, represented by χ and ξ, each with constant diffusivity in the mixture D_l. The binary droplet schematic diagram is shown in figure 4.1; the variable $\chi(\hat{r},\hat{t})$ denotes the volume fraction of one of the components.[1]

---

[1] although there are now two components, there is still only one more degree of freedom because the volume fraction of the other component is given by $\xi(\hat{r},\hat{t}) = 1 - \chi(\hat{r},\hat{t})$

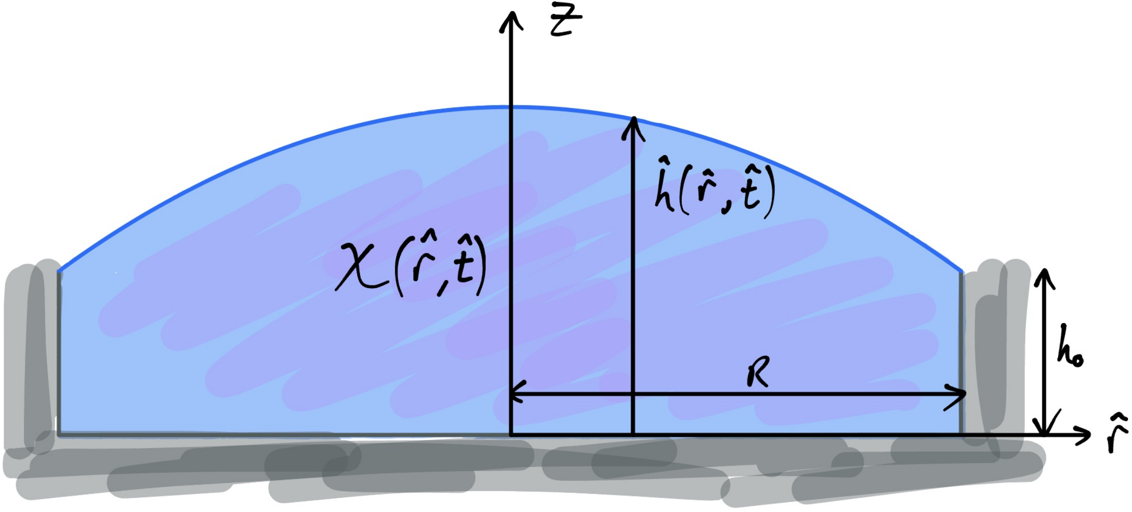

Figure 4.1: A binary droplet in a cylindrical well. The droplet is evaporating into an inert atmosphere devoid of components χ and ξ.

4.2 Fluid Dynamics

The fluid dynamics for the binary droplet are largely the same as that for a pure droplet; equations 3.1 to 3.11 still apply (so too their dimensionless analogues), however if the evaporation rates and surface tensions of the two liquids are different, non-uniform local concentrations and Marangoni forces may appear. This is encoded in the interface stress conditions (equations 3.4 and 3.6), which retain their dependence on droplet surface tension, leading to Marangoni forces acting on the liquid. In this case, the evaporative flux is a function of the composition because both components have different evaporation rates, $\hat{J}_\chi$ and $\hat{J}_\xi$, in general.
We can quantify the difference in evaporation rate between the two species with a parameter α, defined through

$$\hat{J}_\chi = (1-\alpha)\hat{J}_\xi\,; \tag{4.1}$$

because we always take χ to represent the less volatile component, α is a positive constant between 0 and 1. Assuming the liquid mixture behaves ideally and obeys Raoult's law [120], the total evaporation rate becomes

$$\hat{J}(\hat{r},\hat{t},\chi) = \frac{2D_{\text{inert}}M_m^c(c_0-c_\infty)}{\pi}\frac{1-\alpha\chi(\hat{r},\hat{t})}{\sqrt{R^2-\hat{r}^2}}\,, \tag{4.2}$$

where D_{inert} is the diffusivity of components χ and ξ in the inert gas[2] and c_0 and c_∞ are the saturation and ambient concentrations of liquid vapour at the interface and infinitely far from the droplet respectively. It is worth noting the two approximations at play here.
First, a droplet with a composition that varies spatially does not, in general, have an evaporative flux that follows Popov's pure droplet form. Instead, the evaporative flux of each component will depend on the concentration field near to the interface,

---

[2] Assuming they both have the same diffusivity in inert gas. The chemicals that we will be comparing with are likely to adhere to this assumption approximately.

which itself depends on the liquid volume fraction. We will explore this more in chapter 5.

Second, we assume that both components behave identically in the gas phase, hence their diffusion coefficients are equal. This is a good approximation for molecules of similar sizes and weights, but could be adjusted if not.

The surface tensions can be related similarly with a parameter β, defined through

$$\sigma_\chi = (1-\beta)\sigma_\xi \tag{4.3}$$

giving a total surface tension of

$$\sigma(\chi) = \sigma_\xi(1-\beta\chi(\hat{r},\hat{t})). \tag{4.4}$$

β can be either positive (meaning the more volatile component has higher surface tension) or negative (meaning the more volatile component has lower surface tension). In this work we assume that the only Marangoni forces present are solutal in origin, however it is very possible that there will be thermal Marangoni effects active in reality. We make this assumption because the experimental research to which we compare our model reports no significant therm effects. Although our analysis is thus concerned with a simpler, solutal Marangoni situation, we could have included thermal effects by including a new thermal surface tension term, $\sigma_{\text{th}} \propto \Theta$, and solved the Laplace equation in the droplet for temperature, $\nabla^2\Theta = 0$, with appropriate boundary conditions for evaporative cooling along the interface and constant temperature along the substrate. This type of analysis has been done many times before in sessile droplets [84, 121, 122].

We assume that component χ can be well described by a convection-diffusion equation,

$$\frac{D\chi}{D\hat{t}} = D_l\hat{\nabla}^2\chi, \tag{4.5}$$

where D_l is the mutual diffusion coefficient of each component in the liquid mixture. Equation 3.7 can be decomposed into a mass transfer equation for each component at the interface,

$$\chi(\hat{\boldsymbol{u}}\cdot\hat{\boldsymbol{n}} - \hat{V}_n) - D_l\hat{\nabla}\chi\cdot\hat{\boldsymbol{n}} = \frac{1}{\rho}\hat{J}_\chi\chi \tag{4.6}$$

$$\xi(\hat{\boldsymbol{u}}\cdot\hat{\boldsymbol{n}} - \hat{V}_n) - D_l\hat{\nabla}\xi\cdot\hat{\boldsymbol{n}} = \frac{1}{\rho}\hat{J}_\xi\xi, \tag{4.7}$$

and it will prove useful to have the cross-weighted difference of these equations, that is $\xi(4.6)$ $-\chi(4.7)$,

$$-D_l\hat{\boldsymbol{n}}\cdot\hat{\nabla}\chi = \frac{\chi\xi}{\rho}(\hat{J}_\chi - \hat{J}_\xi)\,, \tag{4.8}$$

as well as their sum,

$$\hat{\boldsymbol{u}}\cdot\hat{\boldsymbol{n}} - \hat{V}_n = \frac{1}{\rho}\hat{J}(\hat{r},\hat{t},\chi)\,. \tag{4.9}$$

There are additional boundary conditions to impose with the inclusion of another liquid; there is no flux through the base

$$\hat{w}\chi - D_l \frac{\partial \chi}{\partial \hat{z}} = 0 \text{ at } \hat{z} = 0 \tag{4.10}$$

nor through the wall, nor net flux across the centre

$$\hat{u}\chi - D_l \frac{\partial \chi}{\partial \hat{r}} = 0 \text{ at } \hat{r} = 0, R\,. \tag{4.11}$$

4.3 Non-Dimensionalisation

Using the scalings presented in section 3.3, these equations become

$$\varepsilon^2 \mathrm{Pe}\Big(\frac{\partial \chi}{\partial t} + u\frac{\partial \chi}{\partial r} + w\frac{\partial \chi}{\partial z}\Big) = \varepsilon^2 \frac{1}{r}\frac{\partial}{\partial r}\Big[r\frac{\partial \chi}{\partial r}\Big] + \frac{\partial^2 \chi}{\partial z^2}\,, \tag{4.12}$$

$$J(r,t,\chi) = \frac{1-\alpha\chi}{\sqrt{1-r^2}}\,, \tag{4.13}$$

$$-\varepsilon^2 \frac{\partial h}{\partial r}\frac{\partial \chi}{\partial r} + \frac{\partial \chi}{\partial z} = \frac{\varepsilon^2 \mathrm{Pe}\;\chi(1-\chi)\alpha}{\sqrt{1-r^2}} \text{ at } z = h\,, \tag{4.14}$$

$$w - u\frac{\partial h}{\partial r} - \frac{\partial h}{\partial t} = J(r,t,\chi) \text{ at } z = h\,, \tag{4.15}$$

$$\varepsilon^2\;\mathrm{Pe}\; w\chi - \frac{\partial \chi}{\partial z} = 0 \text{ at } z = 0\,, \tag{4.16}$$

$$\mathrm{Pe}\; u\chi - \frac{\partial \chi}{\partial r} = 0 \text{ at } r = 0, 1\,, \tag{4.17}$$

where Pe is the Péclet number $\mathrm{Pe} = \frac{UR}{D_l} \sim \frac{D_{\mathrm{inert}}}{D_l}\frac{M_m^c(c_0 - c_\infty)}{\rho}$. We can estimate the magnitude of the Péclet number if we assume that $D_{\mathrm{inert}} \sim 10^{-1}\,\mathrm{cm\,s^{-1}}$ [123], $D_l \sim 10^{-6}\,\mathrm{cm\,s^{-1}}$ [124], $M_m^c c_0 \sim 10^{-5}$ and $c_\infty = 0$ [9], and using the density of water, $\rho \sim 10^0$; this gives $\mathrm{Pe} \sim 1$. Of course, some of these estimates may be inaccurate: we would often like to model chemicals with density less than that of water and with higher vapour pressure (toluene, IPA, ethanol), in which case the Péclet number could rise as high as $\mathrm{Pe} \sim 10$. Also, it is difficult to estimate values for the diffusion coefficient of a liquid chemical in another liquid chemical, meaning there is uncertainty about the value of D_l. For the purpose of this thesis, we have taken $\mathrm{Pe} = 10$ unless otherwise stated, because we are more interested in studying the flow due to capillary and Marangoni forces than diffusion. However, we will briefly investigate the impact of diffusion in sections 4.7.1 and 4.7.2.

The mass continuity and Navier-Stokes equations are the same as for the pure droplet case,

$$\frac{1}{r}\frac{\partial}{\partial r}[ru] + \frac{\partial w}{\partial z} = 0, \tag{4.18}$$

$$\frac{\partial^2 u}{\partial z^2} = \frac{\partial p}{\partial r}, \tag{4.19}$$

$$\frac{\partial p}{\partial z} = 0\,, \tag{4.20}$$

but the normal stress condition is modified by the binary mixture

$$p = -\frac{\sigma_\xi \varepsilon^3}{\mu U r}(1-\beta\chi(r,t))\frac{\partial}{\partial r}\left[r\frac{\partial h}{\partial r}\right] \text{ at } z = h\,, \tag{4.21}$$

where we make the crude assumption that the viscosity, μ, is the average viscosity of the two liquids and is independent of composition. We will explore viscosity variation in section 4.7.4.

This reverts to equation 3.21 under $\beta\chi \ll 1$,[3] meaning we use the surface tension of the more volatile component for $\mathcal{C} = \frac{\sigma_\xi \varepsilon^3}{\mu U}$. For the tangential stress interface condition, we now have

$$\frac{\partial u}{\partial z} = \mathcal{M}\frac{\partial \chi}{\partial r} \text{ at } z = h\,. \tag{4.22}$$

where $\mathcal{M} = -\frac{\beta\mathcal{C}}{\varepsilon^2}$ is the Marangoni number. The no-slip and no-flux conditions apply as previously

$$u = w = 0 \text{ at } z = 0 \tag{4.23}$$

and

$$h = 1,\ q = 0 \text{ at } r = 1. \tag{4.24}$$

The two initial conditions are

$$h = h^*(r) \text{ at } t = 0 \tag{4.25}$$

and

$$\chi = \chi^*(r) \text{ at } t = 0. \tag{4.26}$$

4.4 Deriving the Lubrication Equations

This time we have two differential equations to derive: one for the evolution of the droplet height and one for its composition. We shall start with the height lubrication equation, which follows a similar path to the pure droplet case.

4.4.1 Height Evolution Equation

We first derive a velocity profile by integrating equation 4.19 twice and using the stress conditions

$$u(r,z) = -\mathcal{C}\frac{\partial}{\partial r}\left[\frac{1}{r}\frac{\partial}{\partial r}\left[r\frac{\partial h}{\partial r}\right]\right]\left(\frac{1}{2}z^2 - zh\right) + \mathcal{M}\frac{\partial \chi}{\partial r}z \tag{4.27}$$

and

$$\bar{u}(r,t) = \frac{\mathcal{C}h^2}{3}\frac{\partial}{\partial r}\left[\frac{1}{r}\frac{\partial}{\partial r}\left[r\frac{\partial h}{\partial r}\right]\right] + \frac{\mathcal{M}h}{2}\frac{\partial \chi}{\partial r}, \tag{4.28}$$

---

[3] this approximation means that the model is valid only for small β.

and the rest of the derivation is identical to the pure droplet case in chapter 3: we integrate mass continuity, equation 4.18 over the height of the droplet, considering the substrate impermeability (equation 4.23b), then use the Leibniz integral rule on the mass transfer condition (equation 4.15) to acquire an equation for the height evolution,

$$\frac{\partial h}{\partial t} = -\frac{\mathcal{C}}{3r}\frac{\partial}{\partial r}\left[rh^3\frac{\partial}{\partial r}\left[\frac{1}{r}\frac{\partial}{\partial r}\left[r\frac{\partial h}{\partial r}\right]\right]\right] - \frac{\mathcal{M}}{2r}\frac{\partial}{\partial r}\left[rh^2\frac{\partial \chi}{\partial r}\right] - \frac{1-\alpha\chi}{\sqrt{1-r^2}}. \tag{4.29}$$

It is helpful to refer to the three terms on the right hand side of this equation by what they describe: the first term is Laplace-driven flow, the second is Marangoni-driven flow, and the third is evaporation.

4.4.2 Composition Evolution Equation

At this point we might well notice that the model still contains many instances of the parameter ε (equations 4.12, 4.14 and 4.16), which we had previously neglected because it is very small. The way we did this previously was to express each variable as a series expansion in ε^2, that is for any variable f

$$f(r,z,t,...) = f_0(r,z,t,...) + f_1(r,z,t,...)\varepsilon^2 + f_2(r,z,t,...)\varepsilon^4 + ...\,, \tag{4.30}$$

and look at the problem at zero order. We shall indeed do this again, but also inspect the problem at first order afterwards.

Zero Order Problem

At zero order we neglect all terms in ε^2 and smaller, equation 4.12 becomes

$$\frac{\partial^2 \chi_0}{\partial z^2} = 0 \tag{4.31}$$

with boundary conditions 4.14, 4.16 and 4.17

$$\frac{\partial \chi_0}{\partial z} = 0 \ \text{ at } \ z = h\,, \tag{4.32}$$

$$\frac{\partial \chi_0}{\partial z} = 0 \ \text{ at } \ z = 0\,, \tag{4.33}$$

$$\mathrm{Pe}\, u\chi_0 - \frac{\partial \chi_0}{\partial r} = 0 \ \text{ at } \ r = 0, 1\,. \tag{4.34}$$

This system has a simple solution:

$$\chi_0 = \chi_0(r,t)\,, \tag{4.35}$$

i.e. the composition is independent of z.

First Order Problem

We now take all terms at first order in ε^2; equation 4.12 is

$$\mathrm{Pe}\Big(\frac{\partial\chi_0}{\partial t}+u\frac{\partial\chi_0}{\partial r}\Big)=\frac{1}{r}\frac{\partial}{\partial r}\Big[r\frac{\partial\chi_0}{\partial r}\Big]+\frac{\partial^2\chi_1}{\partial z^2}, \tag{4.36}$$

and, integrating over the height of the droplet, becomes

$$h\mathrm{Pe}\Big(\frac{\partial\chi_0}{\partial t}+\bar{u}\frac{\partial\chi_0}{\partial r}\Big)=h\frac{1}{r}\frac{\partial}{\partial r}\Big[r\frac{\partial\chi_0}{\partial r}\Big]+\Big[\frac{\partial\chi_1}{\partial z}\Big]_0^h. \tag{4.37}$$

At first order the boundary conditions are

$$\frac{\partial\chi_1}{\partial z}=0 \ \text{ at } \ z=0 \tag{4.38}$$

and

$$\frac{\partial\chi_1}{\partial z}=\frac{\partial h}{\partial r}\frac{\partial\chi_0}{\partial r}+\frac{\mathrm{Pe}\,\alpha\,\chi_0(1-\chi_0)}{\sqrt{1-r^2}} \ \text{ at } \ z=h. \tag{4.39}$$

We notice that we can eliminate χ_1 from equation 4.37 using these boundary conditions, and the equation emerges as (with subscripts dropped for clarity, but all χs should be understood to be of zero order)

$$\begin{aligned}\frac{\partial\chi}{\partial t}=-\Big(\frac{\mathcal{C}h^2}{3}\frac{\partial}{\partial r}\Big[\frac{1}{r}\frac{\partial}{\partial r}\Big[r\frac{\partial h}{\partial r}\Big]\Big]+\frac{\mathcal{M}h}{2}\frac{\partial\chi}{\partial r}\Big)\frac{\partial\chi}{\partial r}&\\ +\frac{1}{\mathrm{Pe}}\Big(\frac{1}{r}\frac{\partial}{\partial r}\Big[r\frac{\partial\chi}{\partial r}\Big]+\frac{1}{h}\frac{\partial h}{\partial r}\frac{\partial\chi}{\partial r}\Big)+\frac{1}{h}\frac{\alpha\chi(1-\chi)}{\sqrt{1-r^2}}.&\end{aligned} \tag{4.40}$$

We can see the four flow terms again: Laplace, Marangoni, diffusion, and evaporation. This system is associated with boundary conditions for symmetry,

$$\frac{\partial\chi}{\partial r}=0 \ \text{ at } \ r=0, \tag{4.41}$$

and no-flux at the wall,

$$\frac{\partial}{\partial r}\Big[\frac{1}{r}\frac{\partial}{\partial r}\Big[r\frac{\partial h}{\partial r}\Big]\Big]+\frac{3\mathcal{M}}{2\mathcal{C}}\frac{\partial\chi}{\partial r}=0. \tag{4.42}$$

Recalling equation 4.17 again, this leads to:

$$\frac{\partial}{\partial r}\Big[\frac{1}{r}\frac{\partial}{\partial r}\Big[r\frac{\partial h}{\partial r}\Big]\Big]=\frac{\partial\chi}{\partial r}=0 \ \text{ at } \ r=1. \tag{4.43}$$

4.5 Two Dimensional Version

Performing the same process for a two-dimensional droplet in a square well in cartesian space gives a similar system of equations:

$$\frac{\partial h}{\partial t} = -\frac{\mathcal{C}}{3}\frac{\partial}{\partial x}\Big[h^3\frac{\partial^3 h}{\partial x^3}\Big] - \frac{\mathcal{M}}{2}\frac{\partial}{\partial x}\Big[h^2\frac{\partial \chi}{\partial x}\Big] - \frac{1-\alpha\chi}{\sqrt{1-x^2}}\,, \tag{4.44}$$

$$\frac{\partial \chi_0}{\partial t} = -\Big(\frac{\mathcal{C}}{3}h^2\frac{\partial^3 h}{\partial x^3} + \frac{\mathcal{M}}{2}h\frac{\partial \chi_0}{\partial x}\Big)\frac{\partial \chi_0}{\partial x} + \frac{1}{h\,\mathrm{Pe}}\frac{\partial}{\partial x}\Big[h\frac{\partial \chi_0}{\partial x}\Big] + \frac{\alpha}{h}\chi_0(1-\chi_0)\,, \tag{4.45}$$

$$\frac{\partial \chi}{\partial x} = 0 \;\text{ at }\; x = 0\,, \tag{4.46}$$

$$\frac{\partial^3 h}{\partial x^3} = \frac{\partial \chi}{\partial x} = 0 \;\text{ at }\; x = 1\,. \tag{4.47}$$

4.6 Numerical Methods

The numerical section for the binary droplet is very similar to section 3.7; see there for more details. We transformed the PDEs we currently have into ODEs and solved these using the method of lines in Mathematica's NDSolve function.

4.6.1 Cylindrical Well

In (r, z) the domain $r \in [0, 1]$ is discretised into N regions of width Δr; we need to take care again with the $\frac{1}{r}$ faux singularities when dealing with the cylindrical equations. The Marangoni term in the height equation can be written in terms of the function

$$rh^2\frac{\partial \chi}{\partial r} \approx g_{\mathcal{M},i+\frac{1}{2}} = \Big(i+\frac{1}{2}\Big)\frac{(h_{i+1}+h_i)^2}{4}(\chi_{i+1}-\chi_i) \tag{4.48}$$

which means

$$\frac{\partial h_i}{\partial t}\Big|_{\mathcal{M}} = -\frac{\mathcal{M}}{8i(\Delta r)^2}(g_{\mathcal{M},i+\frac{1}{2}} - g_{\mathcal{M},i-\frac{1}{2}}). \tag{4.49}$$

The evaporation term depends on r through Popov's form of the evaporative flux,

$$\frac{\partial h_i}{\partial t}\Big|_{J} = -\frac{1-\alpha\chi_i}{\sqrt{1-(i\Delta r)^2}}. \tag{4.50}$$

The composition equation is discretised similarly (here we split them into their four terms for clarity):

Laplace,

$$\begin{aligned}\frac{\partial \chi_i}{\partial t}\Big|_{\mathcal{C}} = -\frac{\mathcal{C}h_i^2}{12(\Delta r)^4}&\Big((h_{i+2}-h_{i+1}-h_i+h_{i-1}) + \frac{2}{i+\frac{1}{2}}(h_{i+1}-h_i)\\ &- (h_{i+1}-h_i-h_{i-1}+h_{i-2}) - \frac{2}{i-\frac{1}{2}}(h_i-h_{i-1})\Big)(\chi_{i+1}-\chi_{i-1});\end{aligned} \tag{4.51}$$

Marangoni,

$$\left.\frac{\partial \chi_i}{\partial t}\right|_{\mathcal{M}} = \frac{\mathcal{M} h_i}{8(\Delta r)^2}(\chi_{i+1} - \chi_{i-1})^2; \tag{4.52}$$

diffusion,

$$\left.\frac{\partial \chi_i}{\partial t}\right|_{D} = \frac{1}{\mathrm{Pe}(\Delta r)^2}\Bigg(\frac{1}{i}\bigg(\Big(i+\frac{1}{2}\Big)(\chi_{i+1}-\chi_i) - \Big(i-\frac{1}{2}\Big)(\chi_i - \chi_{i-1})\bigg) \\ + \frac{1}{4h_i}(h_{i+1}-h_{i-1})(\chi_{i+1}-\chi_{i-1})\Bigg); \tag{4.53}$$

and evaporation,

$$\left.\frac{\partial \chi_i}{\partial t}\right|_{J} = \frac{\alpha}{h_i}\frac{\chi_i(1-\chi_i)}{\sqrt{1-(i\Delta r)^2}}. \tag{4.54}$$

We need to worry about the pseudo-singularities again because of the terms in $\frac{1}{r}$; we dealt with the height Laplace term at $i = 0$, which can be found in chapter 3 (equation 3.59), here the height Marangoni term must also be expanded:

$$\frac{1}{r}\frac{\partial}{\partial r}\left[rh^2\frac{\partial \chi}{\partial r}\right] = \frac{1}{r}h^2\frac{\partial \chi}{\partial r} + 2h\frac{\partial h}{\partial r}\frac{\partial \chi}{\partial r} + h^2\frac{\partial^2 \chi}{\partial r^2}. \tag{4.55}$$

The gradient of χ vanishes at $r = 0$, so we can apply l'Hôpital's rule again until all instances of the singularity vanish,

$$\left.\frac{1}{r}\frac{\partial}{\partial r}\left[rh^2\frac{\partial \chi}{\partial r}\right]\right|_{r=0} = 2h^2\frac{\partial^2 \chi}{\partial r^2}. \tag{4.56}$$

Symmetry arguments take care of the ghost point at $i = -1$ again, rendering the height Marangoni term

$$\frac{\partial h_0}{\partial t} = \frac{2\mathcal{M}h_0^2}{(\Delta r)^2}(\chi_1 - \chi_0), \tag{4.57}$$

and the evaporation term is trivial to discretise here. In the case of the composition equation, the only part with a singularity is the first half of the diffusion term, for which

$$\frac{1}{r}\frac{\partial}{\partial r}\left[r\frac{\partial \chi}{\partial r}\right] = \frac{\partial^2 \chi}{\partial r^2} + \frac{1}{r}\frac{\partial \chi}{\partial r}. \tag{4.58}$$

L'Hôpital's rule applied at $r = 0$ gives

$$\left.\frac{1}{r}\frac{\partial}{\partial r}\left[r\frac{\partial \chi}{\partial r}\right]\right|_{r=0} = 2\frac{\partial^2 \chi}{\partial r^2}, \tag{4.59}$$

and the whole composition equation at $r = 0$ discretises to

$$\frac{\partial \chi_0}{\partial t} = \frac{2(\chi_1 - \chi_0)}{\mathrm{Pe}(\Delta r)^2} + \frac{\alpha\chi_0(1-\chi_0)}{h_0} \tag{4.60}$$

because of symmetry in χ. Symmetry in h deals with the ghost point in the composition equation at $i = 1$;

$$h_{-1} = h_1. \tag{4.61}$$

For $i = N - 1$ we have to remember the fluid flux vanishing conditions. Equation 4.43a discretises to

$$h_{N+2} + h_{N+1}(-2 + 2\Delta r - \Delta r^2) + 4\Delta r + h_{N-1}(2 + 2\Delta r + \Delta r^2) - h_{N-2} = 0 \quad (4.62)$$

and we can use the height lubrication equation 4.29 at $r = 1$ ($h = 1, h_t = 0, \bar{u} = 0$) to eliminate the h_{N+2} term, which gives an expression for h_{N+1} (after neglecting terms in $(\Delta r)^2$, except for the one multiplying the variable Marangoni-Laplace ratio),

$$\begin{aligned} h_{N+1} = (-3\Big(1 + \frac{2}{3}\Delta r\Big) &+ h_{N-1}(3 + \Delta r) - h_{N-2} \\ &+ \frac{3\mathcal{M}}{2\mathcal{C}}(\Delta r)^2(\chi_N - \chi_{N-1}))(-1 - \Delta r)^{-1}\,, \quad (4.63) \end{aligned}$$

and we can see that the modification is only significant if the Marangoni forces are much stronger than the Laplace forces, $\mathcal{M} >> \mathcal{C}$.
This solves the ghost point problem in both equations at $i = N - 1$; the composition equation is much simpler at $i = N$ because of equation 4.43b, reducing down to the diffusion term:

$$\frac{\partial \chi_N}{\partial t} = \frac{4}{\text{Pe}(\Delta r)^2}(\chi_{N-1} - \chi_N). \quad (4.64)$$

This leaves us with one height ODE and one composition ODE in time for each point along the droplet and we can now proceed with the NDSolve simulation. Again, a similar process is used to discretise the two-dimensional cartesian case.

4.7 Results

In this section we shall take a look at the simulation results of incorporating a second liquid into the evaporating droplet; we will start with some practical limiting cases and later move on to comparing binary droplets with their pure counterparts. It will become clear that the Maranogni effect has a large influence on the droplet shape, transforming the W-, U-, and C-shapes from the previous chapter in a few different ways. We will also see Marangoni-induced changes to the velocity field across the droplet; given that both the shape and the flow have been used as a proxy for deposit distribution in previous research it will be useful to examine the impact of surface tension gradients on droplet evolution. Finally, we will compare the numerical solutions to experimental data again. In all that follows, we shall use a uniform initial composition, $\chi(t = 0) = 0.4$, unless otherwise stated. We shall also start by examining negative values of β; this just means that the more volatile component has lower surface tension, which leads to more interesting results concerning the CRE.

4.7.1 Limiting Cases

There are a few limiting cases that will prove interesting to examine: the binary droplet solution should approach that of the pure droplet as α, $\beta \to 0$; as $\alpha \to 1$

the component denoted by χ approaches involatility; and two different components that evaporate at the same rate require a non-constant initial condition to display Marangoni effects.

$\alpha,\, \beta \to 0$

In the limit of vanishing α and β the solution given by NDSolve is, as expected, identical to the solution for the pure droplet (apart from small differences caused by slight simulation discrepancies). This is illustrated in figure 4.2: for $\mathcal{C} = 2$ the binary droplet shape (4.2a) is the same as the pure droplet shape (4.2c), and its composition distribution (4.2b) remains at $\chi(r) = 0.4$ for the duration of the evaporation. We see equivalent matching across all other values of $\mathcal{C}$.

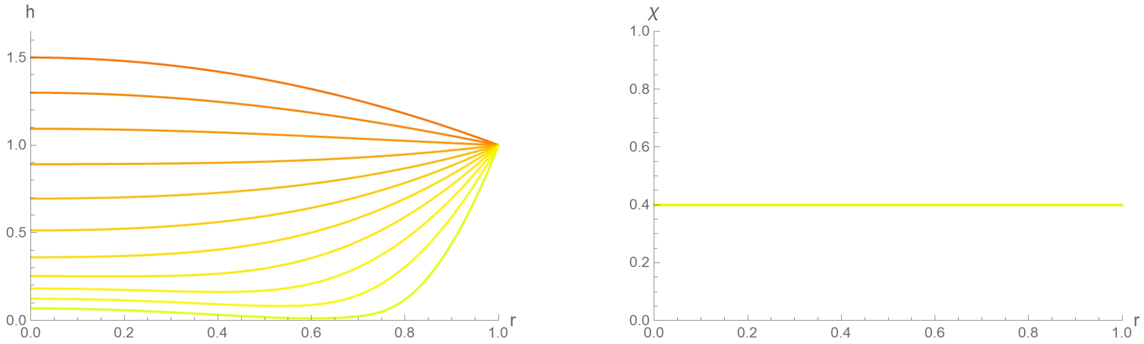

(a) Binary droplet height (b) Binary droplet composition

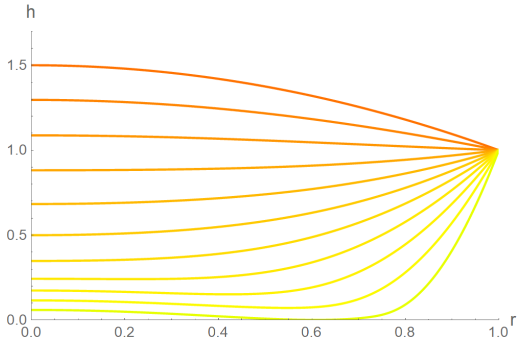

(c) Pure droplet height

Figure 4.2: A comparison between a binary droplet simulation with $\alpha = \beta = 0$ and a pure droplet, both with $\mathcal{C} = 2$. Time advances as orange turns to yellow/green.

$\alpha \to 1$

The limit $\alpha \to 1$ means that component χ does not evaporate. This corresponds to a droplet in which one component is involatile, such as an alcohol-polymer solution.[4] We solve the equation across orders of magnitude of $\mathcal{C}$ with $\alpha = 1$ and $\beta = -0.04$ (supplying medium level Marangoni effects). An example of this kind of solution is given in figure 4.3, where $\mathcal{C} = 2$; figure 4.3a depicts the droplet height evolution from initialisation, through complete evaporation of component ξ, until the (now

---

[4] Although we should recognise that the addition of most polymers would drastically change the viscosity, likely even rendering it a function of χ; for the moment we are rather inspecting a toy model that may give approximate understanding of certain volatile-involatile mixtures.

pure) droplet relaxes into its final shape, given by the black line. There are clearly some new features, most prominently a bulge at the outer edge; we will investigate the shape of the evaporating droplet in more detail in section 4.7.2.
In this limit we let the droplet evaporate until it becomes 100% component χ; as we should expect, the rate of evaporation slows as component ξ evaporates. There are now two stages to this process – the evaporation stage and the relaxation stage, in which the involatile liquid gradually takes its lowest energy shape.

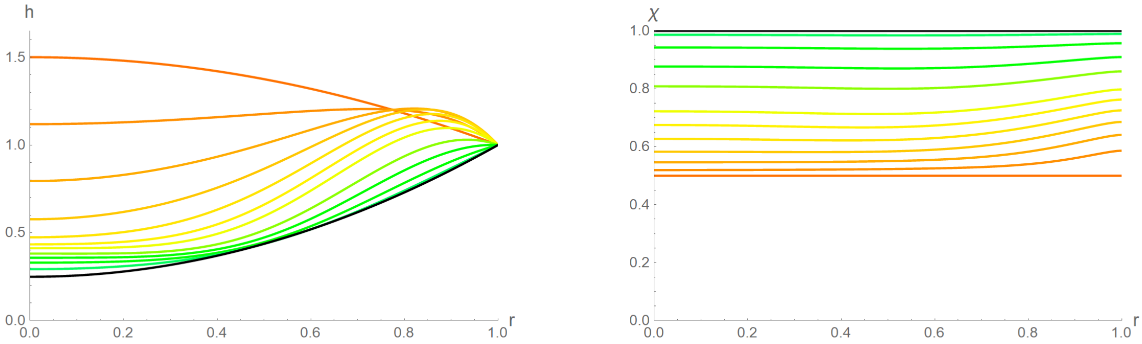

(a) Height

(b) Composition

Figure 4.3: Height and composition evolution for droplets with $\mathcal{C} = 2$ and one involatile component. Here $\chi_0 = 0.5$. Time advances as orange turns to green, with colours matching across the two figures.

We see that the final shape of the droplet is a quadratic bowl, which should come as no surprise to us: the droplet is no longer evaporating and has no surface tension gradients, so its shape is dominated by uniform surface tension. We can formalise this situation by taking the limit $\mathcal{C} \to \infty$ and writing h as a series expansion in powers of $\frac{1}{\mathcal{C}}$:

$$h = \tilde{h}_0 + \frac{1}{\mathcal{C}} h_1 + \frac{1}{\mathcal{C}^2} h_2 + \dots . \tag{4.65}$$

At leading order, equation 4.29 becomes simply

$$\frac{\partial}{\partial r}\left[r \tilde{h}_0^3 \frac{\partial}{\partial r}\left[\frac{1}{r}\frac{\partial}{\partial r}\left[r \frac{\partial \hat{h}_0}{\partial r}\right]\right]\right] = 0 \tag{4.66}$$

with boundary conditions

$$\tilde{h}_0 = 1 \quad \text{at} \quad r = 1 \tag{4.67}$$

and

$$\frac{\partial \tilde{h}_0}{\partial r} = 0 \quad \text{at} \quad r = 0. \tag{4.68}$$

One solution can be found by setting the curvature-like term to zero,

$$\frac{\partial}{\partial r}\left[\frac{1}{r}\frac{\partial}{\partial r}\left[r \frac{\partial \tilde{h}_0}{\partial r}\right]\right] = 0\,, \tag{4.69}$$

and we arrive at the quadratic we observe,

$$\tilde{h}_0 = k_{\chi 0} + (1 - k_{\chi 0}) r^2\,, \tag{4.70}$$

where, by conservation of volume, $k_{\chi_0} = \frac{2\chi_0 V_0}{\pi} - 1$ and V_0 is the initial volume of the droplet. This quantity provokes a question – what happens when the initial volume of χ is such that k_{χ_0} falls below zero? We cannot physically have a droplet surface that crosses the z-axis below zero, so what happens instead? The critical initial volume fraction, at which $k_{\chi_0} = 0$, is given by $\chi_0^* = \frac{1}{1+a}$, where we recall a to be the constant used to define the initial height profile. We usually take $a = 1.5$, in which case $\chi_0^* = 0.4$. Figure 4.4a is a depiction of a droplet with critical initial composition of the involatile component and figure 4.4b starts with involatile composition below the critical value.

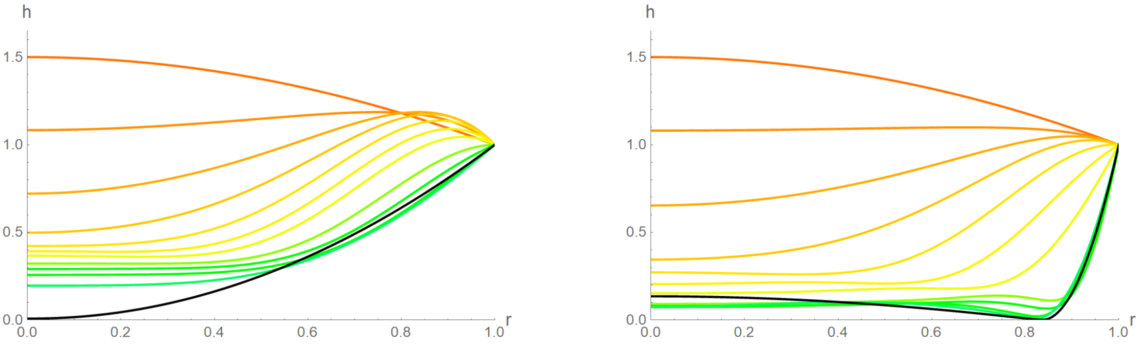

(a) $\chi_0 = 0.4$ (b) $\chi_0 = 0.1$

Figure 4.4: Height evolution for droplets with $\mathcal{C} = 2$ and one involatile component. Here we compare the evaporation of a droplet of initial volume fraction at critical value with a droplet of initial volume fraction below critical value. Time advances as orange turns to green, with colours matching across the two figures.

The corresponding composition evolution plots are shown in figure 4.5; the main feature of interest is the dip in χ near the droplet edge. We will see later that touchdown points are often associated with peaks in χ because of flow bottlenecks, but here we observe the inverse of this: the droplet being deep near the edge leads to a relative depletion of χ compared to the rest of the droplet. That is, the enhanced evaporation at the edge (which usually results in larger χ, ubiquitous in figure 4.5a) has been overcome by the droplet depth, thereby leading to a reversal of Marangoni forces in this instance. It is likely that this effect influences the droplet shape at the end of the evaporation stage – it has a dip (green curves in figure 4.4b) at $r \approx 0.8$ where liquid has been dragged from the edge slightly towards the centre (again, more on the physics of Marangoni DiWs in section 4.7.2).

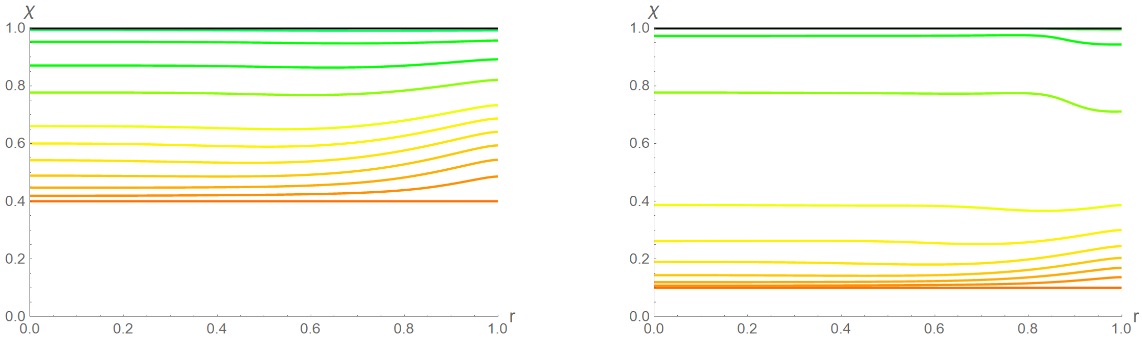

(a) $\chi_0 = 0.4$

(b) $\chi_0 = 0.1$

Figure 4.5: Composition evolution for droplets with $\mathcal{C} = 2$ and one involatile component. In figure 4.5b, the dip at the edge towards the end of the drying is caused by the interface dimple and the depth of the shoulder at the edge. Time advances as orange turns to green, with colours matching across the two figures.

While the final shape in figure 4.4a is evidently also a quadratic bowl, the droplet in figure 4.4b relaxes to a W-shape – it clearly does not have enough liquid left to form a complete bowl shape and, although the final shape of the droplet in the evaporation stage is relatively flat, the final shape in the relaxation stage is certainly not. We can show that this shape is split into two parts, separated by the touchdown point $r_{\text{td}} = 0.8225$: the inner part is quadratic again, only with a negative coefficient of r^2, turning the bowl into a lid; the outer part is a quadratic with a log term and has been described by d'Ambrosio et al. [3] in their analysis of simulated droplets evaporating from wells of different shapes. They calculate it to be

$$h(r) = 1 - \frac{1 - r^2 + 2r_{\text{td}}^2 \ln(r)}{1 - r_{\text{td}}^2 + 2r_{\text{td}}^2 \ln(r_{\text{td}})}\,; \tag{4.71}$$

in their work it represents the shape of the evaporating outer film after touchdown. Both of these shapes are shown to match the final relaxed droplet in figure 4.6.

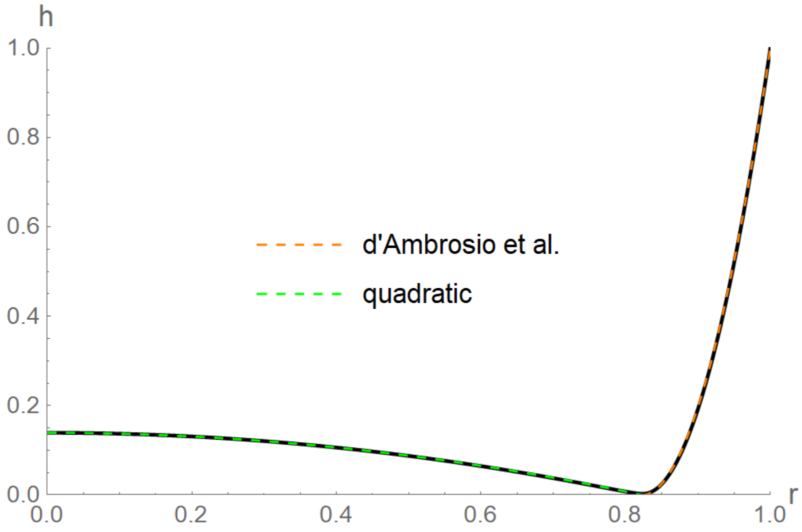

Figure 4.6: The final relaxed state of the $\chi_0 = 0.1$ droplet and two model curves superimposed. The green dotted line is a quadratic lid shape, while the orange dotted line is the quadratic/log relationship proposed in work by d'Ambrosio *et al.* [3].

Figure 4.7 displays the volume depletion and rate of volume loss of the partially involatile droplet as it evaporates. Figure 4.7b makes it clear that the rate of change of the droplet's volume is not necessarily constant, even early in the evaporation stage. Specifically, the droplets with small involatile component ($\chi_0 = 0.1, 0.2, 0.3$) pass through two regimes – their evaporation rate slows gradually at the start, then quickly comes to a complete halt. Those with initial composition above 0.4, on the other hand, gradually and consistently slow down.

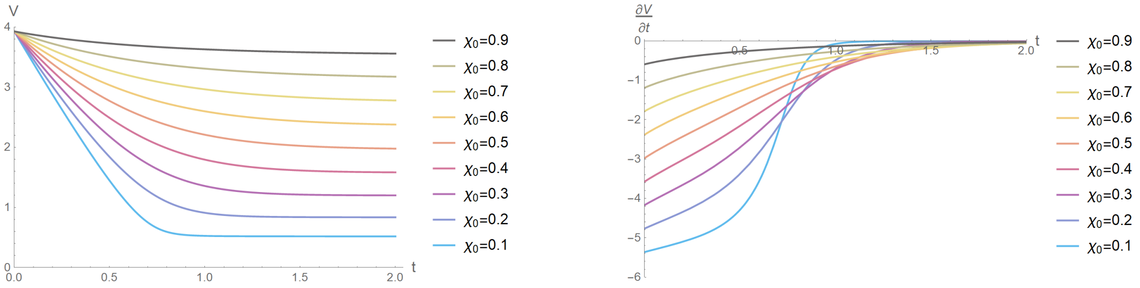

(a) Volume depletion

(b) Rate of depletion of volume

Figure 4.7: Volume evolution for a range of initial compositions, with one involatile component. The colours correspond to the constant initial condition on χ according to the legends.

We will return to partially involatile droplets in section 4.7.4, when we shall consider the effect of evolving viscosity.

$\alpha \to 0$ and $\chi_0 = \chi_0(r)$

This limit corresponds to the case of two liquids with the same rate of evaporation but different surface tensions. The only way to induce Marangoni effects here is to impose a non-constant initial concentration profile, that is $\chi(t=0)=\chi_0(r)$. We therefore initialise the composition by

$$\chi(r,t=0)=a_\chi r^3+b_\chi r^2+c_\chi \tag{4.72}$$

where $b=-\frac{3}{2}a$ in order to preserve the boundary conditions equations 4.41 and 4.43 and we have $a_\chi=-0.1$ and $c_\chi=0.4$. This simulation is somewhat contrived, as it would be rare to encounter such a system in an experiment or industrial process. However, here it may reveal some important features. Figures 4.8 and 4.9 show results for $\mathcal{C}=0.02$ and $\mathcal{C}=0.2$ respectively, both with $\beta=-0.04$.

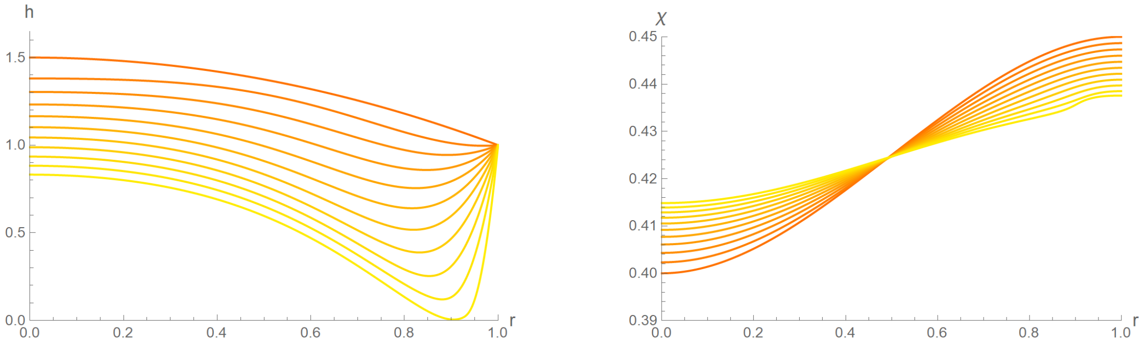

(a) Height (b) Composition

Figure 4.8: Height and composition evolution for droplets with $\mathcal{C}=0.02$ and components with equal evaporation. Time advances as orange turns to yellow, with colours matching across the two figures.

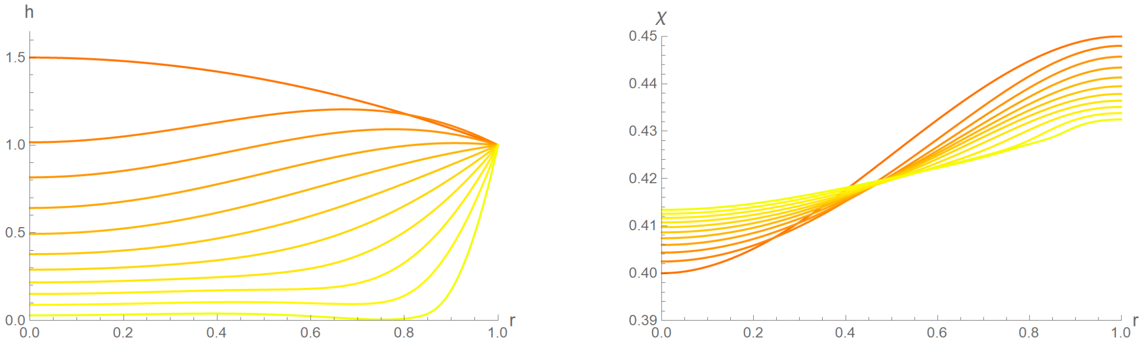

(a) Height (b) Composition

Figure 4.9: Height and composition evolution for droplets with $\mathcal{C}=0.2$ and components with equal evaporation. Time advances as orange turns to yellow, with colours matching across the two figures.

Although there is clearly no change in the ratio of χ to ξ over the whole droplet, the diffusion term we included provides a smoothing-out effect that opposes composition gradients. This means that the composition tends towards uniformity. We can show this smoothing effect is a result of diffusion by comparing these composition figures at Pe$=10$ with Pe$=20$, figures 4.10 and 4.11.

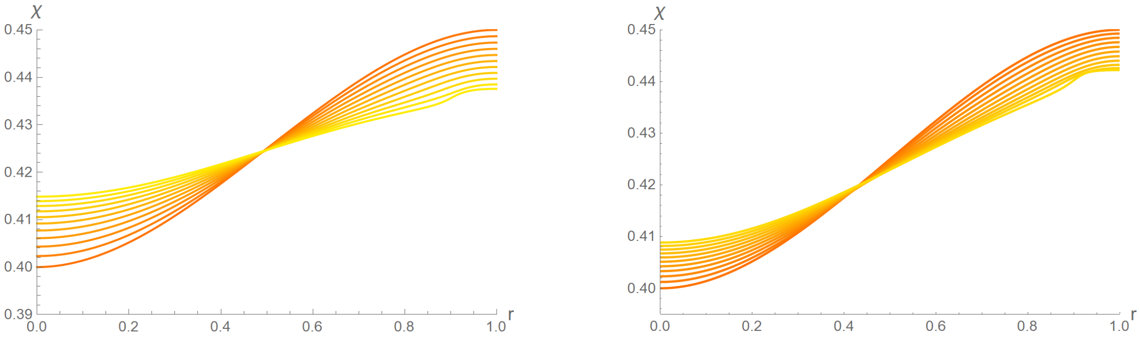

(a) Pe = 10 (b) Pe = 20

Figure 4.10: Comparing Péclet numbers for $\mathcal{C} = 0.02$; we see that the imposed composition perturbation smooths out more slowly when Pe is larger.

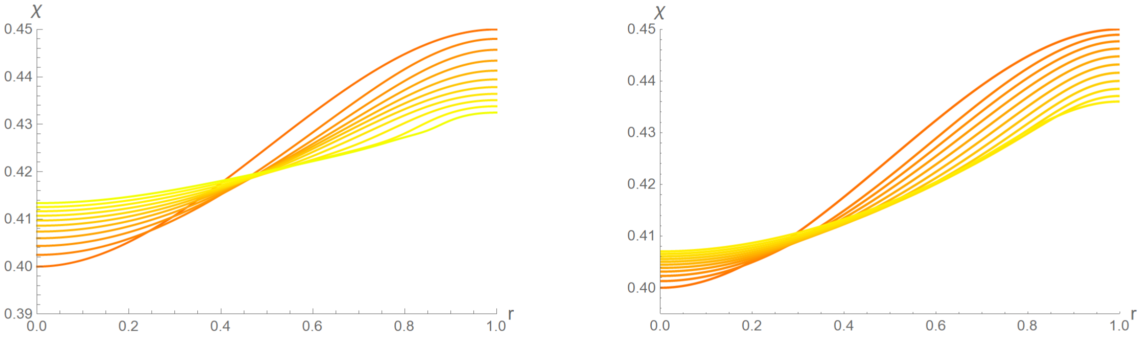

(a) Pe = 10 (b) Pe = 20

Figure 4.11: Comparing Péclet numbers for $\mathcal{C} = 0.2$; we see that the imposed composition perturbation smooths out more slowly when Pe is larger.

In both cases, doubling the Péclet number decreased the smoothing effect, showing that diffusion plays a role in opposing composition gradients.
We include such a diffusion term in the model primarily as a numerical stabiliser, rather than to accurately model the diffusion dynamics of the system. For example, the composition evolution equation at $r = 1$ is purely diffusive, meaning very sharp χ gradients would emerge without diffusion.

4.7.2 Comparison to Pure Droplets

It will prove useful to take a cursory glance at the broad effects that the Marangoni effect has on droplet shape. To this end, we can compare two solutions at a time, droplets with Marangoni turned off and with Marangoni turned on, while moving through orders of magnitude in $\mathcal{C}$ and noting the general trends and relationships between pure[5] droplets and binary droplets. We choose $\alpha = 0.6$ and $\beta = -0.08$ in order to obtain a large effect (ideally visible in the eyeball norm). We start with $\mathcal{C} = 0.02$ in figure 4.12; time points for each droplet are taken at $\frac{1}{10}$ intervals of the interval $[0, t_{\text{td}}]$, where t_{td} is the touchdown time of the droplet in question.

---

[5] These droplets are not strictly pure, because we have matched α to the binary droplet in order to give both as similar an evaporation rate as possible over the course of the drying. We are interested here in the effect of surface tension gradients (β) alone.

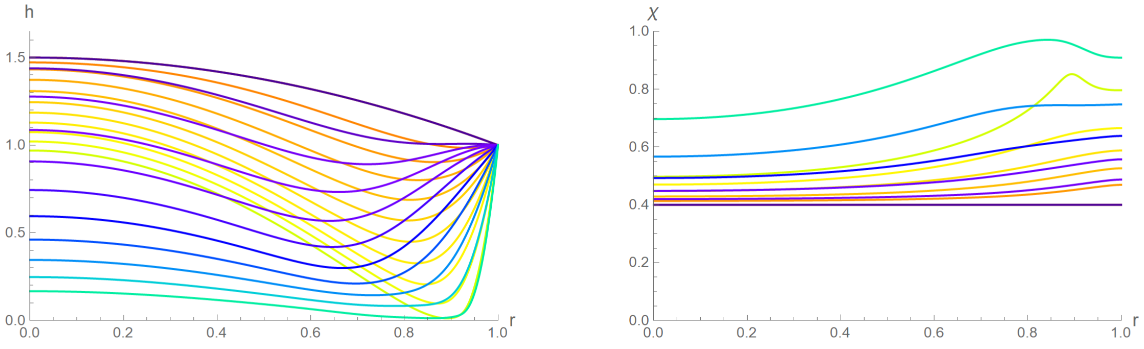

(a) Height comparison

(b) Composition comparison

Figure 4.12: A comparison between a droplet with $\beta = 0$ (orange–yellow) and one with $\beta = -0.08$ (blue–green). $\mathcal{C} = 0.02$ and the touchdown times are $t_{\text{td}} = 0.67$ (pure) and $t_{\text{td}} = 0.93$ (binary).

The first effect we notice is that the lens/dimple of the pure droplet is dramatically reduced when negative-β Marangoni effects are present. A second new feature is an inversion of surface curvature near the edge of the well – this appears almost immediately and persists until $t \approx 0.8t_{\text{td}}$. We can think of this inversion of curvature as a buildup of material induced by Marangoni flows. Large, negative β means that the component that evaporates slower (χ) has a larger surface tension; the preferential evaporation near the contact line leads to an enrichment of χ at the edge of the droplet (see figure 4.12b), which proceeds to draw liquid from the centre by surface tension forces.

In the composition comparison, figure 4.12b, it appears that the inclusion of surface tension gradients smooths the distribution of the two components. This phenomenon is clearer if we consider the quantity $h\chi$, which is proportional to the absolute volume of component χ across the droplet, figure 4.13. This figure demonstrates the composition redistribution property better because it eliminates the spike at the touchdown point in figure figure 4.12b.

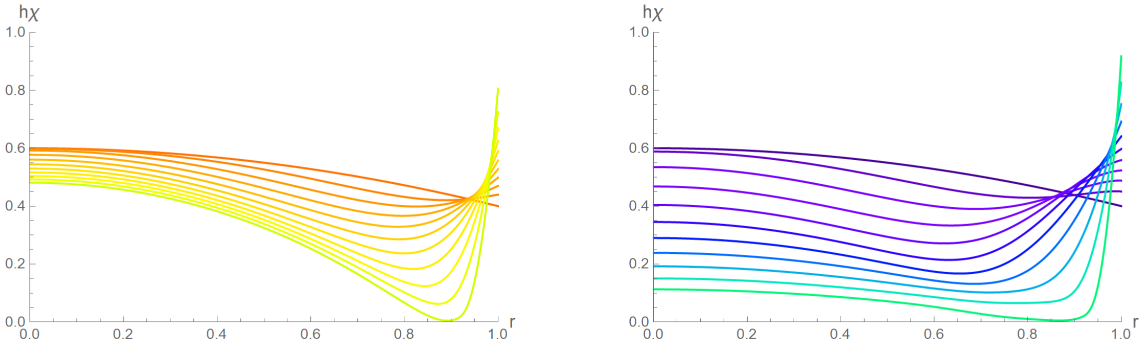

(a) No Marangoni. Time evolves from orange to green.

(b) Marangoni present. Time evolves from purple to teal.

Figure 4.13: The amount of component χ in a droplet with no Marangoni effect compared with one in which Marangoni is present. $\mathcal{C} = 0.02$.

Equivalent height and composition comparisons for $\mathcal{C} = 0.2$ can be found in figure 4.14. Once again, the dimple characteristic of a W-shape profile is reduced; in fact in this case the W-shape is entirely eliminated towards the end of the drying and we are left with a completely flat droplet.

We can see the same edge curvature inversion as in the previous example; here it actually leads to a slight mound above the rim at the beginning of the drying process.

An interesting phenomenon emerges in the composition evolution too. The penultimate curve shown with Marangoni forces activated (bright green) has a negative gradient (from $r = 0$ to $r \approx 0.9$), in contrast to the (mostly) positive gradients we have seen up to this point. This indicates that Marangoni stress is here directed towards the centre of the droplet, rather than towards the edge, and may explain the fast disappearance of the surface curvature inversion (figure 4.14a) as the droplet dries. The gradient of χ remains positive at the edge, likely held there by the larger enhanced evaporation of component ξ.

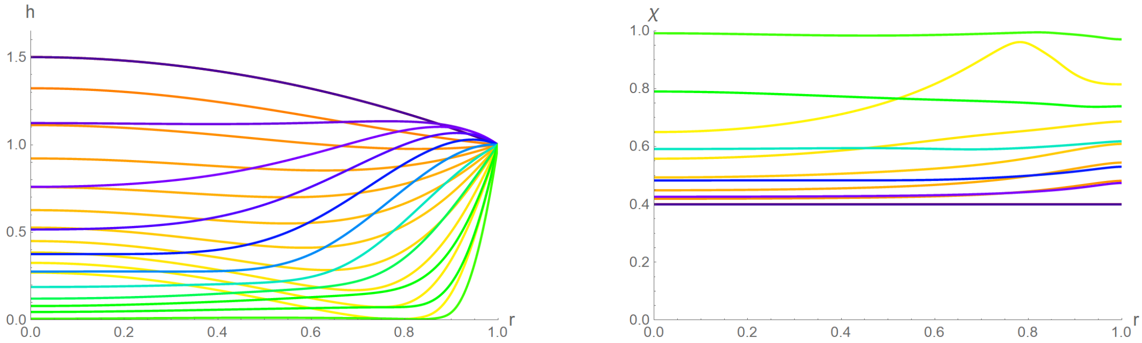

(a) Height comparison (b) Composition comparison

Figure 4.14: A comparison between a droplet with $\beta = 0$ (orange–yellow) and one with $\beta = -0.08$ (blue–green). $\mathcal{C} = 0.2$ and the touchdown times are $t_{\mathrm{td}} = 0.86$ (pure) and $t_{\mathrm{td}} = 0.97$ (binary).

We contrast the above examples to a binary droplet in which the less volatile component has the lower surface tension; this scenario corresponds to $\beta > 0$. In this case we expect some opposite effects, namely that the droplet will tend to grow in the centre due to the enrichment of the component with lower surface tension at the edge, resulting in a Marangoni flow from the edge towards the centre. We do indeed find that the droplet's W-shape is enhanced; this simulation, with $\mathcal{C} = 0.2$, $\alpha = 0.2$, and $\beta = 0.03$, is presented in figure 4.15.

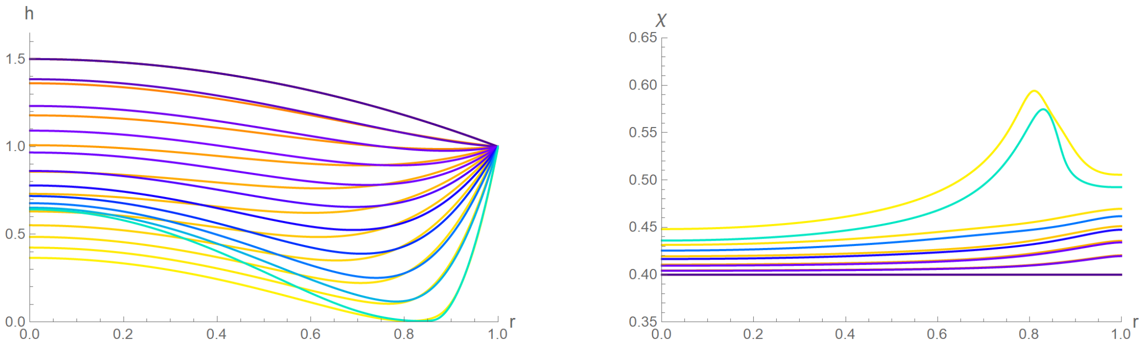

(a) Height comparison

(b) Composition comparison, note that the vertical axis is zoomed in.

Figure 4.15: A comparison between a droplet with $\beta = 0$ (orange–yellow) and one with $\beta = 0.03$ (blue–green). $\mathcal{C} = 0.2$ and the touchdown times are $t_{\mathrm{td}} = 0.61$ (pure) and $t_{\mathrm{td}} = 0.56$ (binary).

The composition also does not exhibit the smoothing effect seen in figures above; rather, it retains a sharp point at the touchdown location. This sharp point is a consequence of the flow behaviour at touchdown and the comparative flux – component χ builds up in this region because it is evaporating more slowly than component ξ and its flow is inhibited through the ever narrowing bottleneck. While it seems that negative β permits redistribution of components just before touchdown (probably by flattening out the interface near to r_{td}, see figures 4.12a and 4.14a), positive β does not.

This is a good moment to briefly return to diffusion and the Péclet number; it is important to see what effect diffusion has on a full droplet simulation. In figure 4.16, we compare Pe$= 10$ with Pe$= 40$, both otherwise having the same parameters as in figure 4.15. Despite imposing such a large change in Pe, there is little difference between the final results: the important quantities such as touchdown point and time barely change. We can see that there is increased build-up of χ near the edge when Pe is larger (due to higher volatility of component ξ); this is to be expected because diffusion is reduced, slightly limiting its capacity to flow inwards.

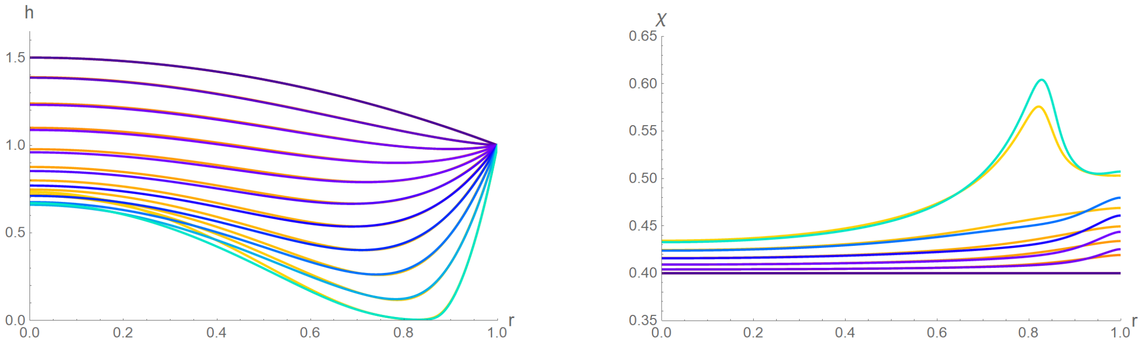

(a) Height comparison

(b) Composition comparison, note that the vertical axis is zoomed in.

Figure 4.16: A comparison between Pe $= 10$ (orange–yellow) and Pe $= 40$ (blue–green). $\mathcal{C} = 0.2$, $\alpha = 0.2$, $\beta = 0.03$. The touchdown times are $t_{\mathrm{td}} = 0.56$ and $t_{\mathrm{td}} = 0.57$ respectively.

4.7.3 Velocity Field

The majority of experimental observations of the Marangoni effect and CRE suppression in droplets (usually large and sessile) are explained in the literature with a 'recirculation flow' argument; many experimental researchers suggest that the liquid cycles round the droplet during the drying, allowing deposited material to settle across the substrate rather than be concentrated at the edge [7, 69, 125, 126].

The following figures (4.17-4.23) are vector plots of the liquid velocity field for a range of binary droplets, analogous to those for pure droplets in section 3.8.5. As previously, the vectors are coloured according to the radial component of velocity and the colour scale is unique to each plot, in order to optimise the presentation of the data. Refer to the bar legend on the right for absolute (dimensionless) speeds. Also as previously, we have not imposed a zero velocity boundary condition at the wall, rather a zero average velocity condition, meaning some of the arrows are permitted to point across the vertical line $r = 1$. In this way, they lose some aspect of quantitative reliability, as this is not a physical boundary condition. However, the height average boundary condition corresponds to neglecting the term in ε^2 in the Navier-Stokes equations, and so we can argue that the error extends only a distance of ε into the liquid from the wall.

New to these plots is the presence of inward flows. We denote a region of inward flow by light red shading (in addition to the obvious flipped direction of the arrows). These regions do not necessarily constitute full recirculating flows; they are rather regions where the liquid flows towards the centre. It is not clear whether thin DiWs support the full recirculating flows observed in the works cited above; Hu and Larson report, for example, that full recirculating flows are suppressed at small contact angles [68] in their sessile droplets.

The equation for vertical velocity is now

$$\begin{aligned} w(r,z) = \frac{\mathcal{C}}{2}\Big(\Big(\frac{\partial^4 h}{\partial r^4} + \frac{2}{r}\frac{\partial^3 h}{\partial r^3} - \frac{1}{r^2}\frac{\partial^2 h}{\partial r^2} + \frac{1}{r^3}\frac{\partial h}{\partial r}\Big)\Big(\frac{1}{3}z^3 - z^2 h\Big) \\ - z^2\frac{\partial h}{\partial r}\Big(\frac{\partial^3 h}{\partial r^3} + \frac{1}{r}\frac{\partial^2 h}{\partial r^2} - \frac{1}{r^2}\frac{\partial h}{\partial r}\Big)\Big) - z^2\frac{\mathcal{M}}{2}\Big(\frac{\partial^2 \chi}{\partial r^2} + \frac{1}{r}\frac{\partial \chi}{\partial r}\Big). \quad (4.73) \end{aligned}$$

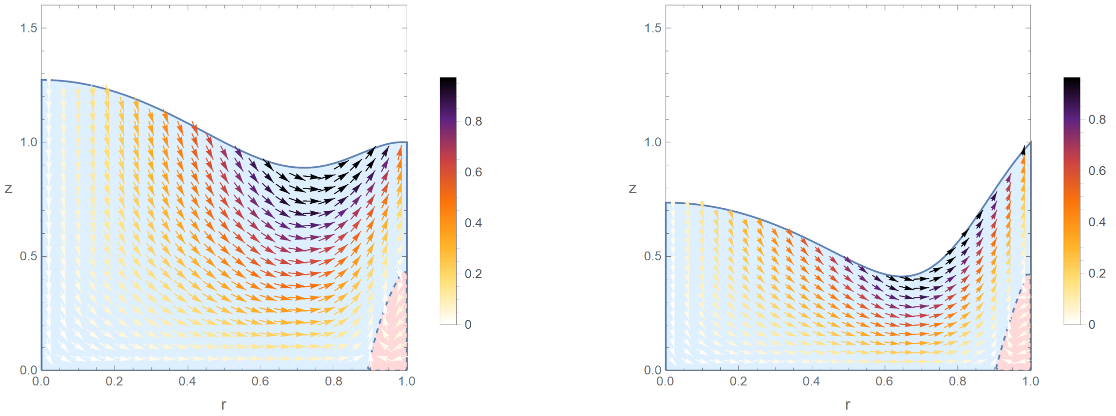

(a) $t = 0.2t_{\text{td}}$ (b) $t = 0.5t_{\text{td}}$

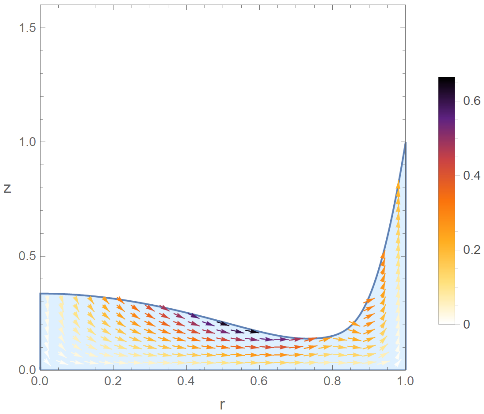

(c) $t = 0.8t_{\text{td}}$

Figure 4.17: A vector plot of the flow field in a binary droplet with $\mathcal{C} = 0.02$, $\alpha = 0.6$, and $\beta = -0.08$. An effect of Marangoni forces is to redistribute flow across the whole droplet; compare to figure 3.25, whose flow at late times is limited to the region around the dimple.

The flow field for the smallest value of $\mathcal{C}$ is presented in figure 4.17. It shows a small region of inward flow near the beginning of the drying, which shrinks and vanishes before $t = 0.8t_{\text{td}}$. These plots also nicely emphasise the effect of negative β in raising the surface tension at the edge and drawing liquid in to create a mound near the pin: we see the strongest upward flow near the top right of the droplet in figures 4.17a and 4.17b. The early inward flow is a consequence of this mound, through the Laplace pressure gradient that arises from the negative curvature near the wall.

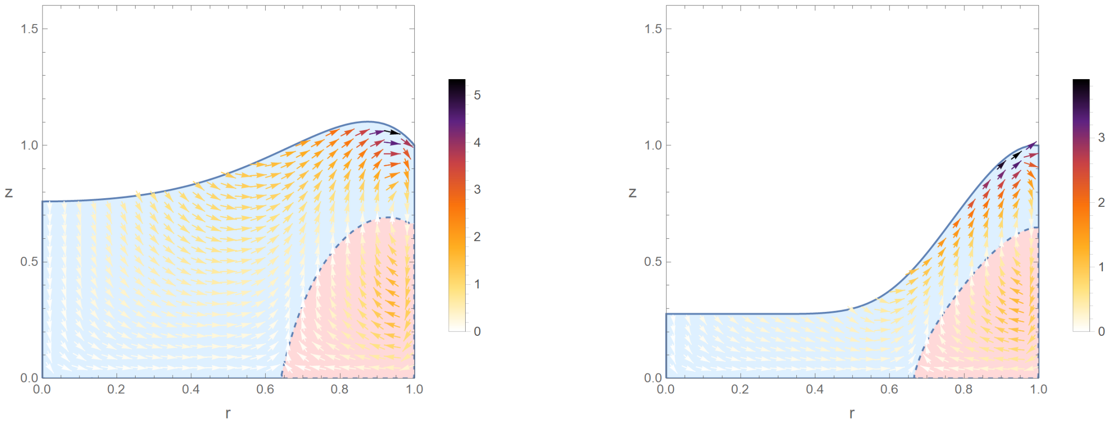

(a) $t = 0.2t_{\mathrm{td}}$

(b) $t = 0.5t_{\mathrm{td}}$

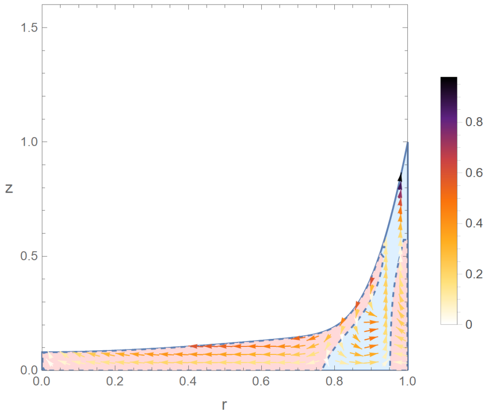

(c) $t = 0.8t_{\mathrm{td}}$

Figure 4.18: A vector plot of the flow field in a binary droplet with $\mathcal{C} = 0.2$, $\alpha = 0.6$, and $\beta = -0.08$. Here we see the first large regions of inward flow; although they do not span the whole radius of the droplet it is clear that the Marangoni effect also acts to drive flow inwards throughout the drying.

Going up an order of magnitude to $\mathcal{C} = 0.2$, we immediately notice that the region of recirculation flow is larger, extending inwards along the bottom nearly to $r = 0.6$. The mound effect is also visible, with large flow moving upwards and outwards in figures 4.18a and 4.18b.

The most notable feature about the late stages of the drying in this case is that the inward current dominates, reversing the direction of flow in the inner part of the droplet. Interestingly, this feature disappears after increasing $\mathcal{C}$ by another order of magnitude, figure 4.20c. The reason for this can be found in figure 4.19; there are slightly more pronounced negative gradients in χ in figure 4.19a than in figure 4.19b near the end of the evaporation, meaning the Marangoni effect will be stronger and will encourage inward flows. The inward flow becomes suppressed near the edge of the droplet where the flow due to interface curvature is large and outward.

We have already seen this phenomenon in the spikes of χ observed at the touchdown point (e.g. figure 4.15b) – when the droplet becomes very thin the less volatile component builds up. In the specific case of late-time $\mathcal{C} = 0.2$, the droplet happens to be thinnest near the centre and gradually thickens, which results in the large region of inward Marangoni flow.

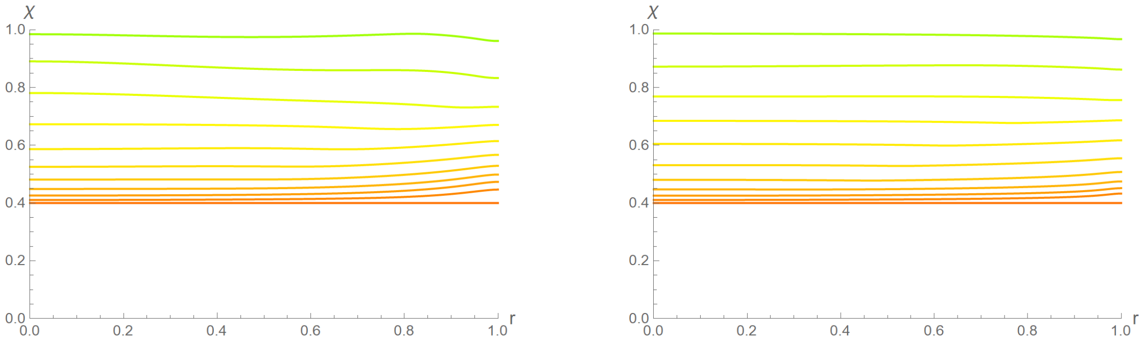

(a) $\mathcal{C} = 0.2$ (b) $\mathcal{C} = 2$

Figure 4.19: Comparing the composition evolution across an order of magnitude in $\mathcal{C}$. $\alpha = 0.6$ and $\beta = -0.08$. For smaller $\mathcal{C}$, composition gradients are more pronounced and Marangoni forces are stronger, leading to inward flows dominating towards the later stages of drying.

The red region in figure 4.20c is found closer to the edge and does not extend back to the centre of the droplet; it actually has positive χ gradients near the centre, but its smaller curvature near the edge combines with negative χ gradients to produce an external inward flow. Note that the droplet interface is much flatter than the $\mathcal{C} = 0.2$ – although it is also thin, its height is largely constant until $r \approx 0.7$, where a negative gradient in χ appears and we observe an inward Marangoni flow.

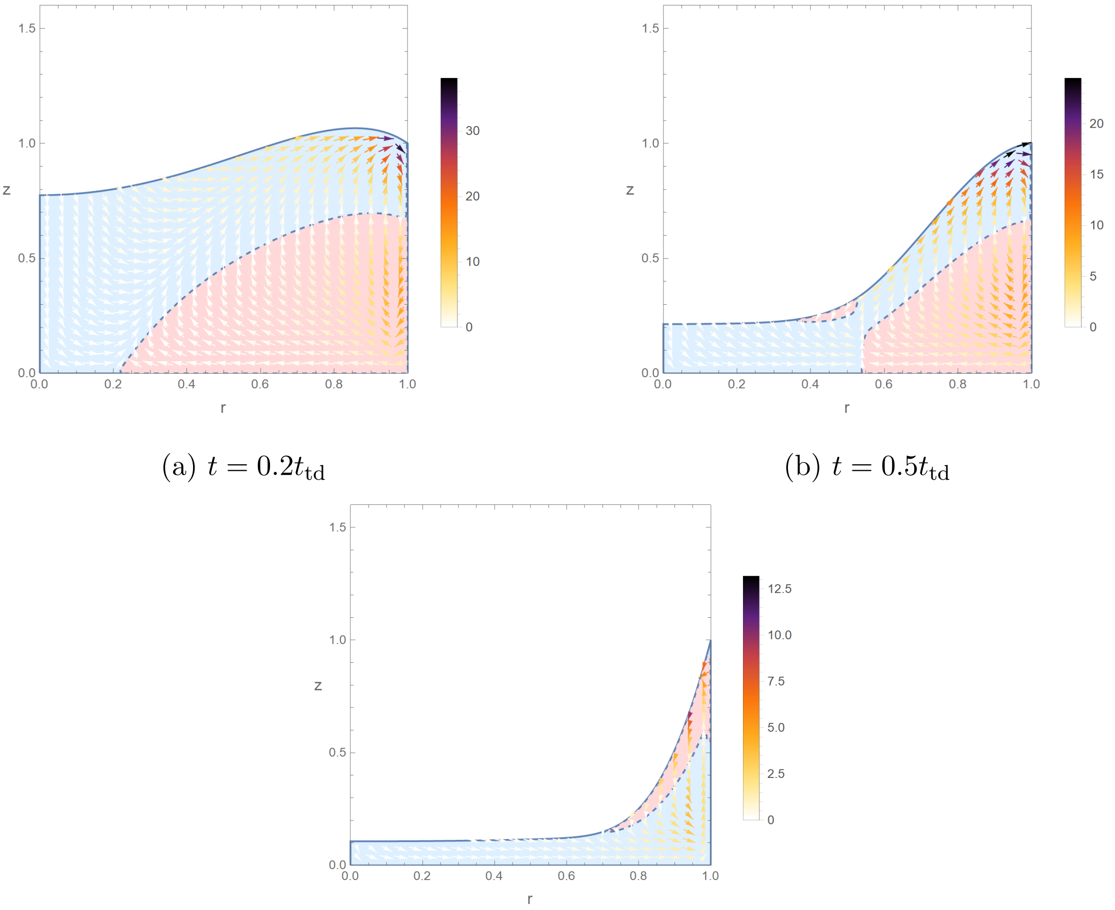

(a) $t = 0.2t_{\text{td}}$

(b) $t = 0.5t_{\text{td}}$

(c) $t = 0.8t_{\text{td}}$

Figure 4.20: A vector plot of the flow field in a binary droplet with $\mathcal{C} = 2$, $\alpha = 0.6$, and $\beta = -0.08$. One of the most notable features of this figure is the dramatic decrease in flow speed near the edge as the droplet dries. This is evidence that the rush hour phenomenon is suppressed somewhat (compare to figure 3.27).

We show the individual flow contributions from capillary and Marangoni forces for figure 4.20a in figure 4.21, which highlights that inward flows can be driven by capillary forces as well as by Marangoni effects (e.g. figure 4.18c). We have also provided a cartoon to show the general flow pattern more clearly, figure 4.22.

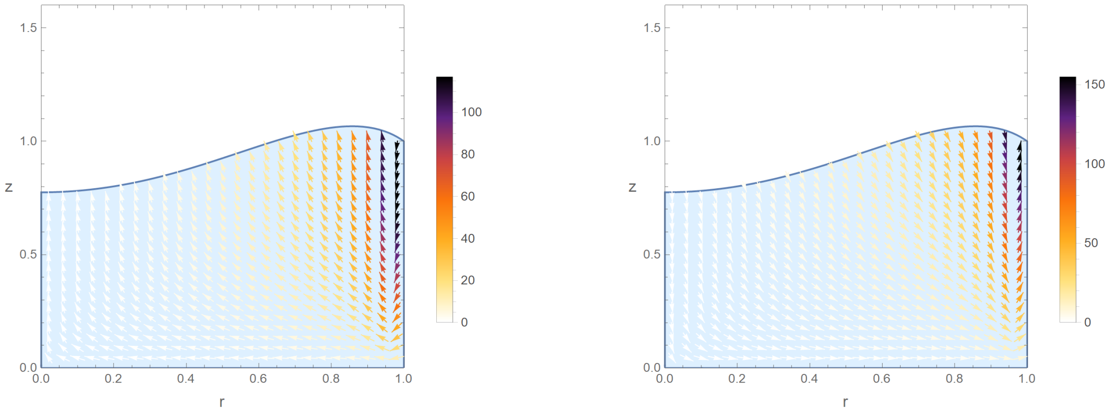

(a) Capillary (b) Marangoni

Figure 4.21: Figure 4.20a is a combination of inward capillary flows and outward Marangoni flows.

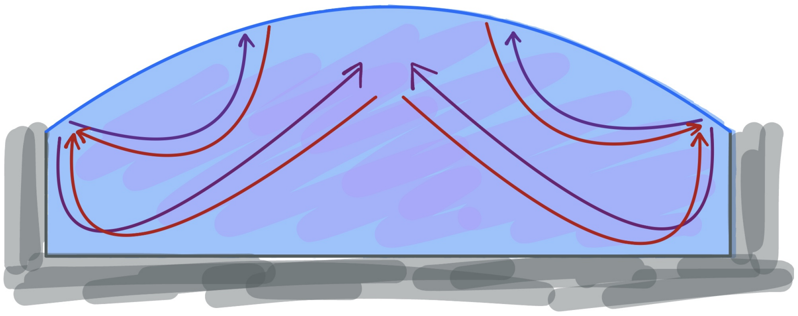

Figure 4.22: A cartoon illustrating the flow field of the droplet in figure 4.21. Purple curves are capillary flows, red curves are Marangoni flows.

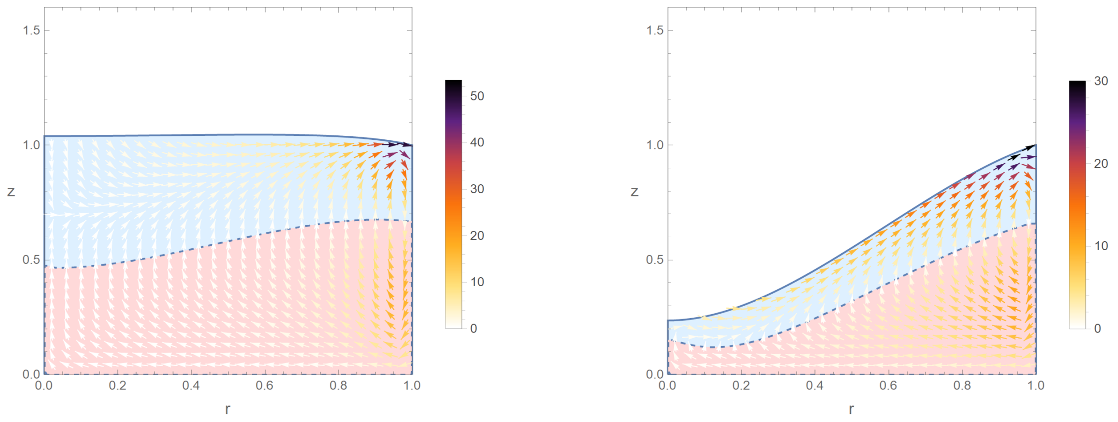

(a) $t = 0.2t_{\text{td}}$

(b) $t = 0.5t_{\text{td}}$

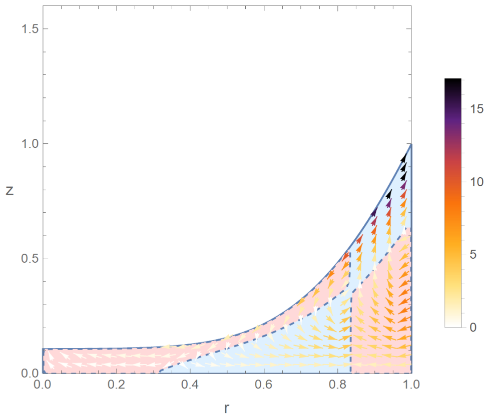

(c) $t = 0.8t_{\text{td}}$

Figure 4.23: A vector plot of the flow field in a binary droplet with $\mathcal{C} = 16$, $\alpha = 0.2$, and $\beta = -0.04$. We have chosen smaller values of α and β because, as $\mathcal{M}$ is much higher, we do not need as large evaporation and surface-tension differences in order to see the results. Here we see the first evidence of full recirculating flows at early/medium times.

The simulation with $\mathcal{C} = 16$ exhibits a full recirculation current, figure 4.23. Its flows are also much faster than both pure droplets (in this case about ten times faster than the equivalent pure droplet) and binary droplets with smaller values of $\mathcal{C}$. This effect is due to the Marangoni flows encountering less viscous resistance; we recall that $\mathcal{C} \sim \mu^{-1}$.

Overall, for droplets with large, negative Marangoni flows present, those with higher values of $\mathcal{C}$ tend to exhibit larger regions of inward flow or even recirculation; above a certain value of $\mathcal{C}$ the recirculation reaches the entire way back along the bottom of the droplet. They also get faster with increasing $\mathcal{C}$, however all droplet flows also slow down towards the end of the evaporation, which contrasts to the acceleration (‘rush hour’) we see in pure droplets in section 3.8.5.

At no point do we simulate particles in our model, but if we were to they would have to be distributed unevenly in z for these recirculation currents to suppress the CRE. We mentioned earlier that researchers will often invoke recirculation to explain CRE suppression, but the requirement for uneven vertical distribution of particles sits somewhat uncomfortably with the lubrication approximation, which completely flattens the droplet. We must, therefore, be very careful not to try to explain away all our problems using recirculation arguments; the inward flows we observe are nonetheless interesting and can contribute to an understanding of DiW CRE suppression.

In the case of positive β, when the more volatile component also has the higher surface tension, we observe much less recirculation over the course of the drying, figure 4.24. At late times there is a region of inward flow (figure 4.24c), but it is located solely in the inner part of the droplet and serves only to enhance the W-shape characteristic of these kinds of binary combinations (see section 4.7.2) by vacating the region where the dimple emerges.

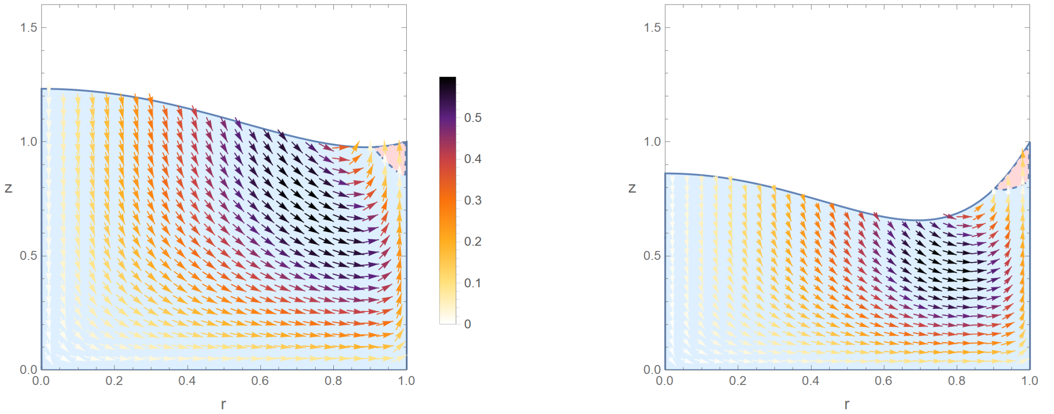

(a) $t = 0.2t_{\text{td}}$

(b) $t = 0.5t_{\text{td}}$

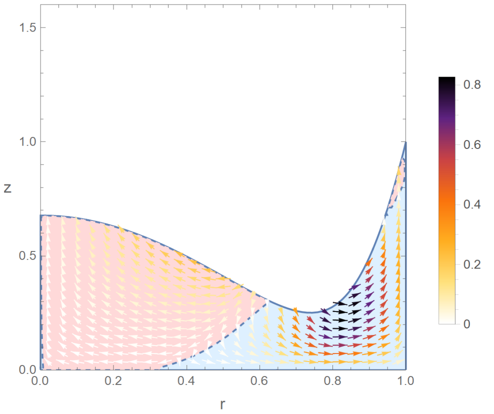

(c) $t = 0.8t_{\text{td}}$

Figure 4.24: A vector plot of the flow field in a binary droplet with $\mathcal{C} = 0.2$, $\alpha = 0.2$, and $\beta = 0.03$. The speed in this case is consistently small compared to the previous examples, but a slight rush-hour effect is detectable near the Marangoni-enhanced dimple.

The inward flow at small r is a direct result of a large, positive composition gradient, which drives material towards the region of higher surface tension (now located at the centre). Inward flows are prevented at larger r by the strong, outward capillary forces. We compare the two in figure 4.25.

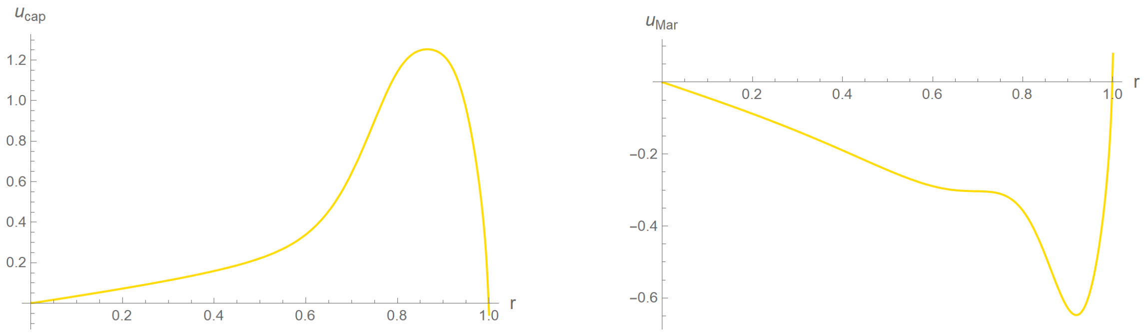

(a) Capillary-driven velocity

(b) Marangoni-driven velocity

Figure 4.25: The horizontal capillary and Marangoni velocities in figure 4.24c at $z = 0.2$.

4.7.4 Variable Viscosity

We saw in section 4.7.1 that our model can easily be adjusted for the presence of an involatile component: in the limit $\alpha \to 1$ one component does not evaporate. Although there exist some involatile liquids with viscosities comparable to laboratory alcohols and aromatics, many involatile liquids will have a significantly different viscosity to the volatile species we have been dealing with up to now. In order to properly model an alcohol-polymer solution, for example, we should adjust the model to account for changes in viscosity as the alcohol evaporates and the polymer concentrates. After the discussion in section 2.7 of chapter 2, we shall consider two simple mixture viscosity models: the linear and logarithmic combinations of viscosity respectively. Unless otherwise stated, in this section we will use $\mathcal{C} = 2$, $\alpha = 1$, $\beta = -0.04$, and $\chi_0 = 0.1$.

Linear Combination of Viscosities

The linear viscosity model for a binary droplet gives a total viscosity of

$$\mu = \chi\mu_\chi + \xi\mu_\xi \,, \tag{4.74}$$

where μ_i is the viscosity of the i^{th} component. If we use γ as a third binary parameter (after α and β) to denote the comparative magnitude of the two viscosities,

$$\mu_\chi = (1+\gamma)\mu_\xi, \tag{4.75}$$

the total viscosity can be written as

$$\mu = (1+\gamma\chi)\mu_\xi. \tag{4.76}$$

After this change, the radial velocity field becomes

$$u(r,z) = -\frac{\mathcal{C}}{1+\gamma\chi}\frac{\partial}{\partial r}\left[\frac{1}{r}\frac{\partial}{\partial r}\left[r\frac{\partial h}{\partial r}\right]\right]\left(\frac{1}{2}z^2 - zh\right) + \frac{\mathcal{M}}{1+\gamma\chi}\frac{\partial \chi}{\partial r}z\,, \tag{4.77}$$

where $\mathcal{C}$ and $\mathcal{M}$ take μ_ξ. Following the same procedure as in chapter 3 and in section 4.4 of this chapter, the height and composition lubrication equations are

$$\frac{\partial h}{\partial t} = -\frac{\mathcal{C}}{3r}\frac{\partial}{\partial r}\left[\frac{rh^3}{1+\gamma\chi}\frac{\partial}{\partial r}\left[\frac{1}{r}\frac{\partial}{\partial r}\left[r\frac{\partial h}{\partial r}\right]\right]\right] - \frac{\mathcal{M}}{2r}\frac{\partial}{\partial r}\left[\frac{rh^2}{1+\gamma\chi}\frac{\partial \chi}{\partial r}\right] - \frac{1-\alpha\chi}{\sqrt{1-r^2}} \tag{4.78}$$

and

$$\frac{\partial \chi}{\partial t} = -\frac{1}{1+\gamma\chi}\frac{\partial \chi}{\partial r}\left(\frac{\mathcal{C}h^2}{3}\frac{\partial}{\partial r}\left[\frac{1}{r}\frac{\partial}{\partial r}\left[r\frac{\partial h}{\partial r}\right]\right] + \frac{\mathcal{M}h}{2}\left(\frac{\partial \chi}{\partial r}\right)^2\right) + \frac{1}{\mathrm{Pe}}\left(\frac{1}{r}\frac{\partial}{\partial r}\left[r\frac{\partial \chi}{\partial r}\right] + \frac{1}{h}\frac{\partial h}{\partial r}\frac{\partial \chi}{\partial r}\right) + \frac{1}{h}\frac{\alpha\chi(1-\chi)}{\sqrt{1-r^2}}. \tag{4.79}$$

Figure 4.26 is an example of the evolution of a partially involatile droplet. It exhibits very similar behaviour to the droplets in section 4.7.1 – the final shape (black curves) is again a combination of a pure quadratic before the touchdown point and a quadratic-log function (see equation 4.71) after the touchdown point. However variable viscosity does induce some quantitative changes.

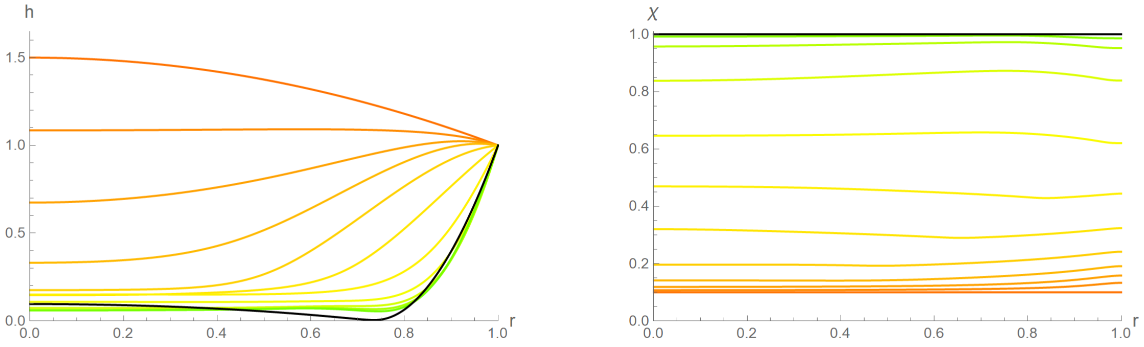

(a) Height

(b) Composition

Figure 4.26: Height and composition evolution for a droplet with viscosity as a linear function of χ. $\mathcal{C} = 2$, $\alpha = 1$, $\beta = -0.04$, $\gamma = 4$, $\chi_0 = 0.1$. One component is involatile again, and we can see a similar dimpled solution to that in figure 4.6 after the volatile component evaporates.

Higher viscosity of the involatile component appears to have an effect on the touchdown point of the final droplet shape; figure 4.27 reveals that the touchdown point moves further outward as the viscosity of the involatile component increases. These are droplets that, like in section 4.7.1, have fully evaporated and then been allowed to relax – we might expect them to all be identical eventually, because the final liquid has the same properties in each case, except for increasing viscosity. However this is clearly not what we see. It looks as if the altered shape during evaporation leads to a different pre-relaxation shape, which contains a dimple for certain values of χ_0.

This kind of solution is not completely unexpected; in fact, dimpled solutions for a thin film lubrication equation appear often in the literature. Shi et al. showed that an oscillating dimpled solution occurs in an oil film over a bubble [127]; interestingly their experiment was also heavily influenced by evaporation and Marangoni flows, which draw liquid from one region to another to create the dimple. Dimpled solutions

also appear in other works using the lubrication approximation on thin films [128, 129, 130, 131].
We have included an approximate functional form relating r_{td} and γ, displayed in figure 4.27, that indicates that the touchdown point tends to a value of 0.90 as the viscosity becomes large.

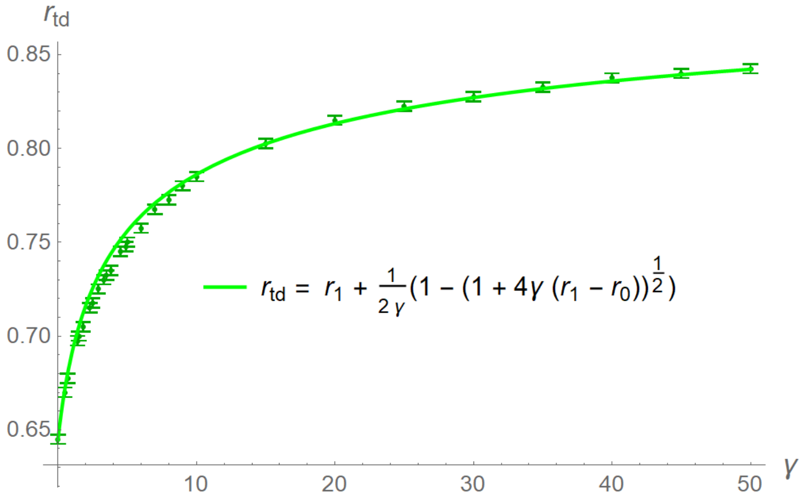

Figure 4.27: The touchdown radius as a function of the viscosity of the involatile component. We calculate that $r_0 = 0.645$ and $r_1 = 0.90$. Error bars are of size Δr.

This phenomenon becomes particularly interesting once we consider the involatile component to comprise part of the desired (or undesired) deposit material – we have shown that the final deposit is likely to consist of two regions, an inner region with the shape of a quadratic bowl, and an outer region whose shape is a quadratic with a logarithmic term in. This kind of profile has been observed experimentally in industrial tests (Dank Walker, Merck Ltd., private communication).
A linear model for viscosity can be well applied to systems in which the viscosity ratio between the two components is small, but we will need to move to a logarithmic model in order to have a chance to examine systems such as polymer solutions, in which the viscosity ratio is large.

Logarithmic Combination of Viscosities

The logarithmic model, on the other hand, gives a total viscosity of

$$\mu = e^{\chi \ln(\mu_\chi) + \xi \ln(\mu_\xi)}\,, \tag{4.80}$$

or equivalently

$$\mu = (1+\gamma)^\chi \mu_\xi\,. \tag{4.81}$$

We show this relationship and how it compares to the linear relationship in figure 4.28.

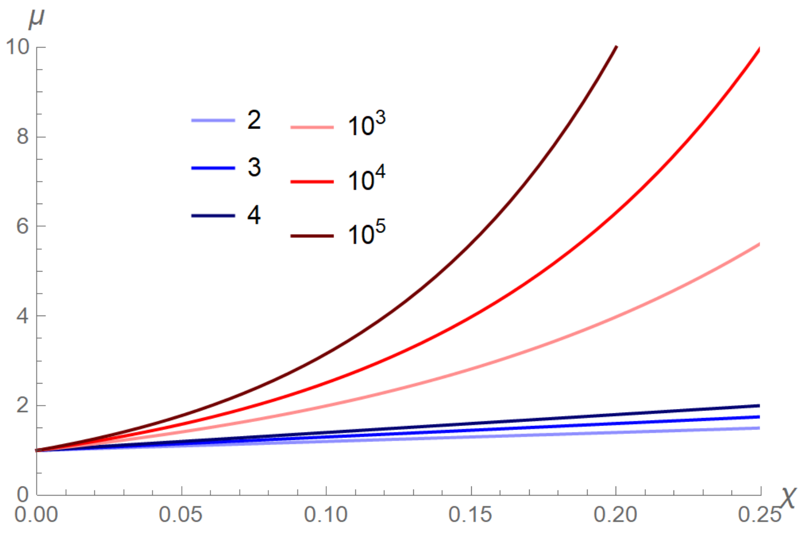

Figure 4.28: A plot of the viscosity as it varies linearly (blue) and logarithmically (red) with composition. Numbers in the legend are values of parameter γ.

This form leads to lubrication equations

$$\frac{\partial h}{\partial t} = -\frac{\mathcal{C}}{3r}\frac{\partial}{\partial r}\left[\frac{rh^3}{(1+\gamma)^\chi}\frac{\partial}{\partial r}\left[\frac{1}{r}\frac{\partial}{\partial r}\left[r\frac{\partial h}{\partial r}\right]\right]\right] - \frac{\mathcal{M}}{2r}\frac{\partial}{\partial r}\left[\frac{rh^2}{(1+\gamma)^\chi}\frac{\partial \chi}{\partial r}\right] - \frac{1-\alpha\chi}{\sqrt{1-r^2}} \quad (4.82)$$

and

$$\frac{\partial \chi}{\partial t} = -\frac{1}{(1+\gamma)^\chi}\frac{\partial \chi}{\partial r}\left(\frac{\mathcal{C}h^2}{3}\frac{\partial}{\partial r}\left[\frac{1}{r}\frac{\partial}{\partial r}\left[r\frac{\partial h}{\partial r}\right]\right] + \frac{\mathcal{M}h}{2}\left(\frac{\partial \chi}{\partial r}\right)^2\right) + \frac{1}{\mathrm{Pe}}\left(\frac{1}{r}\frac{\partial}{\partial r}\left[r\frac{\partial \chi}{\partial r}\right] + \frac{1}{h}\frac{\partial h}{\partial r}\frac{\partial \chi}{\partial r}\right) + \frac{1}{h}\frac{\alpha\chi(1-\chi)}{\sqrt{1-r^2}}. \quad (4.83)$$

We now try mixtures with a much larger difference in viscosity – we can choose $\gamma \in \{10^3, 10^6\}$, taking parameters $\mathcal{C}$, α, β, and χ_0 to be the same as in the previous section. The final droplet is then allowed to relax until it either reaches a stable equilibrium or touches down. Results for $\gamma = 10^3$ and $\gamma = 10^6$ are shown in figures 4.29 and 4.30 below.

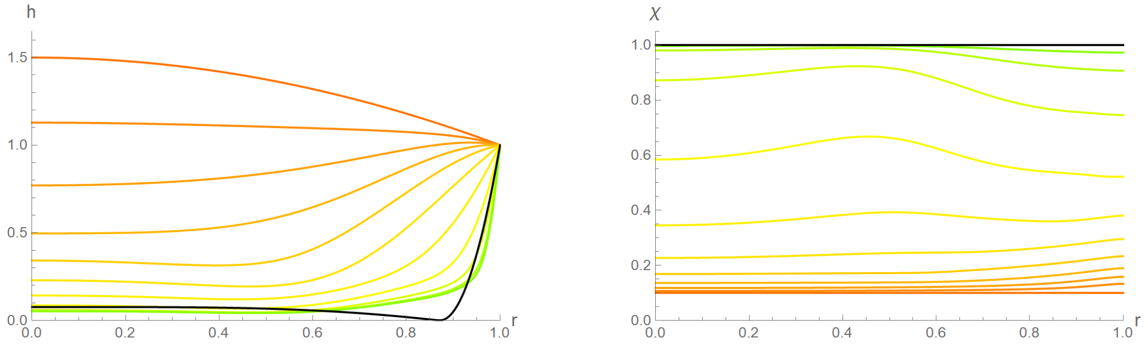

(a) Height

(b) Composition

Figure 4.29: Height and composition evolution for a droplet with viscosity as a logarithmic function of χ. $\mathcal{C} = 2$, $\alpha = 1$, $\beta = -0.04$, $\gamma = 10^3$, $\chi_0 = 0.1$.

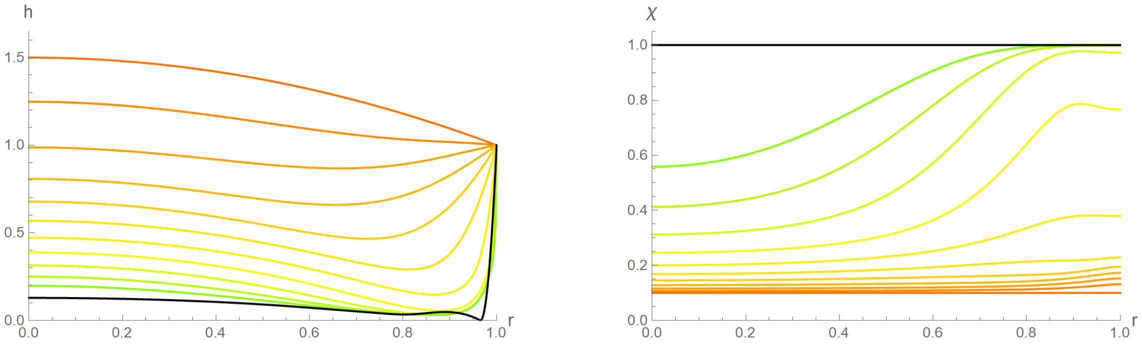

(a) Height (b) Composition

Figure 4.30: Height and composition evolution for a droplet with viscosity as a logarithmic function of χ. $\mathcal{C} = 2$, $\alpha = 1$, $\beta = -0.04$, $\gamma = 10^6$, $\chi_0 = 0.1$. Because the viscosity is very large, the liquid composition does not even out and become uniform and instead sees large growth at the edge where the volatile component evaporates most quickly.

The latter graphs show that, as we should expect, the flow of components is hindered by the large increase in viscosity of component χ, meaning the outer ring enrichment caused by the evaporative flux takes longer to equilibrate across the droplet (see figure 4.30b in comparison to figure 4.29b; while the latter certainly does not have flat composition, it is clearly more able to redistribute both components across the droplet than the former).

This leads to behaviour similar to decreasing $\mathcal{C}$ – although $\mathcal{C} = 2$ in figure 4.30a, it exhibits a W-shape more characteristic of a droplet with $\mathcal{C} = 0.2$ (see section 3.8.3). This makes sense once we realise that the system is operating with an effective $\mathcal{C}$ parameter that depends on composition; a back of the envelope calculation shows us that about halfway through the drying, estimating $\chi = 0.2$ and using $\gamma = 10^6$ and $\mathcal{C} = 2$, we have $\mathcal{C}_{\text{eff}} = \frac{\mathcal{C}}{\gamma^{\chi}} \approx 0.13$.

The black curves represent, again, the final state of the involatile component. As γ becomes large, the time taken for this viscous liquid to relax also increases,[6] and the final curve is determined by the shape of the volatile liquid in its late stages.

Above $\gamma = 10^3$ the relaxation was cut short by the droplet touching down. This may be responsible for the unexpected final shape we see in figure 4.30a – the W-shape present in the evaporation stage resulted in a liquid layer that touches down (in this case $r_{\text{td}} = 0.9675$) on its way to equilibrium. In order to determine the relaxed state of this kind of system we would need a model with additional boundary conditions that account for droplet splitting after touchdown. We have mentioned elsewhere that this kind of simulation is outside the scope of this project, but remind the reader that others have started to work on models that evaluate DiW profiles post-touchdown [3]. Given that a dynamic viscosity DiW model would be useful to understand the precise shape of a polymer deposit in a pixel, it will be important for future studies to incorporate equations such as 4.78, 4.79, 4.82, and 4.83.

---

[6] We are able to short-cut the relaxation by taking the fully evaporated solution and, exploiting the fact that is now a single, involatile liquid, evolving it using the code for a simple, non-evaporating droplet.

4.7.5 Comparison to Experimental Data

Although there does not exist much readily available experimental data in the literature for evaporation of binary DiWs, Zhida Huang has performed experiments analogous to the simulation presented in this chapter. The previous chapter alerted us to the possibility that the $\mathcal{C}$ parameter may have a discrepancy between the model and the experiment; here we have again been careful to analyse the data across multiple values of $\mathcal{C}$, α, and β to try to find the best fit.

In order to find the best fit for these three parameters, we started with their experimental values and gradually adjusted them by eye (using our experience of the influence that they have on the droplet shape). As in chapter 3, we determined the initial time-offset by fitting the curves to the experimental data at $r = 0$.

Given the complexity of the parameter space and the subtle changes that occur when varying $\mathcal{C}$, α, and β, we deemed this to be the most efficient method for matching experimental data. For future theory–data comparisons with a larger set of experimental results, it would be helpful to use machine learning/neural network techniques that could be trained to find the absolute best fit. The problem for the researcher would then become defining a response function that would avoid under- and overfitting errors; for example, we would want to avoid a response function that consistently finds a ‘correct’ fit that bears no visual similarity to the data, or one that produces such a complex curve that it accounts for every datapoint but sacrifices all physical insight.

n-Pentyl Acetate and n-Butanol

Using various sources [132, 133] and assuming surface tension varies linearly with temperature, we calculate the surface tension of n-pentyl acetate to be $\sigma_{\text{n-pent}} = 25.2$ mN m^{-1} at 25°C. n-butanol has a surface tension $\sigma_{\text{n-but}} = 24.2$ mN m^{-1} at 25°C [134, 135, 136], so β takes the value $\beta = -0.04$. If we allocate the symbol χ to n-pentyl acetate (therefore we use ξ for n-butanol), the experiment was performed with initial volume fraction $\chi_0 = 0.29$. The evaporation rates of the pure solvents were measured to be 82 pl s^{-1} for n-butanol and 52 pl s^{-1} for n-pentyl acetate, meaning we also have $\alpha = 0.37$. The cylindrical well had radius $R = 75\,\mu$m and height $h_0 = 2.09\,\mu$m and the experimental $\mathcal{C}$-parameter for this system was $\mathcal{C} = 1.85$ (we used the initial-volume-fraction-weighted viscosity).

We compare a simulation with these parameters to the experimental data in figure 4.31.

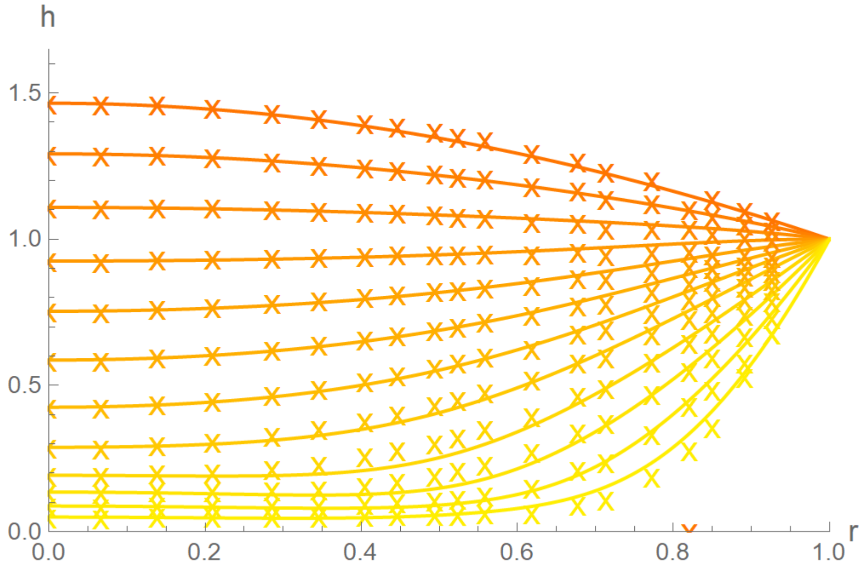

Figure 4.31: A comparison between simulation (solid lines) and experiment (crosses) for n-pentyl acetate and n-butanol. $\mathcal{C} = 2.5$, $\alpha = 0.37$, $\beta = -0.022$. Time increases from orange to yellow.

There are areas of both agreement and disagreement between the theoretical curves and the experimental data. Importantly, the flatter bottom associated with Marangoni flows at $\mathcal{C} \sim 1$ is present in both; in fact the theoretical curves towards the end of the drying quantitatively match the experimental data well from $r = 0$ until $r \approx 0.65$, when the droplet departs from its relative flatness. Furthermore, there is some small negative curvature due to the enrichment of the component with higher surface tension at the edge. Despite the slight loss of quantitative agreement near the edge, the positive curvature is in qualitative agreement between the two.

Toluene and n-Butanol

Toluene has a surface tension of $\sigma_{\text{tol}} = 27.7\,\text{mN m}^{-1}$ at 25°C [137], and was measured to evaporate at 414 pl s^{-1}. The well has dimensions $R = 77\,\mu\text{m}$ and height $h_0 = 2.25\,\mu\text{m}$, so for this system we have $\alpha = 0.80$, $\beta = 0.10$, and $\mathcal{C} = 1.13$. The initial volume fraction of n-butanol (here denoted by χ, due to its lower volatility) was $\chi_0 = 0.33$; this is therefore a droplet with both α and β positive. As for the agreement of the simulation, we had to dramatically reduce β to find a set of curves that qualitatively matched the experimental data – figure 4.32 shows a simulation with parameters $\alpha = 0.80$, $\beta = 0.01$, and $\mathcal{C} = 1.8$.

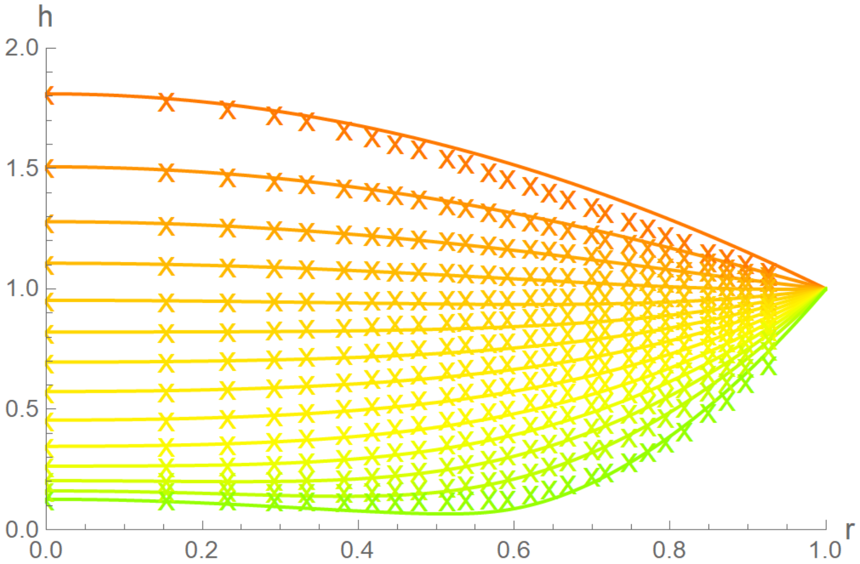

Figure 4.32: A comparison between simulation (solid lines) and experiment (crosses) for toluene and n-butanol. This comparison sees some discrepancy with the dimple, which is more pronounced towards the end of the evaporation in the simulation. Time increases from orange to green.

A factor that we have not yet considered is non-ideal mixing. Due to the difference in preferred bonding interactions between the two chemicals (e.g. hydrogen bonding in the alcohol n-butanol and the van der Waals force in toluene), the vapour pressure of the binary mixture deviates from the ideal (pure) situation described by Raoult's law, in which vapour pressure varies linearly with volume fraction. In general, we may see positively curved, negatively curved, and more complex vapour pressure-volume fraction relationships, depending on the chemicals involved. Not only this, the surface tension relationship will no longer be a linear function of volume fraction. Although it is difficult to predict the exact functional relationship in our experimental scenario, it is likely that both α and β ought to be lower than reported experimentally, as toluene (the component with larger evaporation rate and surface tension) bonds with the weaker intermolecular force.

Moreover, the first set of data points drops lower than the corresponding simulated curve at large r, meaning the experimental time offset is significant enough that the initial condition will have slightly changed. In other words, the first data curve is certainly not a spherical cap, and it is highly likely that the corresponding composition curve is no longer uniform. In order to account for this we would have to also take $\chi_0(r)$ as a variable parameter.

Despite the evident quantitative issues in this case, the qualitative trends show some agreement. Most prominently, the late-stage negative curvature near the centre of the experimental data is reproduced well in the simulation, as is the general behaviour at the beginning of the drying. We do, however, see the usual discrepancy near the edge of the well, and the final simulated curve exhibits too sharp a dip, despite us having reduced β.

4.8 Conclusion

In this chapter we have extended the model for a pure DiW to include binary droplets; we first introduced two new parameters, α and β, to describe the relationship between the evaporative fluxes and surface tensions of the two components respectively. This introduced new terms into the lubrication equation and alters the behaviour of the droplet as it dries.

We found that the droplet's shape depends on the surface tension difference and gradients in composition; areas that become depleted or enriched with one component over the other exert forces on the surface that cause curvature not observed in pure droplets, most notably the emergence of negative curvature at the edge. We suggest that the mechanism for this effect is the enrichment of the component with higher surface tension near the edge of the droplet (due to the preferential evaporation there and the larger volatility of the other component), which proceeds to exert an attractive Marangoni force on surrounding liquid. We also observed the opposite of this – when one component has higher volatility and surface tension we see an enhanced W-shape because of the enrichment of the other component at the edge, which induces a repulsive Marangoni force on surrounding liquid.

The Marangoni effect doesn't only enhance and create mounds, it also appears to provide a flattening effect near the end of the drying. We performed analogous simulations to those in chapter 3, observing the late-stage shape of the interface as we varied $\mathcal{C}$ over several orders of magnitude, and determined that the W-shape profiles we observed previously are suppressed and U-shaped profiles are enhanced (in fact they actually look like the letter U now!) when β is negative. Inspecting the velocity profiles revealed recirculation flows in these droplets, regions in which the flow direction turned inwards. We hypothesised that the emergence of these recirculation regions is a contributing factor to the flattening of an otherwise W-shaped droplet, but does not have the same effect on droplets with a large enough $\mathcal{C}$ – these droplets continue to be approximately C-shaped.

Our model made it easy to simulate a droplet with one component evaporating and the other involatile. During the evaporation stage, the droplet exhibits the same shape features as when both are evaporating: curvature inversion and flatter bottoms. However, we also found them interesting in the relaxation stage, after all the volatile material had evaporated: if the initial volume fraction of χ was in a critical range (low enough that it could not form a quadratic bowl, high enough that the droplet did not touch down from evaporation), we eventually observed a stable, dimpled height profile with two sections, each a different solution of the pure, involatile lubrication equation.

This led us to investigate the effect of viscosity – could we attempt to simulate an approximate polymer-alcohol mixture whose final solution would be the polymer deposit? We found that we could determine a deposit shape for systems in which the viscosity of the involatile component was below a certain value, otherwise the pre-relaxation shape of the involatile droplet would touch down before it could fully relax.

Finally, we compared our simulation to some experimental data, noticing that it matched data well in situations with small β, particularly near the centre of the droplet. It could reproduce the Marangoni mound effect we see in experiments (both at the edge for negative β and at the centre for positive β) and also the flat bottom desirable for many CRE suppression applications. However, we recognise that the model departs from experiment rapidly once β becomes large and negative – there were some qualitative features it was unable to reproduce.

Having developed and tested a model for a binary DiW, finding some success and some areas for development, we shall now return to the evaporative flux. In the entirety of this chapter we have been using the functional form $\frac{1}{\sqrt{1-r^2}}$ consistently; however this is not necessarily true for the evaporative flux of each individual component in a droplet whose composition is constantly changing. In the next chapter we will take a different approach and attempt to solve a two-sided (liquid-vapour) model to determine the evaporative flux of each component dynamically.

Chapter 5

Two-Sided Model

Popov's model offers an accurate representation for the evaporative flux from a pure droplet drying in a well. However, the extent of its validity for binary droplets with non-uniform distribution of components is unclear.

In this chapter we shall consider explicitly the vapour field generated by a binary droplet and compare the solution to the Popov form. The vast majority of works on this topic assume that material transport across the interface is diffusion-dominated and fast, and therefore the vapour concentration can be described by a Laplace equation in two dimensions. The argument for this simplification is best expressed in Hu and Larson's 2002 paper [9], where they argue that the speed at which the vapour reacts to changes in the droplet shape is 10^5 times faster than the rate of evaporation, which can thus be considered a quasi-steady process.

We will incorporate a finite element solution to the Laplace equation into the binary droplet model to simulate dynamically changing evaporative flux; this is the first time dynamically varying flux has been implemented for a binary DiW and it appears to go some way to rectifying numerical discrepancies in the model from the previous chapter.

5.1 Vapour Phase Problem Formulation

According to Fick's law, the evaporative flux of a component from a droplet mixture is proportional to the concentration gradient of that component in the gas directly above the droplet,

$$\hat{J}_i(\hat{r}) = -D_i M_m^c \frac{\partial \hat{c}_i}{\partial \hat{z}}\bigg|_{\hat{z}=\hat{h}}, \tag{5.1}$$

where c_i is the vapour concentration of component i, M_m^c is its molar mass, and D_i is the diffusion coefficient of component i in air. Under the assumption of fast vapour relaxation, the concentration is described by a time-independent Laplace equation. We once again start by not specifying a particular geometry, using r to denote the horizontal space variable. We also change vertical notation when talking about the vapour system, using Z for the vertical space variable. The system comprises a Laplace equation for the concentration of each component, $i = \chi, \xi$,

$$\hat{\nabla}^2 \hat{c}_i = 0\,, \tag{5.2}$$

with mixed boundary conditions that define the concentration at the interface (with c_0 the saturation concentration, and assuming Raoult's Law again),

$$\hat{c} = c_0\chi(\hat{r}) \text{ on } \hat{z} = \hat{h}, \ \ 0 < \hat{r} < R, \tag{5.3}$$

the lack of flux across the substrate,

$$\frac{\partial \hat{c}}{\partial \hat{z}} = 0 \text{ on } \hat{z} = h_0, \ \ \hat{r} > R, \tag{5.4}$$

the symmetry across the centre of the droplet,

$$\frac{\partial \hat{c}}{\partial \hat{r}} = 0 \text{ on } \hat{r} = 0, \tag{5.5}$$

and the far field limit,

$$\hat{c} \to c_\infty \text{ as } \hat{r}^2 + \hat{z}^2 \to \infty. \tag{5.6}$$

For pure droplets, equation 5.3 loses its dependence on χ and becomes constant. We nondimensionalise with the following scale factors,

$$\hat{r} = Rr, \qquad \hat{z} = RZ, \qquad \hat{h} = h_0 h'$$

$$\hat{c} = c_\infty + (c_0 - c_\infty)c, \qquad \hat{J} = \frac{D_{\chi\xi}M_m^c}{R}(c_0 - c_\infty)J,$$

and the system becomes

$$\nabla^2 c = 0, \tag{5.7}$$

$$c = \chi(r) \text{ on } Z = 0, \ \ 0 < r < 1, \tag{5.8}$$

$$\frac{\partial c}{\partial Z} = 0 \text{ on } Z = 0, \ \ r > 1, \tag{5.9}$$

$$\frac{\partial c}{\partial r} = 0 \text{ on } r = 0, \tag{5.10}$$

$$c \to 0 \text{ as } r^2 + Z^2 \to \infty. \tag{5.11}$$

We note that the aspect ratio $\varepsilon = \frac{h_0}{R}$ is small again, meaning we can linearise the droplet into Z=0.

5.2 Analytical Solution

This system can be solved analytically in the specific case of a pure droplet with a saturation concentration that does not depend on space, for which $\chi(r) = 1$. The analytical solution in cylindrical geometry is given in [3] and has the form

$$c(r, Z) = \sin^{-1}\frac{2}{((1+r)^2 + Z^2)^{\frac{1}{2}} + ((1-r)^2 + Z^2)^{\frac{1}{2}}}, \tag{5.12}$$

which leads to the familiar Popov form of the evaporative flux[1],

$$J = \frac{1}{\sqrt{1-r^2}}. \tag{5.13}$$

In the rather more general case of a spatially varying boundary condition along the droplet interface, the system cannot be expressed analytically and the above system must be solved numerically.

5.3 Finite Element Method

With the vapour relaxation timescale being much smaller than that of the liquid, and assuming the droplet is sufficiently small compared to the vapour field that we may linearise the interface to $Z = 0$, we would like to solve the system comprising equations 5.7-5.11. A popular computational technique used to numerically solve problems such as this is the finite element method; we consider a domain comprising the double positive quarter circle with origin at the centre of the droplet and radius R_∞ and subdivide it into an unstructured triangular mesh (using Mathematica's DiscretizeRegion function on part of a Disk Region). It is important that R_∞ be sufficiently large for the far-field boundary condition to be applied there. Given that we are only interested in the concentration field very near to the droplet, we refine the mesh in the vicinity of the droplet and coarsen it continuously as $r^2 + Z^2$ increases until it reaches Mathematica's default coarseness sufficiently far from the droplet.

The finite element model we use is that of Alberty *et al.* [107], but we alter their cartesian-coordinate derivation in order to move the problem to cylindrical polar coordinates and to impose our own boundary conditions. While it is not necessary to reproduce their entire argument here, we shall explain these alterations to the model; if the reader is interested in the rigorous approach to deriving the finite element model, the paper can be found in the citation above (*Remarks around 50 lines of Matlab: short finite element implementation*; Alberty, Carstensen, and Funken).

First, the authors derive their model in cartesian (x, y) coordinates. The choice of coordinates is expressed mathematically via the basis functions of the triangulation $\mathcal{T}$, $\eta(x, y)$; for a triangulation that uses only triangles (as opposed to one with quadrilaterals), each triangular element $\triangle$ has vertices at (x_1, y_1), (x_2, y_2), and (x_3, y_3), and corresponding basis functions η_1, η_2, and η_3. These basis functions satisfy

$$\eta_j(x_k, y_k) = \delta_{jk} \,. \tag{5.14}$$

The entry of the stiffness matrix is a product of basis function gradients integrated over the triangle (though it turns out that the basis function gradients are independent of x and y for each triangle),

---

[1] D'Ambrosio *et al.*'s slightly different nondimensionalisation leads to a factor of $\frac{2}{\pi}$ that we do not have.

$$M_{jk} = \int_{\triangle} \nabla\eta_j(\nabla\eta_k)^{\mathrm{T}} dxdy$$
$$= \frac{1}{(2|\triangle|)^2}(y_{j+1}-y_{j+2}, x_{j+2}-x_{j+1})\begin{pmatrix} y_{k+1}-y_{k+2} \\ x_{k+2}-x_{k+1}\end{pmatrix} \cdot |\triangle|, \quad (5.15)$$

with indices modulo 3. The integral is modified in cylindrical coordinates by the radial location of the triangle (the Jacobian of the integral), here we use Pappus's second centroid theorem,

$$M_{jk} = 2\pi \int_{\triangle} \nabla\eta_j(\nabla\eta_k)^{\mathrm{T}} dZ\, r\, dr$$
$$= \frac{2}{\pi(2|\triangle|)^2}(Z_{j+1}-Z_{j+2}, r_{j+2}-r_{j+1})\begin{pmatrix} Z_{k+1}-Z_{k+2} \\ r_{k+2}-r_{k+1}\end{pmatrix} \cdot |\triangle| \cdot \frac{1}{3}(r_1+r_2+r_3)\,, \quad (5.16)$$

where the final term is the radial coordinate of the barycentric centroid of the triangle. We have here moved from (x, y) to (r, z), with the basis functions now

$$\eta_j(r_k, Z_k) = \delta_{jk}\,. \quad (5.17)$$

Second, our boundary conditions are (for component χ; the boundary conditions for component ξ are defined analogously)

$$c = \chi(r) \;\text{ on }\; Z = 0,\; r \le 1\,, \quad (5.18)$$

$$\frac{\partial c}{\partial Z} = 0 \;\text{ on }\; Z = 0,\; r > 1\,, \quad (5.19)$$

$$\frac{\partial c}{\partial r} = 0 \;\text{ on }\; r = 0\,, \quad (5.20)$$

$$c = 0 \;\text{ on }\; r^2 + Z^2 = R_\infty^2\,. \quad (5.21)$$

We then formulate the system in the same way as in the Alberty paper, except we denote the variable for which we are solving as C, that is, the discrete approximation to $c(r, Z)$.

5.4 Deriving the Evaporative Flux

Once the system has been solved (i.e. C has been found) it remains to determine the evaporation rate from the gradient near $Z = 0$. We assume the gradient is constant inside every triangle (discontinuous, but approximable, at triangle edges and nodes) and use barycentric coordinates to calculate the concentration at two points along a vertical line inside each triangle. The constant vertical gradient can be easily computed with this information;

$$\frac{\partial c_\triangle}{\partial Z} = \frac{c_{\triangle,2} - c_{\triangle,1}}{z_2 - z_1} \;\text{ for }\; \triangle \in \mathcal{T} \quad (5.22)$$

and where numerical subscripts indicate each point on the vertical line in the triangle.

We calculate the gradient on each mesh node along the droplet by taking the area-weighted mean of gradients in the triangles that have one vertex coinciding with the node. The evaporative flux at the i^{th} node is then just

$$J_i = -\frac{\partial c}{\partial Z}\bigg|_i . \tag{5.23}$$

Given that the nodes are not, in general, located at the grid points of the droplet simulation, we then have to compute an interpolation function, J_{int}, for the evaporative flux. We can then use this to determine the evaporation at each grid point.

5.5 Finite Element Results

Using this method we were able to solve the diffusion equation with any arbitrary initial condition on the droplet. We initialise a quarter circle mesh with a large radius, R_∞, that is refined near the droplet (specifically in the quarter circle $r^2+z^2 \leq 1$) and becomes less refined far from the droplet. This is shown in figure 5.1. The mesh refinement function is

$$A_T < \begin{cases} 1\times 10^{-4} & r^2+Z^2 \leq 1 \\ 1\times 10^{-4}\, e^{I_{\text{mesh}}(r^2+Z^2-1)} & r^2+Z^2 > 1\,, \end{cases} \tag{5.24}$$

where A_T is the area of a triangle in the mesh and I_{mesh} is the rate at which the triangles increase in size. The cells grow up to a maximum size.

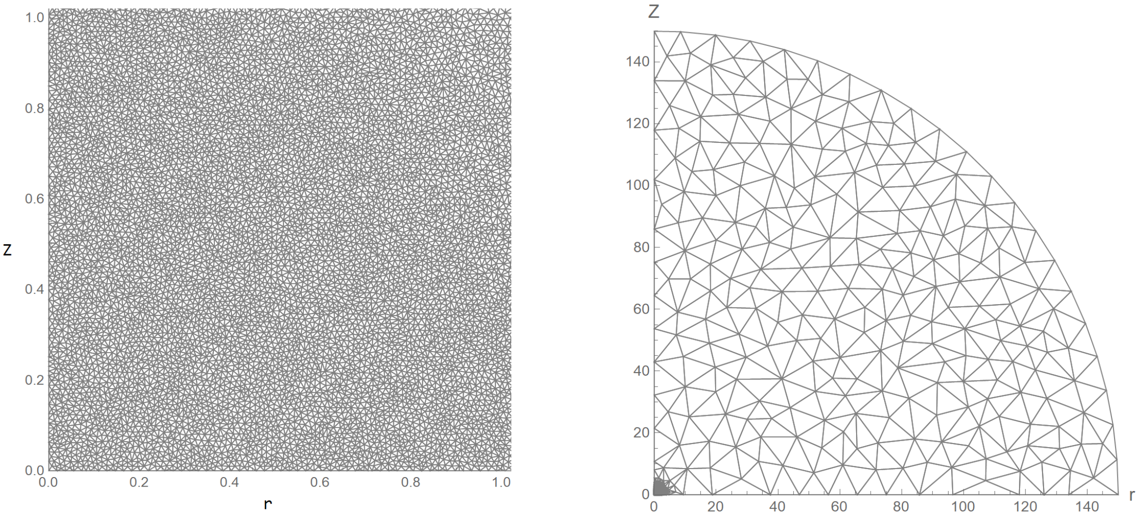

(a) The mesh near to the droplet.

(b) The mesh far from the droplet.

Figure 5.1: A close-up and far-away view of the mesh used for FEM analysis. Here $R_\infty = 150$.

Figure 5.2 shows that the simulation performs as expected for a droplet with uniform concentration; the concentration contours of figure 5.2b are largely similar to the analytical case using equation 5.12, which is shown in figure 5.2a.

The important part of this solution is the concentration just above the droplet, more specifically its gradient, as this is what we use to determine the evaporative flux. Figure 5.3 shows that the gradient of the finite element solution matches Popov's analytical solution well.

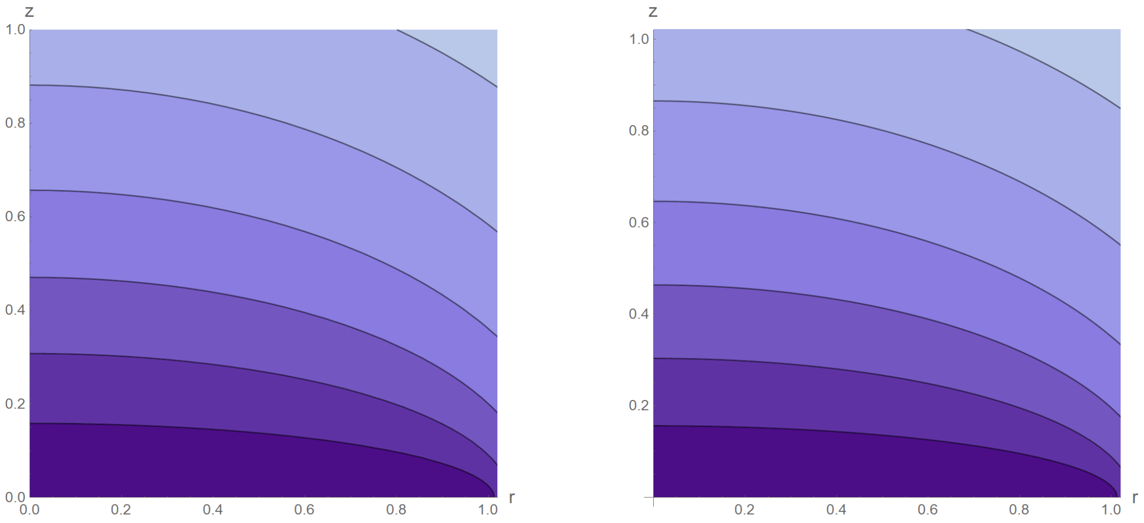

(a) Theoretical concentration field (b) FEM Solution of Diffusion Equation

Figure 5.2: FEM reproduction of the theoretical concentration field above a thin droplet.

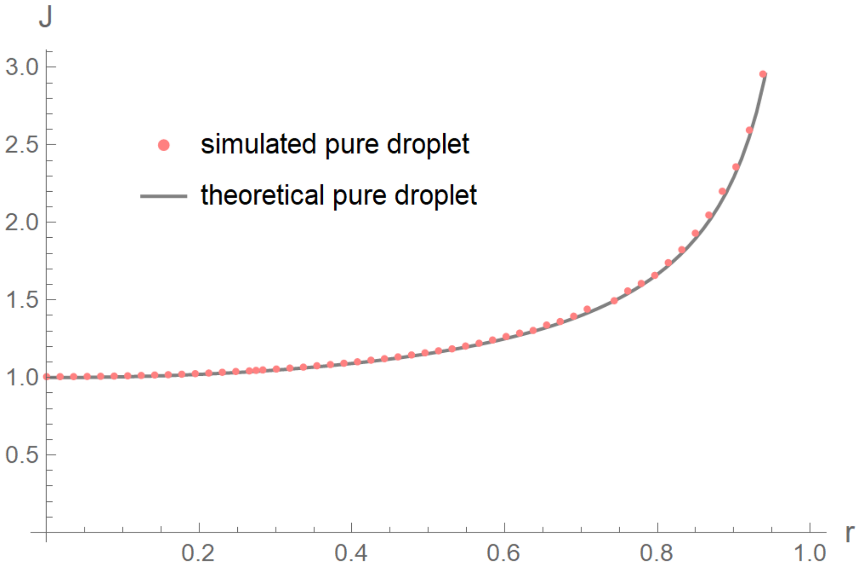

Figure 5.3: Comparison between Popov's theoretical evaporation rate and computed evaporation rate for a pure droplet. In this case $I_{\text{mesh}} = 0.4$ and $R_\infty = 150$.

5.6 Error Quantification

We can quantify the error associated with the discretisation of the domain by varying a few key parameters for a simulation of a pure droplet and comparing the evaporation rate results with the theoretical form.

In this section, the word ‘error’ refers specifically to the percentage error of the finite element vapour field solution compared to the analytical solution, equation 5.12.

5.6.1 Finite Far-Field

In a simulation it is clear that the far-field boundary condition must be imposed a finite distance from the droplet. This will lead to an error in the calculation of the vapour field that, in turn, will cause an error in the computed evaporation rate. Figure 5.4 is a scatter plot of the percentage error of the simulated vapour field from the analytical solution.

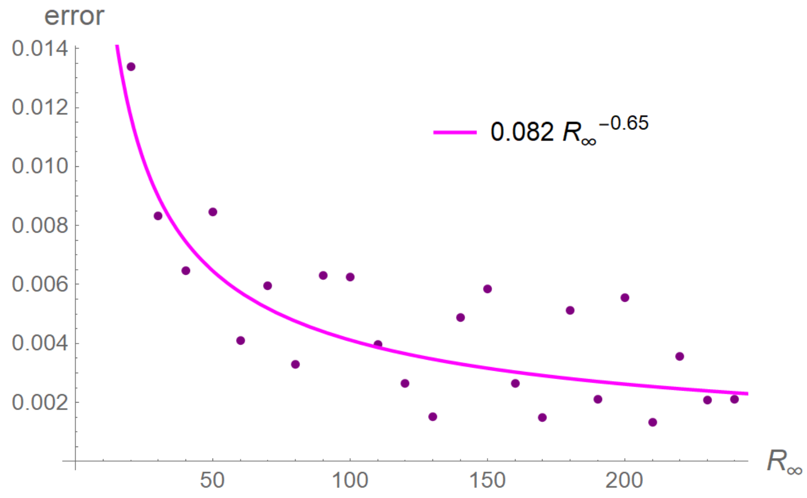

Figure 5.4: The error on evaporation rate associated with imposing a finite far-field condition compared to the theoretical form. The best-fit trend is reciprocal; following the same logic as in chapter 3 we conclude that the error is integrably finite as $R_\infty \to \infty$.

We can see from this plot that there is some degree of randomness involved in the imposition of the boundary condition – this is because the mesh must be recomputed for each value of R_∞. However, it is evident that the error tends to decrease as R_∞ increases, albeit relatively slowly.

5.6.2 Domain Discretisation

We can also measure how the error changes with the refinement of the discretisation. A good measure for this feature is the number of coordinate points in the mesh. First we examine the number of points in the largely unrefined outer region, N_{outer}, shown in figure 5.5. In these simulations we have used $R_\infty = 210$ and the number of points in the refined, inner region $N_{\text{inner}} \approx 6000$.

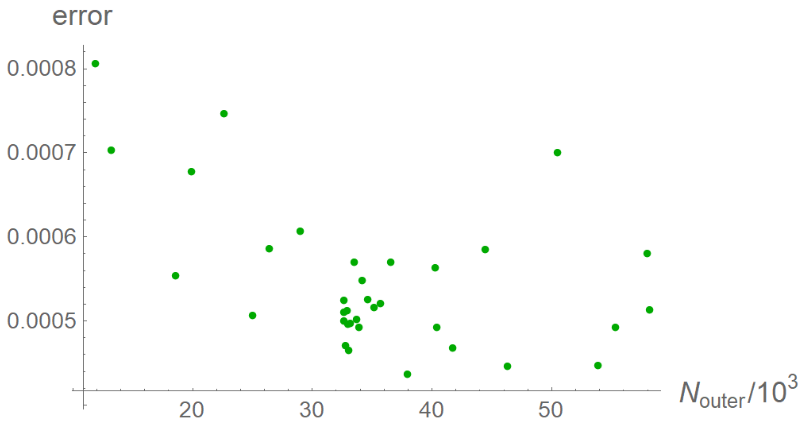

Figure 5.5: The error associated with the discretisation of the whole quarter circle domain. Although the error appears to decrease initially, there is no discernable trend after $N_{\text{outer}} = 30,000$.

We can again see that the accuracy increases as we increase the number of points from 10,000 to 30,000, but there is no discernible increase in accuracy associated with refining the mesh far from the droplet beyond this number. This is to be expected – for us, a rarefied mesh far from the droplet exists only to permit us to impose the far-field condition (analysed above in section 5.6.1); the critical part of the vapour field as far as the evaporative flux is concerned is the region directly above the droplet.
It is a different story when we look at the mesh near to the droplet. Figure 5.6 displays the relationship of the error to the number of points within the unit quarter circle centred on the origin. We have used $R_\infty = 210$ again and $N_{\text{outer}} \approx 36,000$.

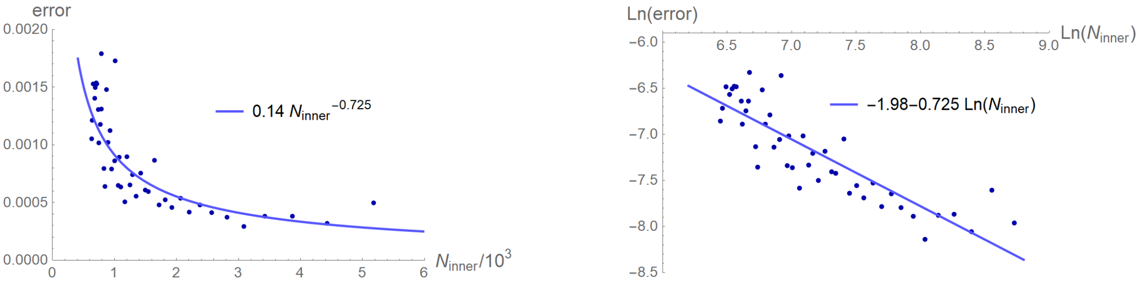

(a) A direct plot of error against number of inner points.

(b) A log-log plot that reveals a reciprocal relationship between error and number of inner points.

Figure 5.6: The error associated with the refinement of the unit quarter circle mesh near to the droplet. In this case, the error again follows a reciprocal relationship, indicating it is integrably finite as $N_{\text{inner}} \to \infty$.

Figures 5.6a and 5.6b equivalently demonstrate that the higher the density of points in the refined region near to the droplet, the smaller the error by the inverse power shown. Following an analogous argument to that in chapter 3, we conclude that the error approaches zero as the number of points approaches infinity.

5.7 Incorporation into Method-of-Lines Algorithm

We are able to avoid the need for an explicitly time dependent simulation of the vapour phase for two reasons. We saw in chapter 2 that Hu and Larson established that the vapour phase relaxes about 10^5 times faster than the droplet, meaning all changes in the gas above the droplet can be modelled to happen instantly compared to the evaporation. Additionally, in our simulations composition gradients generally emerge slowly compared to the evaporation.

Therefore we choose a composition change condition that, when met, pauses the simulation, recalculates the vapour field, and updates the evaporative flux for each component. It remains to decide on a condition; since we are particularly interested in composition gradients and not necessarily absolute composition, we choose to modify the evaporative flux whenever any of the discrete composition points changes by 0.02.

5.8 Comparison To Static Evaporation

Varying the evaporative flux in this way tends to provide an overall smoothing effect on the composition – an overload of one component somewhere in the droplet causes the evaporative flux of that component to increase at that location too, meaning the composition somewhat self-regulates. The gradients are therefore gentler and Marangoni effects are reduced, though still present. We can see all this in figures 5.7, 5.10, and 5.11. Figure 5.7 displays a comparison between static and dynamic evaporation for a droplet of $\mathcal{C} = 0.02$; this of the three plotted values of $\mathcal{C}$ shows the largest difference. The difference is emphasised when we examine the radial surface curvature, shown in figure 5.8: where the droplet with static evaporation exhibits strong curvature inversion near the edge, it is a much weaker and more short-lived effect in the case with dynamic evaporation. In fact, we notice that it exhibits fairly strong positive curvature at about the halfway point of evaporation instead.

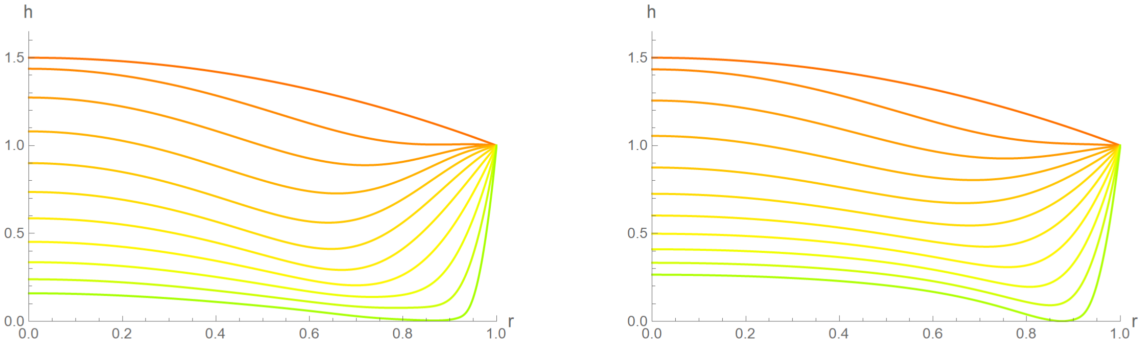

(a) Static Evaporation

(b) Dynamic Evaporation

Figure 5.7: A comparison between identical droplet evaporation processes, one with constant evaporative flux and the other with variable evaporative flux. $\mathcal{C} = 0.02$, $\alpha = 0.6$, $\beta = -0.08$. Dynamic evaporation decreases the W-shape suppression caused by the Marangoni effect.

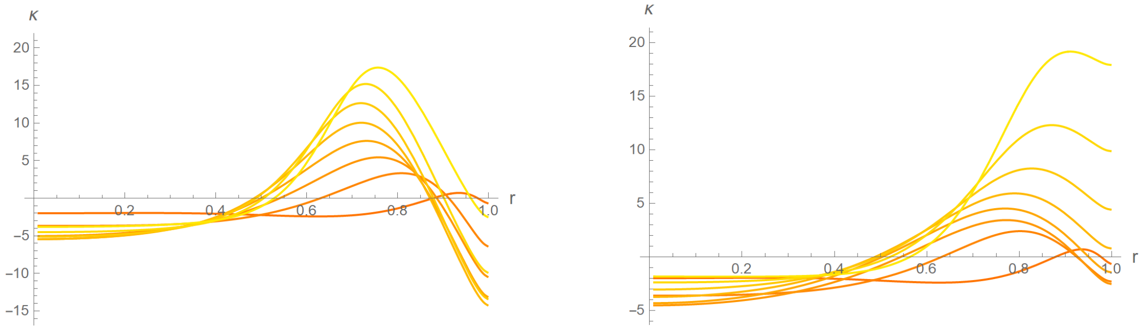

(a) Static evaporation

(b) Dynamic evaporation

Figure 5.8: A comparison of the curvature across the whole droplet between static and dynamic evaporation. Includes times between $t = 0.02$ and $t = 0.54$; as usual, early times are orange and become more yellow as time progresses. $\mathcal{C} = 0.02$, $\alpha = 0.6$, $\beta = -0.08$

The stabilising effect of dynamic evaporation can also be seen by comparing the composition variables, figure 5.9. Both droplets start similarly, with the predictable increase in χ near the edge, where component ξ evaporates most quickly. However, where the statically evaporating droplet has χ running unchecked, the dynamically evaporating droplet clearly limits the extent to which composition gradients can occur.

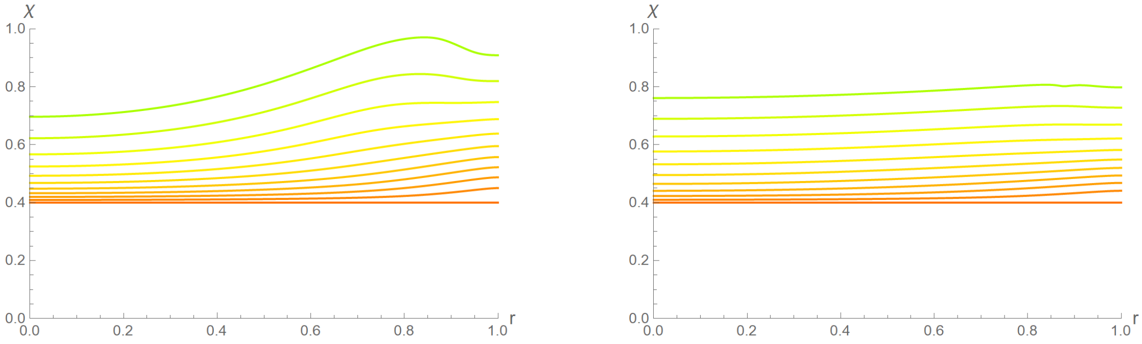

(a) Static Evaporation

(b) Dynamic Evaporation

Figure 5.9: Composition comparison for $\mathcal{C} = 0.02$, $\alpha = 0.6$, $\beta = -0.08$. The effect of dynamic evaporation is clear: composition gradients are much less pronounced, hence the suppression of the Marangoni effect.

Figure 5.10 displays the same comparison up an order of magnitude in $\mathcal{C}$. Immediately we see that the difference is much smaller and, although the W-shape reemerges with dynamic evaporation, you would be forgiven for taking them to be identical, at first glance at least. Figure 5.11, an order of magnitude higher again, prompts us to wonder if the effect of dynamic evaporation wanes with increasing $\mathcal{C}$.

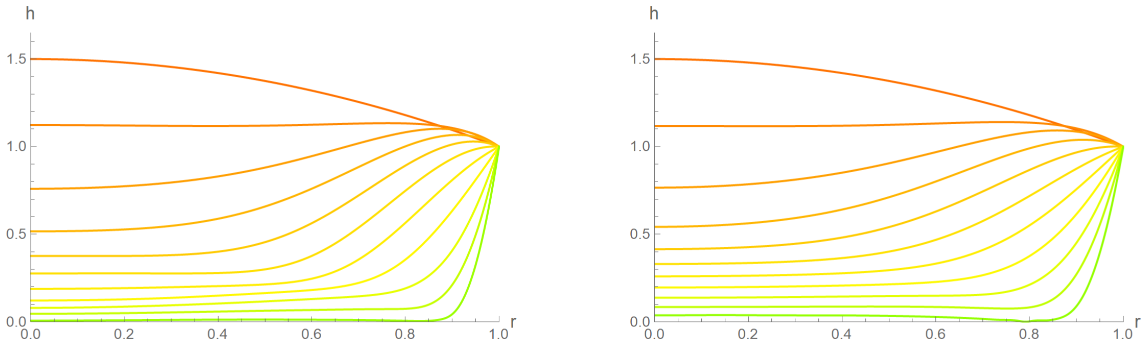

(a) Static Evaporation (b) Dynamic Evaporation

Figure 5.10: A comparison between identical droplet evaporation processes, one with constant evaporative flux and the other with variable evaporative flux. $\mathcal{C} = 0.2$, $\alpha = 0.6$, $\beta = -0.08$. At this larger value of $\mathcal{C}$ the dynamic flux does not oppose Marangoni flows as much as in figure 5.7.

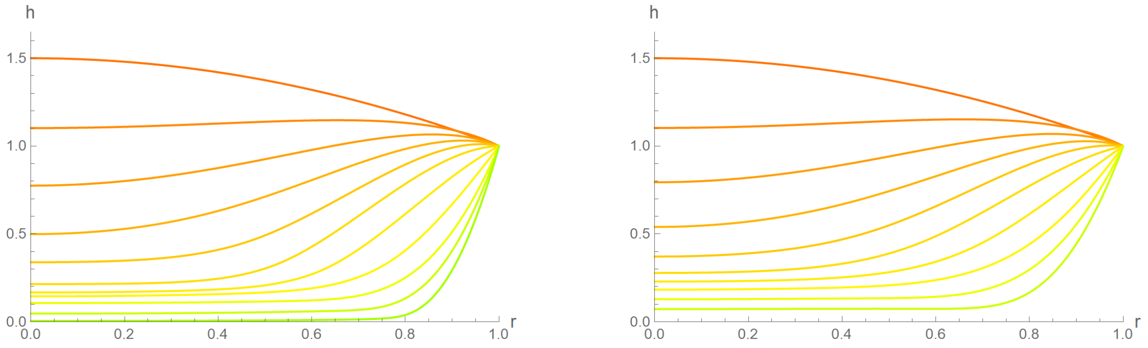

(a) Static Evaporation (b) Dynamic Evaporation

Figure 5.11: A comparison between identical droplet evaporation processes, one with constant evaporative flux and the other with variable evaporative flux. $\mathcal{C} = 2$, $\alpha = 0.6$, $\beta = -0.08$. At this larger value of $\mathcal{C}$ the dynamic flux does not oppose Marangoni flows as much as in figure 5.7.

5.8.1 Impact of $\mathcal{C}$, α, and β on Static vs Dynamic Flux

We can examine the mean difference between the curves at each time point; data is presented in figure 5.12. The difference does indeed reduce for larger values of $\mathcal{C}$, at least initially. This indicates that, depending on our accuracy requirements for any given simulation, we may choose a value of $\mathcal{C}$ below which to perform dynamic experiments and above which to revert to static (less computationally expensive) experiments.

However, the tendency towards uniformity between static and dynamic evaporation does not continue indefinitely; we can see in figure 5.12b that the difference has increased again for $\mathcal{C} = 20$ (the comparison for which is presented in figure 5.13). Evidently, those simulations that change the most after switching to dynamic evaporation are the ones with the fastest and sharpest changes in the composition, but due to the complexity of the parameter space it is difficult to identify a sole determining factor for this variable.

Other work on binary sessile droplets asserted that a two-sided model was essential for agreement with experimental data, partly because of the large composition gradients that would appear where the droplet became thin at the contact line (we report similar gradient behaviour in chapter 4) [56]. This might be part of the reason for the similarity we see at $\mathcal{C} \approx 2$ – the droplets at this level are quite flat and, critically, they become thin uniformly (except near the edge, where the droplet is pinned). This does not give the droplet much of a chance of forming strong composition gradients in the first place.

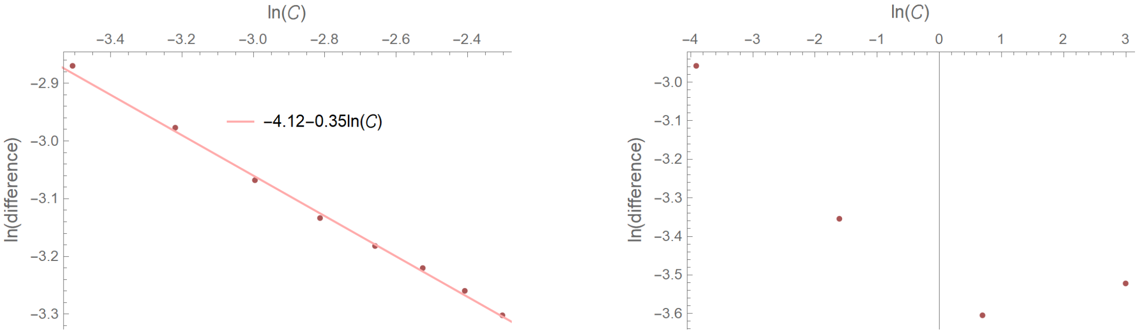

(a) Within order of magnitude $\mathcal{C} \sim 10^{-2}$

(b) Across four orders of magnitude $\mathcal{C} \in \{10^{-2}, 10^{1}\}$

Figure 5.12: Numerically comparing droplets with static and dynamic evaporative fluxes. There is a minimum in difference between static- and dynamic-flux results at $\mathcal{C} \approx 2$.

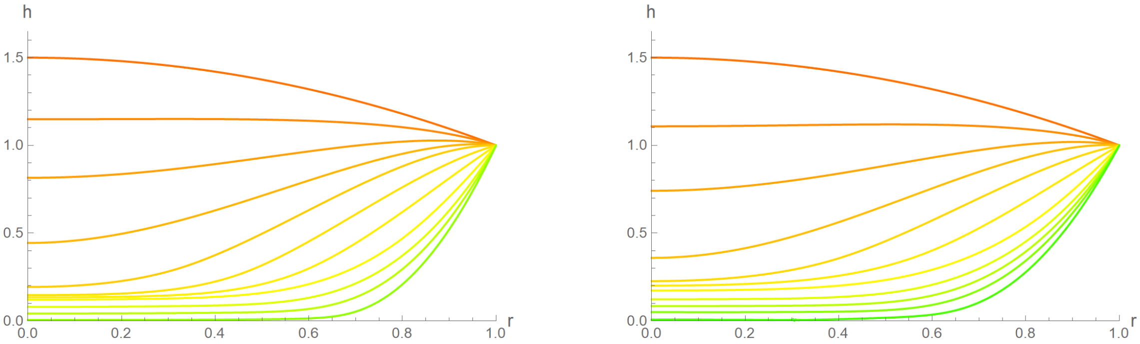

(a) Static Evaporation

(b) Dynamic Evaporation

Figure 5.13: A comparison between identical droplet evaporation processes, one with constant evaporative flux and the other with variable evaporative flux. $\mathcal{C} = 20$, $\alpha = 0.6$, $\beta = -0.08$.

Examining the dependence of static-dynamic difference on parameters α and β, we find the relationships depicted in figure 5.14. When α is very small or very large, the droplet approaches pure droplet behaviour; $\alpha = 0$ affords no opportunity for composition gradients because both components evaporate at the same rate (this is effectively a pure droplet), and $\alpha = 1$ simulations finish with a pure droplet, which will relax to the same shape regardless of whether the flux is dynamic or static. Therefore, as can be seen in figure 5.14a, the peak dynamic/static difference is observed at $\alpha \sim 0.5$.

The relationship for β is a different story (figure 5.14b). As β gets large and negative, the dynamic flux has a larger effect because Marangoni forces are acting to pull liquid to the edge of the droplet, where the evaporative flux is always enhanced. This phenomenon serves to increase the nonuniformity of χ across the droplet. Of course, the droplet is most similar to a pure DiW at $\beta = 0$, so we are not surprised that there is a minimum at that point. And as β becomes more positive, the potency of the dynamic flux seems to decrease again; the opposite effect is occurring, where liquid is drawn to the less volatile centre of the droplet by Marangoni forces.

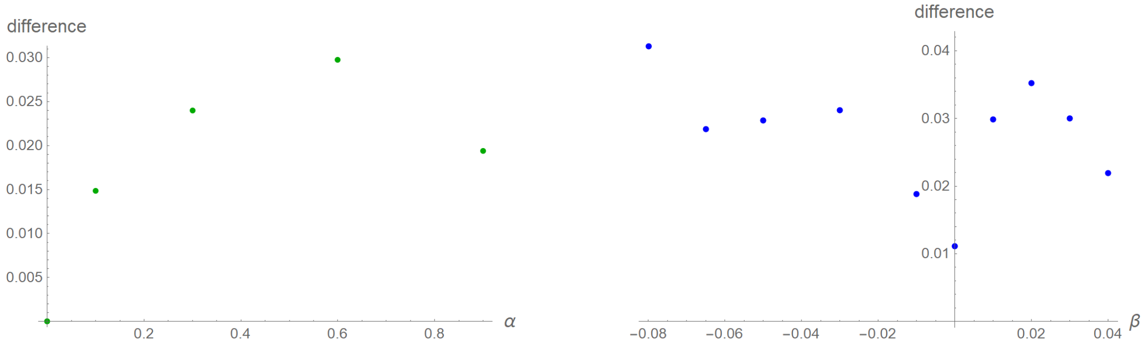

(a) $\alpha \sim 0.5$ is where large differences occur.

(b) Varying β gives a more complicated relationship.

Figure 5.14: Dynamic evaporation is more potent in droplets that exhibit large compositional deviations from uniform composition. $\mathcal{C} = 0.2$ in both; green dots are for α variation and blue dots are for β variation.

There is a small decrease in the difference between $\beta = -0.03$ and $\beta = -0.07$. The origin of this effect is unclear.

We have not included the final curve in figure 5.10 because it features a wave-like instability (figure 5.15) that is worth considering.

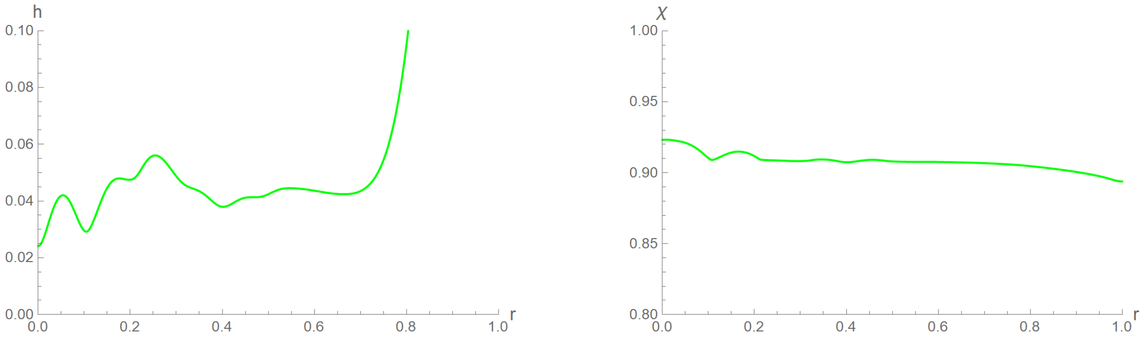

(a) Height (b) Composition

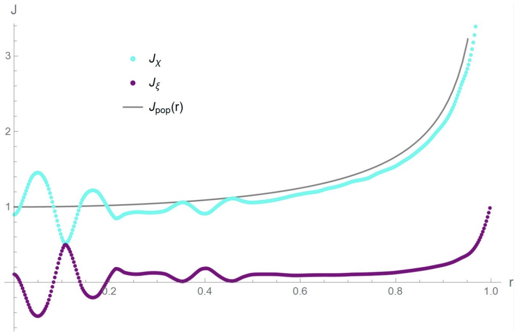

(c) Evaporative Flux

Figure 5.15: A numerical problem that features in the dynamic evaporation simulation with $\mathcal{C} = 2$, $\alpha = 0.6$, $\beta = -0.08$.

The instability appears in the same manner independent of the MoL discretisation and FEM mesh resolution; it is also clear from figure 5.15 that its wavelength is not related to either of these numerical approximations. Another snapshot (from the end of a simulation with $\beta = -0.04$) is shown in figure 5.16; here we can much more clearly see a sinusoidal instability emerging in the evaporative flux.

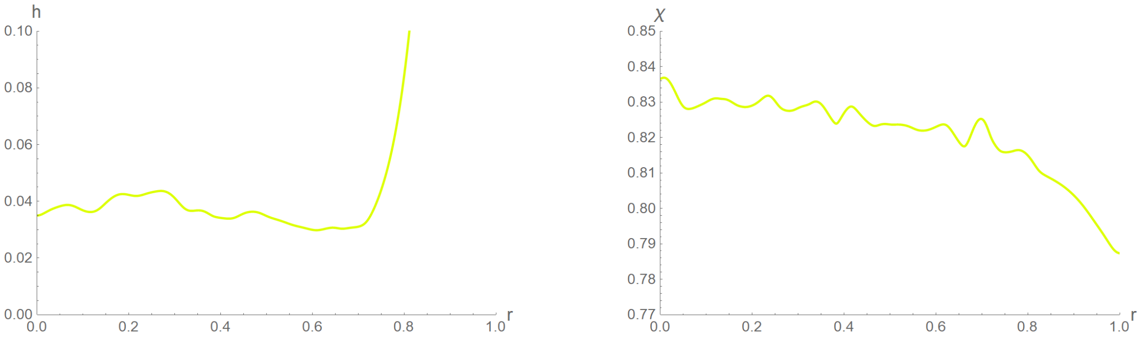

(a) Height (b) Composition

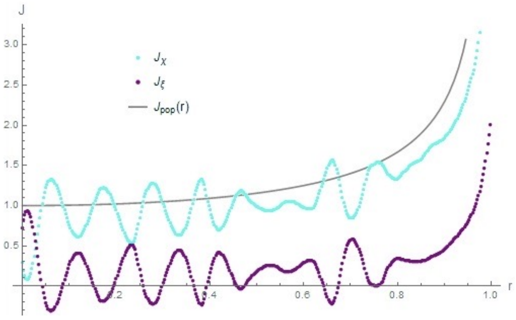

(c) Evaporative Flux

Figure 5.16: A numerical problem that features in the dynamic evaporation simulation with $\mathcal{C} = 2$, $\alpha = 0.6$, $\beta = -0.04$.

This instability appears for simulations with dynamic flux in the approximate range $2 < \mathcal{C} < 5$, with $\alpha > 0.3$ and $\beta < -0.03$ and only at very late time ($\sim 0.97t_{\text{td}}$). Therefore it is largely inconsequential for most applications of the DiW model, partly because we can safely analyse the droplets for 97% of their lifetime and partly because it is this range of $\mathcal{C}$ that bears most similarity to the static flux simulations. Although it would be beneficial to find its origin (particularly if one wanted a precise simulation at the moment of touchdown), it is enough to simply know to avoid this range of parameters when using dynamic flux.

5.9 Comparison to Experimental Data

In the same way as in chapter 4, we can compare the numerical simulation with dynamic evaporation to the experimental data for binary droplets.

5.9.1 n-Pentyl Acetate and n-Butanol

We return to the n-pentyl/n-butanol droplet from chapter 4, section 4.7.5 (the physical data can be found there also). The comparison between simulation and experiment is shown in figure 5.17, where the experimental value of $\mathcal{C}$ has been used instead of the best fit from the previous comparison; the experimental data is again represented by crosses and the simulation by solid lines.

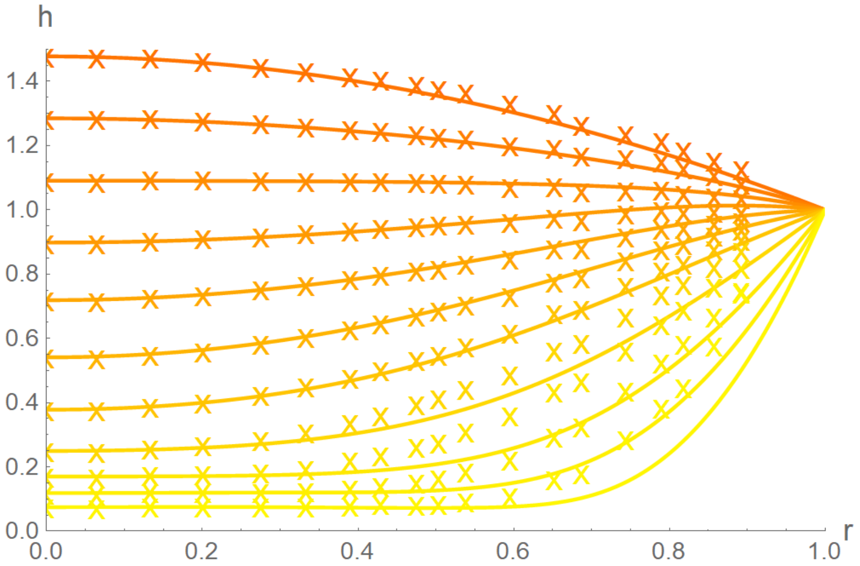

Figure 5.17: A comparison between simulation (solid lines) and experiment (crosses) for n-pentyl acetate and n-butanol. $\mathcal{C} = 1.85$, $\alpha = 0.37$, $\beta = -0.022$. Dynamic evaporation.

We notice that dynamic evaporation has brought us some success in aligning the theoretical $\mathcal{C}$-parameter with its experimental value, $\mathcal{C} = 1.85$ – certainly for the early stages of drying, the simulation has good agreement with the experimental data and we can see that it captures the curvature inversion near the rim again. At later stages disagreement emerges again; the simulated droplet is slightly flatter than the experimental one near the rim. We could write this off as experimental slippage of the pin, but it may also be a result of the weakness of the dynamic evaporation algorithm; evaporative flux does not change continuously, but discretely, and is static for short periods of time. We have already seen that a negative β-parameter tends to flatten droplets out at the bottom, and also that dynamically varying evaporative flux tends to negate this effect by working against fluctuations in χ. This experimental comparison might be showing us that discretely changing evaporation is not enough to capture the behaviour at the end of drying, when the composition is usually changing the fastest and the droplet often has the most curvature.

The vapour simulation also does not account for the depth of the well – the droplet is thinnest near the edge, and sits below the surface of the substrate, where we have assumed the interface to be in the vapour-phase calculation. While we apply the lubrication approximation and assume the well is thin, we have also seen that small variations in composition can have a large effect on the evaporative flux and it is also possible that this discrepancy causes some error in calculating the evaporation. Unfortunately we currently do not have more experimental data with which to compare the theoretical model, as it is necessary to compare our model with pairs of liquids for which Raoult's Law is a good approximation. Divergence from Raoult's law is a consequence of non-ideal mixing, which we discussed in chapter 4 section 4.7.5.

5.10 Conclusion

In our penultimate chapter we have started to investigate the role that the gas above a DiW plays in its evaporation. Following in the footsteps of many other works, we made use of the large difference in relaxation timescale between the vapour and the droplet to argue that the system can, at any instant, be described by the Laplace equation. For a binary droplet, this model included an interface concentration boundary condition that was variable in time and space; for such a problem it was necessary to find a numerical solution instead of the analytical solution offered by studies that use constant and uniform concentration at the interface. We modified an existing finite element model so that it was able to solve the Laplace equation for any given distribution of two components in 3D cylindrical space and implemented it in the MoL algorithm for the droplet evaporation, using the concentration gradient at $Z = 0$ for the evaporative flux. The newly dynamic evaporative flux resulted in a droplet system with some self-correcting tendencies – as expected, large deviations in volume fraction create variations in evaporative flux that tend to oppose the compositional deviations.

We found that some groups of parameters were affected by the dynamic evaporation more than others. Notably, those droplets that exhibited a higher degree of curvature with static flux changed more under dynamic flux than those with less; and the droplet with the flattest bottom we simulated became susceptible to instabilities in its final moments of drying, leading us to lose trust in the model for particularly flat, late-stage DiWs. Because of this, and of the additional computation cost associated with dynamically varying the evaporative flux, we believe it is important to assess the need for a full two-sided DiW simulation before committing to one. The conditions under which we observe the numerical instability happen to coincide with the parameter range where dynamic-flux droplets are most similar to static-flux droplets, that is $\mathcal{C} \approx 2$, and also only appeared for $\alpha > 0.3$, $\beta <= -0.03$. For these reasons, we suggest that it makes sense, if the researcher requires very late-stage data ($> 97\%\, t_{\mathrm{td}}$), to use static evaporation when the experimental $\mathcal{C}$ parameter lies in the range $2 < \mathcal{C} < 5$, α is non-zero, and β is negative.

In the final chapter, we shall look at the case of a droplet that has been printed asymmetrically and use linear stability analysis to try to understand the rare – but nonetheless experimentally observed – phenomenon of an unstable asymmetrical droplet drying in a well.

Chapter 6

Stability of Asymmetrical Droplets

6.1 Non-Axisymmetric Droplets

In the DiW experiments, the droplet from the inkjet nozzle rarely lands exactly in the middle of the well and the droplet often overflows the edges of the well. In the vast majority of cases, the liquid relaxes back to an axisymmetric cap bounded at the edge of the well as the liquid evaporates. For certain values of alpha and beta, however, an asymmetry in the droplet is observed to grow with time. In rare cases it has also been observed that an initially symmetric droplet spontaneously develops an asymmetric profile. It is usually very difficult to investigate the process experimentally; the rate of volume loss is hard to calculate for a skewed droplet, and the droplet often overflows the well if the perturbation grows straight after printing. However, the perturbation does more rarely occur part way through the drying, figure 6.1. The origin of this phenomenon is not entirely known, but may be related to small imperfections in well manufacture. Examining the cross section, figure 6.2, reveals that the asymmetry begins just as the peak of the droplet passes through the plane of the top of the well and the interface starts to slip down the left hand side wall.

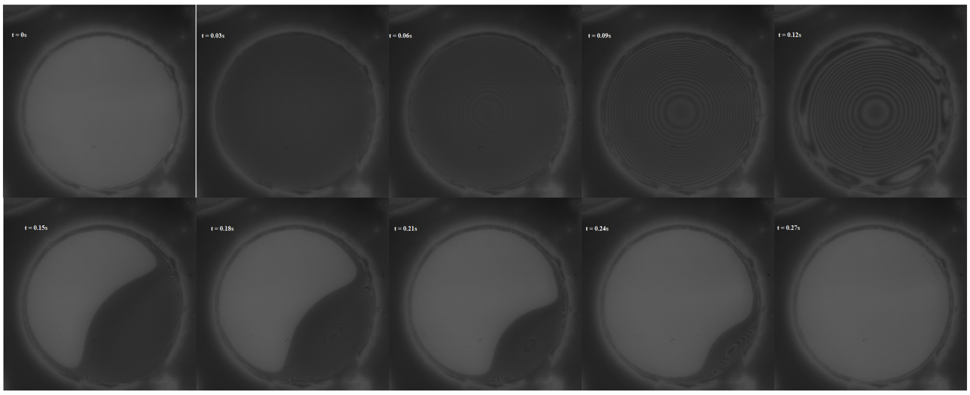

Figure 6.1: A DiW with an asymmetrical perturbation that emerges part way through the drying. Image courtesy of Zhida Huang.

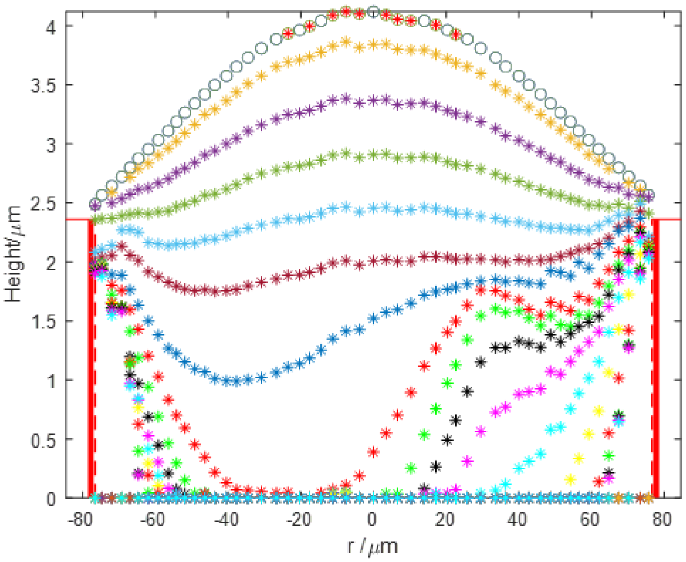

Figure 6.2: A cross section (one of many possible choices) of the DiW shown in figure 6.1. Image courtesy of Zhida Huang.

In order to investigate the stability conditions on the droplet we will perform a linear stability analysis (LSA) on the system equations. We shall start with an analysis of the two-dimensional binary problem introduced in chapter 4 (although we did not enter into much detail about it), because it is significantly simpler than the full three-dimensional cylindrical simulation and we would like to perform some numerical calculations. Later in this chapter we will state the analogous lubrication equations for a 3D non-axisymmetric droplet, but it will prove beyond the computational power of our machinery to perform the full simulation.
The following kind of linear stability analysis is used a number of other works on droplet and other thin films [138, 139, 140, 141, 142], but has not been performed on an evaporating DiW before. There are questions about whether some of the assumptions hold; while a flat-interface assumption is probably reasonable, given that we are operating within the lubrication approximation, the frozen-interface assumption (quasi-steady-state) may not hold when dealing with very volatile chemicals – their evaporation rate may be fast enough to contradict the imposition of a frozen interface. In this chapter we nonetheless intend to make some analytical progress under these assumptions to understand some of the overall features of instability in DiWs. We also hope to offer a mathematical starting point for future researchers to investigate full, three-dimensional DiW instability.

6.1.1 Two-Dimensional Cartesian Coordinates

Deriving Dispersion Relations

We first apply the quasi-steady-state approximation in order to assume that the growth rate of the perturbation is much faster than the evolution of the base state variables, h and χ. We freeze our solution at an instantaneous time, t_*, and perform the LSA on this frozen system. We also neglect spatial variation in the system, instead perturbing a uniform base state solution $\{h_b, \chi_b\}$. In our system, there is only one spatially uniform base state for the height profile that satisfies the boundary conditions: $h_b = 1$. We have freedom to choose any composition base state (we usually impose a uniform initial condition anyway), $\chi_b = \chi_0$. While spatial uniformity seems like a reductionist assumption, we are initially only searching for a qualitative description of droplet asymmetry behaviour – why are some system stable and others not?. The works cited above all make this assumption too; even though the majority of them apply a LSA to a thin film without the DiW boundary conditions, it will be informative to compare our results to theirs.

We then linearise the lubrication equations 4.44 and 4.45 about the base states at our frozen time $t = t_*$ with normal modes,

$$\tilde{h} = h_b + \delta_h e^{ikx - \omega t}\,, \tag{6.1}$$

$$\tilde{\chi} = \chi_b + \delta_\chi e^{ikx - \omega t}\,, \tag{6.2}$$

where we have applied a perturbation of wavelength k (a real number such that $k = \frac{n\pi}{2}$ in order to satisfy the boundary condition $h = 1$ at $x = 1$) and growth rate ω (in general a complex number). We search for the ω-k dispersion relation that emerges from the system when we substitute $\tilde{h}$ and $\tilde{\chi}$ into equation 4.29:

$$\omega(k) = \frac{\mathcal{C}}{3}k^4 - \frac{\delta_\chi}{\delta_h}\frac{\mathcal{M}}{2}k^2\,. \tag{6.3}$$

This parameter indicates whether a perturbation will grow or shrink by its sign – if it is positive the perturbation dies out, if it is negative the perturbation will grow. We present the dispersion relation in figure 6.3 for two values of the perturbation ratio, $\frac{\delta_h}{\delta_\chi}$. This reveals that capillary forces act to stabilise perturbations and are stronger for large wavenumbers, while Marangoni forces serve to drive the instability.

There is an equivalent dispersion relation that emerges from the composition equation,

$$\omega = \frac{k^2}{\mathrm{Pe}}\,, \tag{6.4}$$

which indicates that χ, through diffusion, always seeks to stabilise after a small perturbation.

Figure 6.3 also reveals the dependence of equation 6.3 on the perturbation ratio.

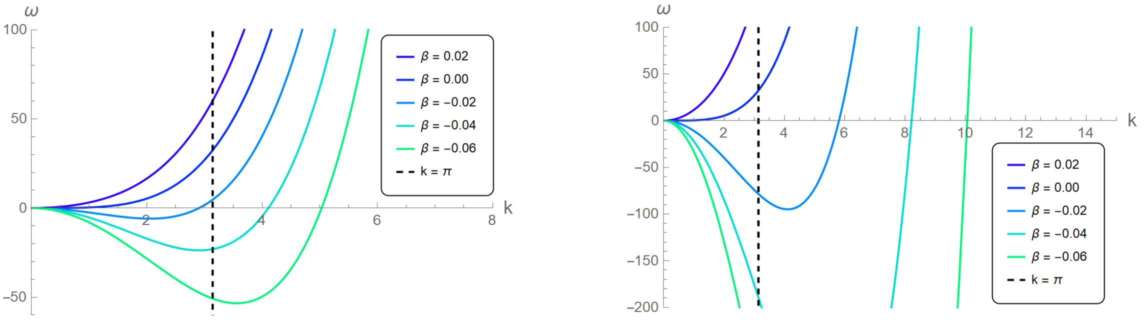

(a) $\frac{\delta_\chi}{\delta_h} = 0.05$

(b) $\frac{\delta_\chi}{\delta_h} = 0.2$

Figure 6.3: The dispersion relation (equation 6.3) for two different values of the ratio $\frac{\delta_\chi}{\delta_h}$. The dashed vertical line indicates where $k = \pi$, representing the smallest possible asymmetrical perturbation wavelength.

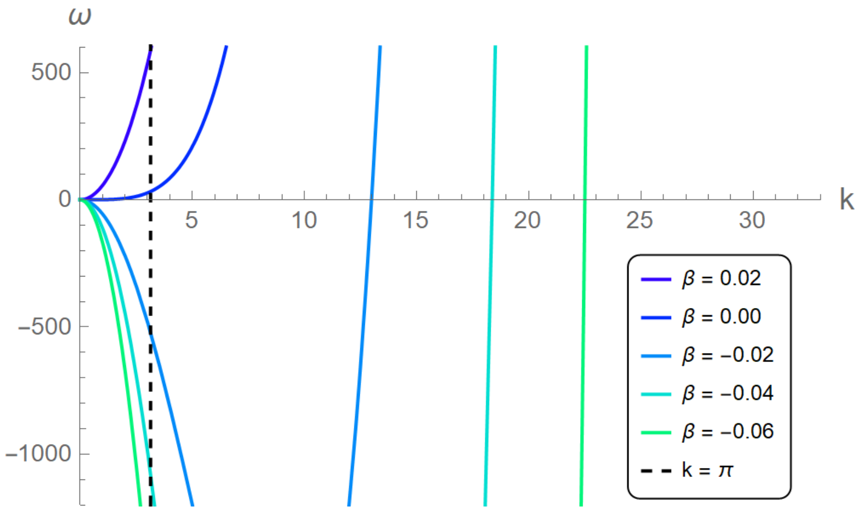

Figure 6.4: The dispersion relation with $\frac{\delta_\chi}{\delta_h} = 1$.

Of course, the assumption that we start at $h = 1$, $\chi = \chi_0$ and have no subsequent spatial variation in h is not generally useful: the experiments identify that asymmetrical perturbations can grow at a number of different points in the droplet evaporation, when the droplets shape is usually not flat. While we may be happy to approximate these with equation 6.3 (the droplet is indeed always thin, having a very small aspect ratio), there might also be situations in which we would prefer to obtain a more general and accurate description of asymmetrical instability in a DiW. This is especially true for analysing the stability of W-shaped droplets at later stages, when curvature plays a larger role in its evolution.

However, we encounter a problem if we try to do this. If we set the height base state $h_b = h_b(x)$ and work through the equivalent derivation we arrive at a contradictory expression for the dispersion relation, in which ω is a function not just of k, but also of x through h. This contradicts the original assumption that ω was solely dependant on k, by which we differentiated $h_b + \delta h$.

One possible way to analyse a non-flat droplet is to introduce a perturbation that itself varies spatially (in addition to its sinusoidal form):

$$\delta h = \delta_h f(x) e^{ikx-\omega t}, \tag{6.5}$$

where we seek a function $f(x)$ that cancels with the height base state to give a dispersion relation $\omega(k)$. If we start by perturbing the base state that corresponds to the initial parabolic shape of the droplet, the first term of the equation gives a dispersion relation

$$\begin{aligned}\mathfrak{Re}(\omega)(k) = \frac{\mathcal{C}}{3}\Bigg(3h_b^2\frac{\partial h_b}{\partial x}\bigg(\frac{d^3 f}{dx^3} - 3\frac{df}{dx}k^2\bigg)& \\ + h_b^3\bigg(-3\frac{d^2 f}{dx^2}k^2 + fk^4\bigg)& \\ + h_b^3\bigg(\frac{d^4 f}{dx^4} - 3\frac{d^2 f}{dx^2}k^2\bigg)\Bigg)&. \end{aligned} \tag{6.6}$$

We can immediately see that this approach will be fruitless – there is no function

$f(x)$ that will cancel with $h_b(x)$ such that we may obtain the desired dispersion relation. However, we can set $h_b = f = 1$ and retrieve the first term of equation 6.3. Another possible approach is to express the base state and the perturbation as Fourier series and plug them into the lubrication equations. We make use of the known result for x^2,

$$x^2 = \frac{2}{3} + \frac{4}{\pi^2} \sum_{n=1}^{\infty} \frac{(-1)^n}{n^2} \cos(n\pi x)\,, \tag{6.7}$$

and write the perturbation as

$$\delta h = \sum_{m=0}^{\infty} \delta_m \sin(m\pi x) e^{-\omega_m t}\,. \tag{6.8}$$

Inserting these expressions into the first term of equation 4.44 gives

$$\begin{aligned}
&\sum_{m=0}^{\infty} \frac{-\delta_m \omega_m}{2i} (e^{im\pi x} - e^{-im\pi x}) e^{-\omega_m t} = \\
&\qquad -\frac{(1-a)^3}{\pi^2} \Bigg[3\Big(\sum_{n=1}^{\infty} \frac{(-1)^n i}{n} (e^{in\pi x} - e^{-in\pi x}) \Big) \cdot \\
&\qquad\qquad \Big(\sum_{n=1}^{\infty} \frac{(-1)^n}{n} (e^{in\pi x} + e^{-in\pi x}) \Big)^2 \cdot \\
&\qquad\qquad \Big(\sum_{n=1}^{\infty} \delta_n n^3 (e^{in\pi x} + e^{-in\pi x}) e^{-\omega_n t} \Big) \\
&\qquad\qquad + 16 \Big(\sum_{n=1}^{\infty} \frac{(-1)^n i}{n^2} (e^{in\pi x} + e^{-in\pi x}) \Big)^3 \cdot \\
&\qquad\qquad\qquad \Big(\sum_{n=1}^{\infty} \delta_n n^4 i (e^{in\pi x} - e^{-in\pi x}) e^{-\omega_n t} \Big) \Bigg]\,,
\end{aligned} \tag{6.9}$$

In theory, we could find an expression for the real part of the growth parameter of each mode, ω_n, such that the spatial variation from x cancels out. In the analysis in this chapter, we consider it enough to use the simpler expression that assumes a flat film, equations 6.3 and 6.4. For the purpose of this thesis, we simply want to understand why some systems develop asymmetry and we are not attempting to match growth rates quantitatively; we will see that these equations can offer some insight into the qualitative asymmetrical instability behaviour of simple, 2D DiWs.

Short-Time Simulation

We can underline equations 6.3 and 6.4 with some simulations; we start with those in figure 6.5, which have a uniform initial height and composition profile with a small sinusoidal perturbation,

$$\delta h = \delta \chi = -\delta \sin(\pi x)\,. \tag{6.10}$$

We then run the usual simulation, without evaporation, for a short time. Of course, strictly speaking, the dispersion relation no longer applies once we have a large perturbation, or one that evolves away from a perfect sine curve; we will indeed see this behaviour, even after short time. The simulations are only intended to give us an indication of the validity of our derived dispersion relations. In this section, we use red curves to symbolise the initial perturbed state, yellow–orange for an intermediate step, and blue for the final curve that we consider (e.g. the flat interface in figure 6.5a).

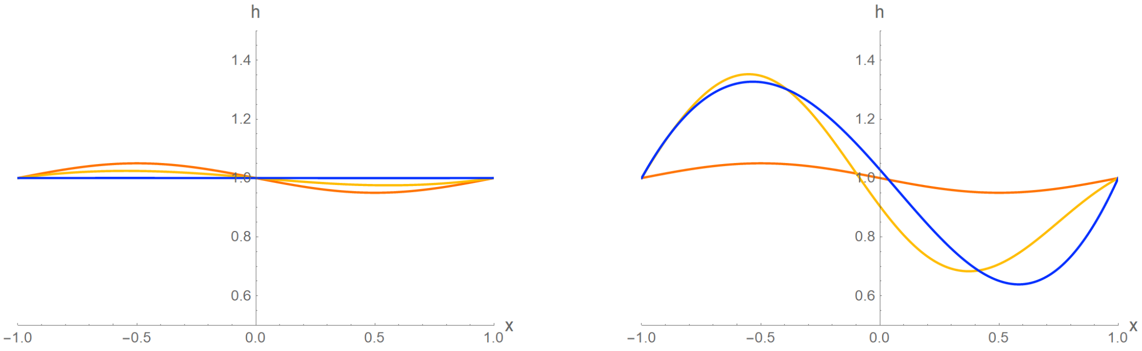

(a) $\beta = 0$ (b) $\beta = -0.06$

Figure 6.5: Short-time evolution of the uniform base state under a perturbation for two values of β. Having a negative value of β drives the imposed instability over the short period of time.

It is clear from figure 6.5 that, while a droplet without Marangoni forces equilibrates quickly to the flat base state, the perturbation in a binary droplet with a large surface tension difference grows.

We might be surprised to see the droplet's asymmetry[1] become asymmetrical and no longer pass through the point (0, 1), especially given that $\frac{\partial h}{\partial t}$ is a symmetrical PDE. This phenomenon is likely caused by the evolution of the composition variable, whose evolution equation (equation 4.44) contains a term in $\frac{1}{h}$. This term will lead to an asymmetrical evolution of the composition because the perturbation in h is odd around the z-axis.

The short-time evolution of the composition is presented in figure 6.6. We see that the perturbation shrinks in both cases, as predicted by equation 6.4, and the system with Marangoni effects briefly exhibits an off-central perturbation (thanks to the $\frac{1}{h}$ term in the equation).

---

[1] for the avoidance of ambiguity, we should refer to this as odd-function symmetry. Figure 6.5b depicts a sinusoidal, odd, but technically symmetrical function that evolves into a truly asymmetrical function

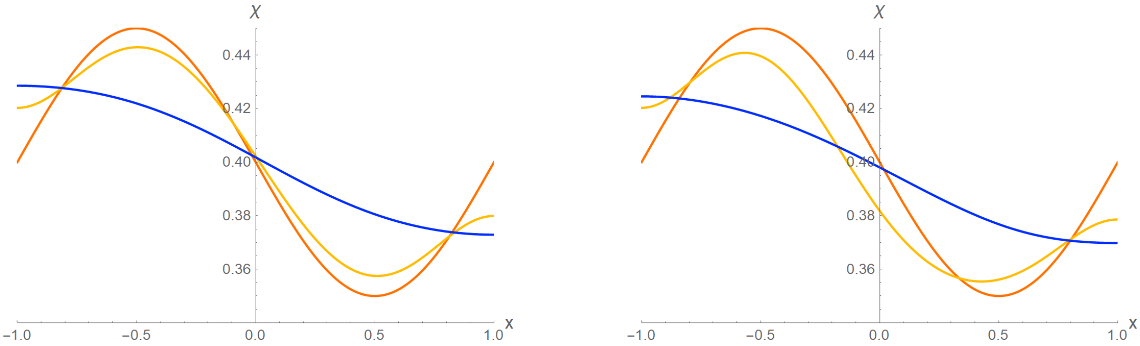

(a) $\beta = 0$ (b) $\beta = -0.06$

Figure 6.6: Short-time evolution of the composition. Here Marangoni forces do not have a large effect on the evolution of the perturbation in the composition; in both cases the perturbation tends to decrease over the short time period.

There is some slightly unexpected behaviour in the case of positive β, shown in figure 6.7. The prediction in equation 6.3 is initially fulfilled and the perturbation shrinks. However, it subsequently inverts and begins to grow, despite the composition variable continuing to die out. We can understand the growth after the sign inversion by noticing that the ratio $\frac{\delta_\chi}{\delta_h}$ becomes negative and therefore $\omega < 0$, but what about the origin of the inversion itself? When β is positive, the surface tension is proportional to $-\chi$, meaning liquid will be drawn away from regions of large χ. We can see this by comparing figures 6.7a and 6.7b – where χ is largest, h is depleted, and where χ is smallest, h increases.

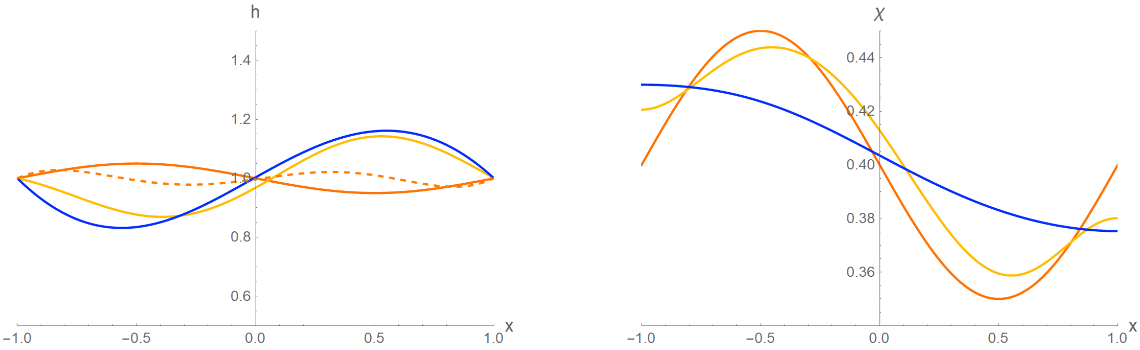

(a) height (b) composition

Figure 6.7: Short-time evolution of the height and composition of a droplet with $\beta = 0.03$. The dotted curve represents an instant in which the perturbed interface has become deflected to equilibrium at some places (near the centre) and has remained perturbed at others (near the edge). Positive values of β appear to invert the perturbation of the interface eventually, due to the interaction with the perturbed composition.

We can conclude, then, that equations 6.3 and 6.4 describe the instantaneous behaviour of uniform base states accurately and give insight into the evolution of perturbations over a short timescale. While this analysis clearly cannot describe the asymmetry observed in some experiments quantitatively, it does indicate that a critical factor in studying these unstable droplets is the Marangoni effect and the magnitude of parameter $\mathcal{M}$. For future investigation, it would be desirable to properly compare simulation with experiment to determine the quantitative interaction of the Marangoni effect and asymmetrical instability. For this, we would need a set of experimental results and a fully three-dimensional model of the system.

6.1.2 Three-Dimensional Cylindrical Coordinates

A fully three-dimensional cylindrical treatment of the DiW system gives rise to equations that depend on the azimuthal coordinate θ. Using the same derivation method as in chapter 3, we arrive at

$$\frac{\partial h}{\partial t} = -\frac{1}{r}\Big(\frac{\partial}{\partial r}[rh\bar{u}] + \frac{\partial}{\partial \theta}[h\bar{v}]\Big) - \frac{1}{\sqrt{1-r^2}} \tag{6.11}$$

and

$$\begin{aligned}\frac{\partial \chi}{\partial t} = -\bar{u}\frac{\partial \chi}{\partial r} - \bar{v}\frac{\partial \chi}{\partial \theta}& \\ + \frac{1}{\mathrm{Pe}}\Big(\frac{1}{r}\frac{\partial}{\partial r}\Big[r\frac{\partial \chi}{\partial r}\Big] + \frac{1}{h}\frac{\partial h}{\partial r}\frac{\partial \chi}{\partial r} + \frac{1}{r^2}\frac{\partial^2 \chi}{\partial \theta^2} + \frac{1}{hr^2}\frac{\partial h}{\partial \theta}\frac{\partial \chi}{\partial \theta}\Big)& \\ + \frac{\alpha\chi(1-\chi)}{h\sqrt{1-r^2}}\,,&\end{aligned} \tag{6.12}$$

where the radial and azimuthal velocities are given by

$$u = -\mathcal{C}\Big(\frac{\partial}{\partial r}\Big[\frac{1}{r}\frac{\partial}{\partial r}\Big[r\frac{\partial h}{\partial r}\Big]\Big] + \frac{\partial}{\partial r}\Big[\frac{1}{r^2}\frac{\partial^2 h}{\partial \theta^2}\Big]\Big)\Big(\frac{1}{2}z^2 - hz\Big) + \frac{\mathcal{M}}{2}\frac{\partial \chi}{\partial r}z \tag{6.13}$$

and

$$v = -\mathcal{C}\Big(\frac{1}{r}\frac{\partial^2}{\partial \theta \partial r}\Big[r\frac{\partial h}{\partial r}\Big] + \frac{1}{r^2}\frac{\partial^3 h}{\partial \theta^3}\Big)\Big(\frac{1}{2}z^2 - hz\Big) + \frac{\mathcal{M}}{2r}\frac{\partial \chi}{\partial \theta}z\,, \tag{6.14}$$

and the bar indicates that they are averaged over the droplet height.
We might conceive of initialising the 3D droplet as per figure 6.8, whose interface has the form

$$h_{\mathrm{asym}}(r,\theta) = a + (1-a)r^2 + \delta\, r(r-1)\cos(\theta)\,. \tag{6.15}$$

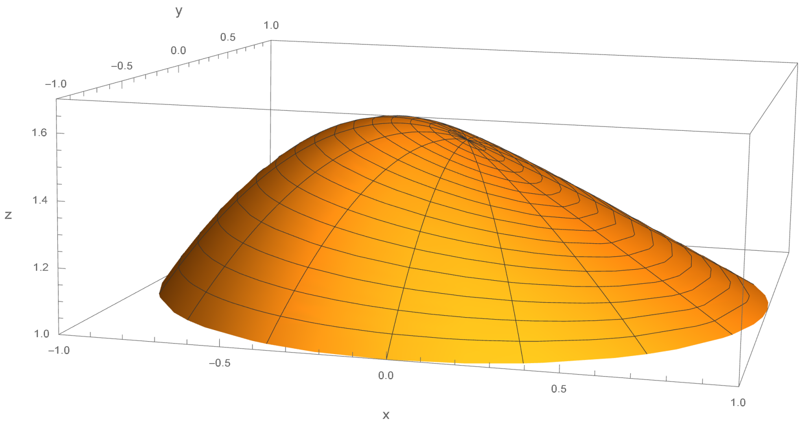

Figure 6.8: One possible initial condition of the perturbed 3D droplet. Perturbation is exaggerated for visibility.

A full 3D simulation would be the logical next step for an analysis into the evolution of asymmetrical DiWs, but is beyond the scope of this project.

6.2 Conclusion

In our final chapter we have examined the properties of the DiW system under the inclusion of small perturbations to both the height and composition variables. Using a linear stability analysis on a uniform base state, we were able to derive a dispersion relation between the growth rate and wavenumber of a sinusoidal perturbation that, critically, depends on the capillary and Marangoni numbers of the DiW system. We tested the perturbation's growth/death condition using a short-time simulation on a flat DiW with a single-wavelength sinusoidal perturbation and found that our model's predictions were accurate: droplets with no Marangoni forces equilibrated back to uniformity; droplets with negative β exhibited initial destabilisation which slowed as the composition re-equilibrated; and those with positive β initially flattened, only for the perturbation to invert and subsequently grow.

This model comprises a starting point for future investigation into the instability of asymmetrical/non-axisymmetrical DiWs, which would require a fully 3D model and simulation. We ended this chapter by suggesting such a model, which now depends on the azimuthal coordinate θ.

Chapter 7

Conclusion

In this thesis, we have conducted a theoretical and numerical investigation into the evaporation of a tiny droplet from a well. We have simulated the physics of pure droplets, binary droplets, and the vapour concentration field to study a range of important properties of these droplets in a well (DiWs), including the shape of the droplet-gas interface as it dries, the flow field inside the droplet, and its complex behaviour under Marangoni forces and a viscosity that changes with composition distribution.

We established our central research questions in chapter 1: we wanted to construct a model for a DiW that could probe the coffee-ring effect, noticing that there were no complete mathematical models for this problem that accounted for large variation in the capillary number. We wondered to what extent it would be possible to model conditions under which the coffee-ringe effect (CRE) may be suppressed in both pure and binary droplets, composed of different liquids and printed in a well of different sizes. And, moving away from industrial application, we simply asked whether we would be able to replicate experimental results; could we generate qualitatively, or even quantitatively, accurate interface shapes compared to our colleagues' results in the lab.

7.1 Conclusions

Chapter 3 focused on pure DiWs and the derivation of a lubrication model to simulate their evolution. The main result from this chapter was the appearance of three distinct regions of parameter $\mathcal{C}$, in which we saw the droplet assume a W-, U-, or C-shaped profile; we successfully built a model and simulation that was capable of reproducing generic, qualitative properties of simple droplets observed in experiments. Furthermore, we were able to match our model to experimental results (the correlation only weakening towards the extreme outer edge of the droplet), proving that the shapes we can produce are real and observable in experiment; while there is some discrepancy in the quantitative agreement between experimental and theoretical values of $\mathcal{C}$, we are nonetheless confident in the qualitative ability of our model to predict complex droplet surface morphology.

In chapter 2, we saw that one of the key predictors of deposit shape in a well was the droplet shape at touchdown; Vlasko-Vlasov *et al.*'s paper [38] showed that the sticking and slipping of the inner contact line (that is, the touchdown point) left a deposit of concentric rings. We are confident, then, that our model is able to inform the general conditions by which one might avoid these kinds of deposits in a pixel – conditions that favour W-shapes are likely to produce stronger ring patters than those that favour U- or C-shapes, which are more likely to result in central disk deposits.

It is not only the droplet shape that gives us information on the final deposit, however. We saw, in works from Li *et al.* and Ooi *et al.* [45, 17], that flow velocity also plays a role, the CRE being associated with large flow speeds near the edge of the droplet, particularly towards the end of the drying. Our model is able to reveal the velocity field of the DiW across all values of $\mathcal{C}$; it can show the conditions under which we see examples of faster radial flows early in the drying and rush-hour effects late in the drying.

Chapter 4 moved past the simple pure droplet to extend the model to binary droplets. We first introduced two new parameters, α and β, to represent the evaporation and surface tension differences between the two components; now we had a model with three degrees of freedom. In this chapter we examined the effects of varying these three parameters on the interface shape and velocity field in order to catalogue a broader range of combinations of conditions for controlling the deposit. We compared our simulation results to experimental data again, having similar qualitative success with the overall shape as in the pure droplet case.

Recalling Hu and Larson's extensive research on the Marangoni effect in sessile droplets [7, 68], we were pleased to mirror their general CRE suppression result (theirs obtained by finite element analysis (FEA), ours by method of lines (MoL)) – we succeeded in transforming a W-shaped DiW into a flat-bottomed one by including surface tension gradients that drew liquid from the centre of the droplet to the edge. There is some small hole in the literature at this point – out of a desire to eliminate the CRE for important and valid industrial purposes, the field has largely overlooked the inverse effect. The Marangoni effect does not ubiquitously act to suppress ring stains, because it is represented by a signed quantity. We found that flipping the sign of β led to an opposite effect wherein W-shape droplets had their curvature enhanced, by proxy supporting the CRE. Of course, this is simple to achieve in theoretical research and somewhat more difficult in experimental work, but we believe that a complete understanding (both mathematical and practical) of the Marangoni effect in DiWs will not emerge until we grapple with Marangoni flows that suppress *and* enhance CRE-type behaviour.

Another feature of the Marangoni effect we discussed in the literature review is the recirculating flow; in fact it is often held largely responsible for suppression of the CRE. Our model was able to predict the emergence of regions where the flow turned inwards, showing that for some range of parameters they disappear and for others they are present. Although we only observed full recirculation for a small range of the parameter space (namely, large $\mathcal{C}$ and negative β), all DiWs with $\mathcal{C} > 0.1$ contained regions where the flow was directed towards the centre.

In chapter 4, we encountered, quite by accident, the phenomenon of a dimpled solution in the limiting case of $\alpha \to 0$, i.e. when one component is involatile. Indeed, we advanced our model to include scenarios in which one component is much more viscous than the other, discovering that the magnitude of the variation in viscosity had a large influence on the location of touchdown. Specifically, the greater the viscosity of the less volatile component, the further from the centre the droplet touched down. This represents another oversight in the small body of literature on DiWs (especially binary ones); we mentioned that dimpled solutions in lubrication-limited systems are found in closely related fields [127, 128, 129, 130, 131], but not specifically in work on droplets or DiWs, despite the fact that such a phenomenon may be useful industrially and conceptually in understanding the behaviour of droplet deposits, as we discussed in this chapter.

Chapter 5 was motivated by an acknowledgement that the evaporative flux of the two components in a binary droplet could not, in general, be described accurately by the simple Popov form we had previously been using. We built a two-sided simulation of a three-dimensional, axisymmetric droplet; while it was not possible to solve this model analytically, we constructed a FEM simulation that tracked the evolution of the vapour field as the droplet dried. We demonstrated its accuracy by reproducing Popov's form of the flux [13] that diverges at the contact line.

We proceeded to compare what we called static- and dynamic-flux simulations, the former in which we used the Popov form throughout and the latter in which we updated the flux every time a specific condition was met. Dynamic flux tended to act against the effects we had observed in chapter 4; that is, the evaporative flux increased and decreased according to the locations of peaks and troughs respectively, causing them to be less pronounced over the course of the drying. While the overall impact of the solutal Marangoni effect was not negated, it was certainly suppressed. This Marangoni suppression was larger for different values of the parameters; for $\mathcal{C} \approx 2$, for example, it was much smaller than for the other values we tested. This indicates that a full dynamic-flux simulation (which is quite computationally expensive) may not be necessary to model DiWs over the whole parameter space – for certain droplet/well combinations it would be acceptable (depending on precision requirements) to revert to a static-flux simulation.

From the small dataset at our disposal, we were able to fit a simulation to experimental data with parameters much closer to those provided from the experiment. It was very accurate near the centre of the droplet and also in the early and mid-stages of drying, only losing accuracy towards the end and near the edge. We are confident that this dynamic-flux model could be refined through access to a larger set of experimental data to further test the idea that including dynamic flux increases the model's accuracy at predicting some DiWs.

Finally, inspired by a chance observation in the lab, we spent chapter 6 briefly exploring the instability dynamics of a droplet that prints asymmetrically. We used a linear stability analysis to determine the conditions under which a droplet in a 2D square well might become asymmetrically unstable, concluding that the Marangoni term in the height lubrication equation was responsible for asymmetrical growth, in accordance with others who have studied the instability of thin films [142]. We went on to show that the dispersion relations can predict the asymmetry behaviour of 2D DiWs that are initialised with a perturbation by analysing some short-time simulations.

7.2 Drawbacks and Future Research

There is much room for future work in the field of evaporating pure and binary DiWs. Primarily, this work is limited by the small body of experimental data with which to compare a theoretical model, particularly for binary DiWs. The main drawback of this project is that consistent quantitative agreement with the current selection of data sets is elusive – as long as a discrepancy between experimental and theoretical values of $\mathcal{C}$ exists, a fully predictive model will be out of reach. The elephant in the room for this project in particular is the COVID-19 pandemic, the social restrictions for which started in March 2020 in the UK. Because of its nature as a theoretical and numerical thesis, this project has not been affected to the same extent as those that are lab-based, however the main limitations it has suffered are precisely *because* the laboratory work was suspended for such a long time. Although we were able to analyse and compare with the small range of data on pure droplets that already existed, experimental work on binary droplets was paused.

Due to the complexity of the three-dimensional parameter space, and with the intention of eliminating the experimental–theoretical discrepancy in these values, we consider that a more rigorous data fitting procedure ought to be adopted for future analysis. In chapter 4 we described a fitting method that started with the experimental values of parameter and slowly changed them until we obtained a visual match. An example of a much better method would be to train a neural network to understand the parameter space (it could learn on a set of simulated curves, varying parameters $\mathcal{C}$, α, β, χ_0, a, Pe, and the sampled time points) and predict the theoretical values of $\mathcal{C}$, α, and β that correspond to experimental data.

Secondarily, there remains work to be done on the direct link between a DiW surface profile and the material deposit. While we know, as we have stated at multiple points in this report, that W-shaped profiles lead to strong coffee rings (with a mound in the middle too, once the dimple evaporates) and U-shapes with lower radial flow create more uniform deposits, for the theoretician there is still some hand-waving and guesswork in this process. For example, we are unable to offer a numerical relationship between the interface shape (for example, quantifying the curvature at the touchdown point) and the density of a given solid deposit; although we are confident the argument is qualitatively correct, more study is necessary on the mechanisms that provoke the CRE in DiWs. A strength of our method is the ability to set $\alpha = 1$ and study a system in which one component is involatile. Because we can point to the final shape (before the second, non-evaporative relaxation stage) as an indicator of the deposit depth, we believe it would be worthwhile to investigate this limit further.

Another drawback of this project is that it is limited to only consider relatively simple scenarios; for example, we only give a treatment of binary droplets and do not advance to tertiary ones. In this respect, our project offers a basic fundamental model that could be built upon for future research into the dynamics of DiWs: including multiple chemical components beyond just two; exploring the full effect of polymer viscosity on dimpled solutions; and more thoroughly analysing the impact of dynamic flux.

Including further chemical components would, of course, prove an additional challenge to future researchers; many of the assumptions we have made in the model in this work would break down if we were to move to a tertiary system. For example, we have consistently assumed ideal mixing, which is already one assumption too far for some binary systems – how much more for triple-component droplets. We have also neglected thermal Marangoni effects, an assumption that is unlikely to hold for much more complicated droplets. Therefore many assumption made in this thesis may have to be reevaluated before moving to tertiary systems.

We also acknowledge that we were unable to locate the source of the sinusoidal numerical instability that arose at the end of the drying for a small range of $\mathcal{C}$ values. The wave pattern assumed by the evaporative flux, although detrimental to the quality of the simulation, is an intriguing occurrence and we are sure finding its origin would have led to a deeper understanding of the two-sided DiW system.

Finally, there remains the interesting problem of the asymmetrically unstable droplets. While we made progress in understanding the forces that drive and restrain asymmetry in a DiW, our analysis was limited to a 2D square well and approximated with a flat interface. In order to understand the origins of non-axisymmetric interfaces in DiWs fully, we need a three-dimensional (r, θ, z) model that solves the two lubrication equations and a set of experimental results to compare with.

7.3 Final Reflections

We have come a long way, then, from watching paint dry, spilling espressos on tables, and finding excuses to have another glass of wine at a wedding. If my conversation partners from chapter 1 are still with me after 20 minutes or so, a final question often signals the end of their brief foray into science: “so, how is all this going to change the world?” There is always a risk at this stage of either over- or underselling the impact of the thesis and its contribution to our understanding of the universe. However, I enjoy articulating something about the beauty of a simple mathematical model that describes a niche part of the world. We started with a single equation and a single dimensionless parameter that was capable of qualitative and quantitative imitation of pure droplets drying in wells. And even when we advanced the model with new parameters and a new equation for binary droplets, we discovered interesting and unexpected behaviour that helps us to understand the physics of more complex systems: mixtures of chemicals whose surface tensions create new flows; the relevance of a dynamically changing evaporative flux; and the conditions under which our droplets become wonky and even overflow.

As for technological implications, I would also mention that my project, along with the experimental work performed by Zhida Huang and Teresa Colosimo, has made progress in designing fluids that give uniform deposits when drying in pixels. My interrogator may not notice the direct impact on her next iPhone, but between the experimental and theoretical contributions of this work and others, we are well on the way towards a more efficient manufacturing process for organic light emitting diode displays.

After our conversation, I usually leave hoping that I have been able to inspire a stir of excitement about the study and science of small and seemingly insignificant parts of the world; I hope that the reader has also enjoyed our journey through the world of droplets drying in wells.

Bibliography

[1] Adam D Eales, Nick Dartnell, Simon Goddard, and Alexander F Routh. The impact of trough geometry on film shape. a theoretical study of droplets containing polymer, for p-oled display applications. *Journal of Colloid and Interface Science*, 458:53–61, 2015.

[2] Jan Schlottke and Bernhard Weigand. Direct numerical simulation of evaporating droplets. *Journal of Computational Physics*, 227(10):5215–5237, 2008.

[3] Hannah-May D'ambrosio, Teresa Colosimo, Brian R Duffy, Stephen K Wilson, Lisong Yang, Colin D Bain, and Daniel E Walker. Evaporation of a thin droplet in a shallow well: theory and experiment. *Journal of Fluid Mechanics*, 927, 2021.

[4] Robert D Deegan, Olgica Bakajin, Todd F Dupont, Greb Huber, Sidney R Nagel, and Thomas A Witten. Capillary flow as the cause of ring stains from dried liquid drops. *Nature*, 389(6653):827–829, 1997.

[5] Daniel Walker, Hamish Leith, Lisa Duff, Li Wei Tan, Hsin-Rong Tseng, Thorsten Schenk, and Peter Levermore. High resolution ink-jet printed oled for display applications. In *NIP & Digital Fabrication Conference*, volume 2016, pages 469–471. Society for Imaging Science and Technology, 2016.

[6] JB Fournier and AM Cazabat. Tears of wine. *EPL (Europhysics Letters)*, 20(6):517, 1992.

[7] Hua Hu and Ronald G Larson. Marangoni effect reverses coffee-ring depositions. *The Journal of Physical Chemistry B*, 110(14):7090–7094, 2006.

[8] WD Ristenpart, PG Kim, C Domingues, J Wan, and Howard A Stone. Influence of substrate conductivity on circulation reversal in evaporating drops. *Physical review letters*, 99(23):234502, 2007.

[9] Hua Hu and Ronald G Larson. Evaporation of a sessile droplet on a substrate. *The Journal of Physical Chemistry B*, 106(6):1334–1344, 2002.

[10] Manouk Abkarian, Janine Nunes, and Howard A Stone. Colloidal crystallization and banding in a cylindrical geometry. *Journal of the American Chemical Society*, 126(19):5978–5979, 2004.

[11] Emmanuelle Rio, Adrian Daerr, François Lequeux, and Laurent Limat. Moving contact lines of a colloidal suspension in the presence of drying. *Langmuir*, 22(7):3186–3191, 2006.

[12] Robert D Deegan, Olgica Bakajin, Todd F Dupont, Greg Huber, Sidney R Nagel, and Thomas A Witten. Contact line deposits in an evaporating drop. *Physical review E*, 62(1):756, 2000.

[13] Yuri O Popov. Evaporative deposition patterns: spatial dimensions of the deposit. *Physical Review E*, 71(3):036313, 2005.

[14] Benjamin J Fischer. Particle convection in an evaporating colloidal droplet. *Langmuir*, 18(1):60–67, 2002.

[15] Jens Eggers and Len M Pismen. Nonlocal description of evaporating drops. *Physics of Fluids*, 22(11):112101, 2010.

[16] Eric Sultan, Arezki Boudaoud, and Martine Ben Amar. Diffusion-limited evaporation of thin polar liquid films. *Journal of engineering mathematics*, 50(2):209–222, 2004.

[17] Yuto Ooi, Itsuo Hanasaki, Daiki Mizumura, and Yu Matsuda. Suppressing the coffee-ring effect of colloidal droplets by dispersed cellulose nanofibers. *Science and Technology of Advanced Materials*, 18(1):316–324, 2017.

[18] Christian Diddens, Yaxing Li, and Detlef Lohse. Competing marangoni and rayleigh convection in evaporating binary droplets. *Journal of Fluid Mechanics*, 914, 2021.

[19] Lennert R van den Doel and Lucas J van Vliet. Temporal phase-unwrapping algorithm for dynamic interference pattern analysis in interference-contrast microscopy. *Applied optics*, 40(25):4487–4500, 2001.

[20] B Rieger, LR Van den Doel, and LJ Van Vliet. Ring formation in nanoliter cups: Quantitative measurements of flow in micromachined wells. *Physical Review E*, 68(3):036312, 2003.

[21] Chin-Tai Chen, Ching-Chang Chieng, and Fan-Gang Tseng. Uniform solute deposition of evaporable droplet in nanoliter wells. *Journal of Microelectromechanical Systems*, 16(5):1209–1218, 2007.

[22] Youngki Jung, Tadashi Kajiya, Tatsuya Yamaue, and Masao Doi. Film formation kinetics in the drying process of polymer solution enclosed by bank. *Japanese Journal of Applied Physics*, 48(3R):031502, 2009.

[23] Tadashi Kajiya, Wataru Kobayashi, Tohru Okuzono, and Masao Doi. Controlling the drying and film formation processes of polymer solution droplets with addition of small amount of surfactants. *The Journal of Physical Chemistry B*, 113(47):15460–15466, 2009.

[24] Tohru Okuzono, Masaru Kobayashi, and Masao Doi. Final shape of a drying thin film. *Physical Review E*, 80(2):021603, 2009.

[25] Yu Tarasevich, IV Vodolazskaya, OP Isakova, Abdel Latif, et al. Evaporation-induced flow inside circular wells: analytical results and simulations. *Microgravity Science and Technology*, 21(1):39–44, 2009.

[26] Henning Sirringhaus and Tatsuya Shimoda. Inkjet printing of functional materials. *MRS bulletin*, 28(11):802–806, 2003.

[27] Haibin Zhu, Weijie Wang, Fengjie Zhang, Xin Jin, Xiaohu Li, Xinxing Wang, Bin Zhang, and Guangcai Yuan. 47-4: Effects of fine-metal-mask wrinkling on oled patterning defects. In *SID Symposium Digest of Technical Papers*, volume 49, pages 627–629. Wiley Online Library, 2018.

[28] Madhusudan Singh, Hanna M Haverinen, Parul Dhagat, and Ghassan E Jabbour. Inkjet printing—process and its applications. *Advanced materials*, 22(6):673–685, 2010.

[29] Peter Levermore, Thorsten Schenk, Hsin-Rong Tseng, Hsing-Ju Wang, Holger Heil, Anja Jatsch, Herwig Buchholz, and Edgar Böhm. 38-1: Invited paper: Ink-jet-printed oleds for display applications. In *SID Symposium Digest of Technical Papers*, volume 47, pages 484–486. Wiley Online Library, 2016.

[30] B-J De Gans, Paul C Duineveld, and Ulrich S Schubert. Inkjet printing of polymers: state of the art and future developments. *Advanced materials*, 16(3):203–213, 2004.

[31] Jing Shi, Lisong Yang, and Colin D Bain. Drying of ethanol/water droplets containing silica nanoparticles. *ACS applied materials & interfaces*, 11(15):14275–14285, 2019.

[32] Emma L Talbot, Lisong Yang, Arganthaël Berson, and Colin D Bain. Control of the particle distribution in inkjet printing through an evaporation-driven sol–gel transition. *ACS applied materials & interfaces*, 6(12):9572–9583, 2014.

[33] Alexander Oron, Stephen H Davis, and S George Bankoff. Long-scale evolution of thin liquid films. *Reviews of modern physics*, 69(3):931, 1997.

[34] Osborne Reynolds. Iv. on the theory of lubrication and its application to mr. beauchamp tower's experiments, including an experimental determination of the viscosity of olive oil. *Philosophical transactions of the Royal Society of London*, (177):157–234, 1886.

[35] S Maenosono, CD Dushkin, S Saita, and Y Yamaguchi. Growth of a semiconductor nanoparticle ring during the drying of a suspension droplet. *Langmuir*, 15(4):957–965, 1999.

[36] Robert D Deegan. Pattern formation in drying drops. *Physical review E*, 61(1):475, 2000.

[37] Chin-Tai Chen, Fan-Gang Tseng, and Ching-Chang Chieng. Evaporation evolution of volatile liquid droplets in nanoliter wells. *Sensors and Actuators A: Physical*, 130:12–19, 2006.

[38] VK Vlasko-Vlasov, M Sulwer, EV Shevchenko, J Parker, and WK Kwok. Ring patterns generated by an expanding colloidal meniscus. *Physical Review E*, 102(5):052608, 2020.

[39] Adam D Eales, Alexander F Routh, Nick Dartnell, and Goddard Simon. Evaporation of pinned droplets containing polymer–an examination of the important groups controlling final shape. *AIChE Journal*, 61(5):1759–1767, 2015.

[40] AD Eales, N Dartnell, S Goddard, and Alexander Francis Routh. Thin, binary liquid droplets, containing polymer: an investigation of the parameters controlling film shape. *Journal of Fluid Mechanics*, 794:200–232, 2016.

[41] Yaxing Li, Christian Diddens, Pengyu Lv, Herman Wijshoff, Michel Versluis, and Detlef Lohse. Gravitational effect in evaporating binary microdroplets. *Physical review letters*, 122(11):114501, 2019.

[42] AMJ Edwards, PS Atkinson, CS Cheung, H Liang, DJ Fairhurst, and FF Ouali. Density-driven flows in evaporating binary liquid droplets. *Physical review letters*, 121(18):184501, 2018.

[43] Alvaro G Marin, Hanneke Gelderblom, Detlef Lohse, and Jacco H Snoeijer. Order-to-disorder transition in ring-shaped colloidal stains. *Physical review letters*, 107(8):085502, 2011.

[44] Álvaro G Marín, Hanneke Gelderblom, Detlef Lohse, and Jacco H Snoeijer. Rush-hour in evaporating coffee drops. *Physics of fluids*, 23(9):091111, 2011.

[45] Yaxing Li, Christian Diddens, Tim Segers, Herman Wijshoff, Michel Versluis, and Detlef Lohse. Evaporating droplets on oil-wetted surfaces: Suppression of the coffee-stain effect. *Proceedings of the National Academy of Sciences*, 117(29):16756–16763, 2020.

[46] GJ Dunn, SK Wilson, BR Duffy, S David, and Khellil Sefiane. A mathematical model for the evaporation of a thin sessile liquid droplet: Comparison between experiment and theory. *Colloids and Surfaces A: Physicochemical and Engineering Aspects*, 323(1-3):50–55, 2008.

[47] Rajneesh Bhardwaj, Xiaohua Fang, and Daniel Attinger. Pattern formation during the evaporation of a colloidal nanoliter drop: a numerical and experimental study. *New Journal of Physics*, 11(7):075020, 2009.

[48] Alexander W Wray, Brian R Duffy, and Stephen K Wilson. Competitive evaporation of multiple sessile droplets. *Journal of Fluid Mechanics*, 884, 2020.

[49] MA Saxton, D Vella, JP Whiteley, and JM Oliver. Kinetic effects regularize the mass-flux singularity at the contact line of a thin evaporating drop. *Journal of Engineering Mathematics*, 106(1):47–73, 2017.

[50] Noushine Shahidzadeh-Bonn, Salima Rafai, Aza Azouni, and Daniel Bonn. Evaporating droplets. *Journal of Fluid Mechanics*, 549:307–313, 2006.

[51] GJ Dunn, SK Wilson, BR Duffy, S David, and Khellil Sefiane. The strong influence of substrate conductivity on droplet evaporation. *Journal of Fluid Mechanics*, 623:329–351, 2009.

[52] DM Anderson and SH Davis. The spreading of volatile liquid droplets on heated surfaces. *Physics of Fluids*, 7(2):248–265, 1995.

[53] K Sefiane, SK Wilson, S David, GJ Dunn, and BR Duffy. On the effect of the atmosphere on the evaporation of sessile droplets of water. *Physics of fluids*, 21(6):062101, 2009.

[54] FGH Schofield, SK Wilson, D Pritchard, and K Sefiane. The lifetimes of evaporating sessile droplets are significantly extended by strong thermal effects. *Journal of Fluid Mechanics*, 851:231–244, 2018.

[55] C Diddens, Johannes GM Kuerten, CWM Van der Geld, and HMA Wijshoff. Modeling the evaporation of sessile multi-component droplets. *Journal of colloid and interface science*, 487:426–436, 2017.

[56] Amir A Pahlavan, Lisong Yang, Colin D Bain, and Howard A Stone. Evaporation of binary-mixture liquid droplets: The formation of picoliter pancakelike shapes. *Physical review letters*, 127(2):024501, 2021.

[57] James Thomson. Xlii. on certain curious motions observable at the surfaces of wine and other alcoholic liquors. *The London, Edinburgh, and Dublin Philosophical Magazine and Journal of Science*, 10(67):330–333, 1855.

[58] LE Scriven and CV Sternling. The marangoni effects. *Nature*, 187(4733):186–188, 1960.

[59] Carlo Marangoni. *Sull'espansione delle goccie d'un liquido galleggianti sulla superfice di altro liquido.* Fratelli Fusi, 1865.

[60] Dora Pesach and Abraham Marmur. Marangoni effects in the spreading of liquid mixtures on a solid. *Langmuir*, 3(4):519–524, 1987.

[61] DA Nield. Surface tension and buoyancy effects in cellular convection. *Journal of Fluid Mechanics*, 19(3):341–352, 1964.

[62] Abraham D Stroock, Rustem F Ismagilov, Howard A Stone, and George M Whitesides. Fluidic ratchet based on marangoni- bénard convection. *Langmuir*, 19(10):4358–4362, 2003.

[63] Hector Mancini and Diego Maza. Pattern formation without heating in an evaporative convection experiment. *EPL (Europhysics Letters)*, 66(6):812, 2004.

[64] X Fanton and AM Cazabat. Spreading and instabilities induced by a solutal marangoni effect. *Langmuir*, 14(9):2554–2561, 1998.

[65] Pierre Gilles De Gennes. Instabilities during the evaporation of a film: Non-glassy polymer+ volatile solvent. *The European Physical Journal E*, 6(1):421–424, 2001.

[66] Peter Ehrhard and Stephen H Davis. Non-isothermal spreading of liquid drops on horizontal plates. *Journal of Fluid Mechanics*, 229:365–388, 1991.

[67] R Savino, D Paterna, and N Favaloro. Buoyancy and marangoni effects in an evaporating drop. *Journal of thermophysics and heat transfer*, 16(4):562–574, 2002.

[68] Hua Hu and Ronald G Larson. Analysis of the effects of marangoni stresses on the microflow in an evaporating sessile droplet. *Langmuir*, 21(9):3972–3980, 2005.

[69] Mainak Majumder, Clint S Rendall, J Alexander Eukel, James YL Wang, Natnael Behabtu, Cary L Pint, Tzu-Yu Liu, Alvin W Orbaek, Francesca Mirri, Jaewook Nam, et al. Overcoming the "coffee-stain" effect by compositional marangoni-flow-assisted drop-drying. *The Journal of Physical Chemistry B*, 116(22):6536–6542, 2012.

[70] Jungho Park and Jooho Moon. Control of colloidal particle deposit patterns within picoliter droplets ejected by ink-jet printing. *Langmuir*, 22(8):3506–3513, 2006.

[71] Van Nguyen Truskett and Kathleen J Stebe. Influence of surfactants on an evaporating drop: Fluorescence images and particle deposition patterns. *Langmuir*, 19(20):8271–8279, 2003.

[72] Tim Still, Peter J Yunker, and Arjun G Yodh. Surfactant-induced marangoni eddies alter the coffee-rings of evaporating colloidal drops. *Langmuir*, 28(11):4984–4988, 2012.

[73] RT van Gaalen, C Diddens, HMA Wijshoff, and JGM Kuerten. The evaporation of surfactant-laden droplets: A comparison between contact line models. *Journal of colloid and interface science*, 579:888–897, 2020.

[74] RT van Gaalen, C Diddens, HMA Wijshoff, and JGM Kuerten. Marangoni circulation in evaporating droplets in the presence of soluble surfactants. *Journal of colloid and interface science*, 584:622–633, 2021.

[75] RT van Gaalen, HMA Wijshoff, JGM Kuerten, and C Diddens. Competition between thermal and surfactant-induced marangoni flow in evaporating sessile droplets. *Journal of Colloid and Interface Science*, 622:892–903, 2022.

[76] Hyoungsoo Kim, François Boulogne, Eujin Um, Ian Jacobi, Ernie Button, and Howard A Stone. Controlled uniform coating from the interplay of marangoni flows and surface-adsorbed macromolecules. *Physical review letters*, 116(12):124501, 2016.

[77] EL Talbot, A Berson, and CD Bain. Drying and deposition of picolitre droplets of colloidal suspensions in binary solvent mixtures. In *NIP & Digital Fabrication Conference*, volume 2012, pages 420–423. Society for Imaging Science and Technology, 2012.

[78] EL Talbot, A Berson, L Yang, and CD Bain. Internal flows and particle transport inside picoliter droplets of binary solvent mixtures. In *NIP & Digital Fabrication Conference*, volume 2013, pages 307–312. Society for Imaging Science and Technology, 2013.

[79] Emma L Talbot, Huai N Yow, Lisong Yang, Arganthaël Berson, Simon R Biggs, and Colin D Bain. Printing small dots from large drops. *ACS applied materials & interfaces*, 7(6):3782–3790, 2015.

[80] Svante Arrhenius. Über die innere reibung verdünnter wässeriger lösungen. *Zeitschrift für Physikalische Chemie*, 1(1):285–298, 1887.

[81] LaAHN Grunberg and Alfred H Nissan. Mixture law for viscosity. *Nature*, 164(4175):799–800, 1949.

[82] Antje MJ Van den Berg, Antonius WM de Laat, Patrick J Smith, Jolke Perelaer, and Ulrich S Schubert. Geometric control of inkjet printed features using a gelating polymer. *Journal of Materials Chemistry*, 17(7):677–683, 2007.

[83] Kunshan Sun and Srinivasa R Raghavan. Thermogelling aqueous fluids containing low concentrations of pluronic f127 and laponite nanoparticles. *Langmuir*, 26(11):8015–8020, 2010.

[84] Hua Hu and Ronald G Larson. Analysis of the microfluid flow in an evaporating sessile droplet. *Langmuir*, 21(9):3963–3971, 2005.

[85] M Cachile, O Benichou, C Poulard, and AM Cazabat. Evaporating droplets. *Langmuir*, 18(21):8070–8078, 2002.

[86] C Poulard, O Benichou, and AM Cazabat. Freely receding evaporating droplets. *Langmuir*, 19(21):8828–8834, 2003.

[87] N Murisic and L Kondic. Modeling evaporation of sessile drops with moving contact lines. *Physical Review E*, 78(6):065301, 2008.

[88] Robert M Ybarra and Partho Neogi. Dynamic contact angles under evaporation. *The Journal of chemical physics*, 120(12):5755–5760, 2004.

[89] SJS Morris. A phenomenological model for the contact region of an evaporating meniscus on a superheated slab. *Journal of Fluid Mechanics*, 411:59–89, 2000.

[90] Christof Sodtke, Vladimir S Ajaev, and Peter Stephan. Dynamics of volatile liquid droplets on heated surfaces: theory versus experiment. *Journal of Fluid Mechanics*, 610:343–362, 2008.

[91] William E Schiesser. *The numerical method of lines: integration of partial differential equations*. Elsevier, 2012.

[92] MNO Sadiku and CN Obiozor. A simple introduction to the method of lines. *International journal of electrical engineering education*, 37(3):282–296, 2000.

[93] Kara L Maki and Satish Kumar. Fast evaporation of spreading droplets of colloidal suspensions. *Langmuir*, 27(18):11347–11363, 2011.

[94] Jürgen Horbach and Sauro Succi. Lattice boltzmann versus molecular dynamics simulation of nanoscale hydrodynamic flows. *Physical review letters*, 96(22):224503, 2006.

[95] Andrew K Gunstensen, Daniel H Rothman, Stéphane Zaleski, and Gianluigi Zanetti. Lattice boltzmann model of immiscible fluids. *Physical Review A*, 43(8):4320, 1991.

[96] Daniel H Rothman. Cellular-automaton fluids: A model for flow in porous media. *Geophysics*, 53(4):509–518, 1988.

[97] Haibo Huang, Michael Sukop, and Xiyun Lu. Multiphase lattice boltzmann methods: Theory and application. 2015.

[98] Rodrigo Ledesma-Aguilar, Dominic Vella, and Julia M Yeomans. Lattice-boltzmann simulations of droplet evaporation. *Soft Matter*, 10(41):8267–8275, 2014.

[99] Y Yu, Q Li, Chenn Q Zhou, P Zhou, and HJ Yan. Investigation of droplet evaporation on heterogeneous surfaces using a three-dimensional thermal multiphase lattice boltzmann model. *Applied Thermal Engineering*, 127:1346–1354, 2017.

[100] Bortolo Matteo Mognetti, H Kusumaatmaja, and JM Yeomans. Drop dynamics on hydrophobic and superhydrophobic surfaces. *Faraday discussions*, 146:153–165, 2010.

[101] Mahsa Ebrahim, Alfonso Ortega, Nicolas Delbosc, Mark CT Wilson, and Jonathan L Summers. Simulation of the spreading of a gas-propelled micro-droplet upon impact on a dry surface using a lattice-boltzmann approach. *Physics of Fluids*, 29(7):072104, 2017.

[102] Khaled HA Al-Ghaithi, Oliver G Harlen, Nikil Kapur, and Mark CT Wilson. Morphologies and dynamics of micro-droplet impact onto an idealised scratch. *Journal of Fluid Mechanics*, 925, 2021.

[103] Christian Diddens. Detailed finite element method modeling of evaporating multi-component droplets. *Journal of Computational Physics*, 340:670–687, 2017.

[104] Rajneesh Bhardwaj, Jon P Longtin, and Daniel Attinger. Interfacial temperature measurements, high-speed visualization and finite-element simulations of droplet impact and evaporation on a solid surface. *International Journal of Heat and Mass Transfer*, 53(19-20):3733–3744, 2010.

[105] Martin Gielok, Marcus Lopes, Elmar Bonaccurso, and Tatiana Gambaryan-Roisman. Droplet on an elastic substrate: Finite element method coupled with lubrication approximation. *Colloids and Surfaces A: Physicochemical and Engineering Aspects*, 521:13–21, 2017.

[106] R Mollaret, Khellil Sefiane, JRE Christy, and D Veyret. Experimental and numerical investigation of the evaporation into air of a drop on a heated surface. *Chemical Engineering Research and Design*, 82(4):471–480, 2004.

[107] Jochen Alberty, Carsten Carstensen, and Stefan A Funken. Remarks around 50 lines of matlab: short finite element implementation. *Numerical algorithms*, 20(2):117–137, 1999.

[108] Tapan Kumar Pradhan and Pradipta Kumar Panigrahi. Deposition pattern of interacting droplets. *Colloids and Surfaces A: Physicochemical and Engineering Aspects*, 482:562–567, 2015.

[109] Tapan Kumar Pradhan and Pradipta Kumar Panigrahi. Influence of an adjacent droplet on fluid convection inside an evaporating droplet of binary mixture. *Colloids and Surfaces A: Physicochemical and Engineering Aspects*, 500:154–165, 2016.

[110] Florian Carle, Sergey Semenov, Marc Medale, and David Brutin. Contribution of convective transport to evaporation of sessile droplets: empirical model. *International Journal of Thermal Sciences*, 101:35–47, 2016.

[111] Lyle N Long, Michael M Micci, and Brian C Wong. Molecular dynamics simulations of droplet evaporation. *Computer Physics Communications*, 96(2-3):167–172, 1996.

[112] Lorenzo Consolini, Suresh K Aggarwal, and Sohail Murad. A molecular dynamics simulation of droplet evaporation. *International journal of heat and mass transfer*, 46(17):3179–3188, 2003.

[113] S Nishida, D Surblys, Y Yamaguchi, K Kuroda, M Kagawa, T Nakajima, and H Fujimura. Molecular dynamics analysis of multiphase interfaces based on in situ extraction of the pressure distribution of a liquid droplet on a solid surface. *The Journal of chemical physics*, 140(7):074707, 2014.

[114] Jianguo Zhang, Frédéric Leroy, and Florian Müller-Plathe. Evaporation of nanodroplets on heated substrates: a molecular dynamics simulation study. *Langmuir*, 29(31):9770–9782, 2013.

[115] Gary N Coleman and Richard D Sandberg. A primer on direct numerical simulation of turbulence-methods, procedures and guidelines. 2010.

[116] PJ Sáenz, K Sefiane, J Kim, OK Matar, and P Valluri. Evaporation of sessile drops: a three-dimensional approach. *Journal of Fluid Mechanics*, 772:705–739, 2015.

[117] Jonathan Reutzsch, Corine Kieffer-Roth, and Bernhard Weigand. A consistent method for direct numerical simulation of droplet evaporation. *Journal of Computational Physics*, 413:109455, 2020.

[118] Feargus GH Schofield, Alexander W Wray, David Pritchard, and Stephen K Wilson. The shielding effect extends the lifetimes of two-dimensional sessile droplets. *Journal of Engineering Mathematics*, 120(1):89–110, 2020.

[119] KB Kiradjiev, CJW Breward, and IM Griffiths. Surface-tension-and injection-driven spreading of a thin viscous film. *Journal of Fluid Mechanics*, 861:765–795, 2019.

[120] Francois-Marie Raoult. Loi générale des tensions de vapeur des dissolvants. *CR Hebd. Seances Acad. Sci*, 104:1430–1433, 1887.

[121] Christian Diddens, Huanshu Tan, Pengyu Lv, Michel Versluis, JGM Kuerten, Xuehua Zhang, and Detlef Lohse. Evaporating pure, binary and ternary droplets: thermal effects and axial symmetry breaking. *Journal of fluid mechanics*, 823:470–497, 2017.

[122] Xuefeng Xu, Jianbin Luo, and Dan Guo. Criterion for reversal of thermal marangoni flow in drying drops. *Langmuir*, 26(3):1918–1922, 2010.

[123] J. Winkelmann. Diffusion of ethanol (1); air (2): Datasheet from landolt-börnstein - group iv physical chemistry · volume 15a: "gases in gases, liquids and their mixtures" in springermaterials (https://doi.org/10.1007/978-3-540-49718-9_614). Copyright 2007 Springer-Verlag Berlin Heidelberg.

[124] Alexander Klinov and Ivan Anashkin. Diffusion in binary aqueous solutions of alcohols by molecular simulation. *Processes*, 7(12):947, 2019.

[125] Hanneke Gelderblom, Christian Diddens, and Alvaro Marin. Evaporation-driven liquid flow in sessile droplets. *Soft Matter*, 2022.

[126] Alvaro Marin, Robert Liepelt, Massimiliano Rossi, and Christian J Kähler. Surfactant-driven flow transitions in evaporating droplets. *Soft Matter*, 12(5):1593–1600, 2016.

[127] Xingyi Shi, Gerald G Fuller, and Eric SG Shaqfeh. Oscillatory spontaneous dimpling in evaporating curved thin films. *Journal of Fluid Mechanics*, 889, 2020.

[128] Laurent Duchemin and Christophe Josserand. Dimple drainage before the coalescence of a droplet deposited on a smooth substrate. *Proceedings of the National Academy of Sciences*, 117(34):20416–20422, 2020.

[129] Peng Gao, Lei Li, James J Feng, Hang Ding, and Xi-Yun Lu. Film deposition and transition on a partially wetting plate in dip coating. *Journal of Fluid Mechanics*, 791:358–383, 2016.

[130] Jian Qin, Yu-Ting Xia, and Peng Gao. Axisymmetric evolution of gravity-driven thin films on a small sphere. *Journal of Fluid Mechanics*, 907, 2021.

[131] JH Snoeijer, Johanna Ziegler, B Andreotti, M Fermigier, and J Eggers. Thick films of viscous fluid coating a plate withdrawn from a liquid reservoir. *Physical review letters*, 100(24):244502, 2008.

[132] BMS Santos, AGM Ferreira, and IMA Fonseca. Surface and interfacial tensions of the systems water+ n-butyl acetate+ methanol and water+ n-pentyl acetate+ methanol at 303.15 k. *Fluid Phase Equilibria*, 208(1-2):1–21, 2003.

[133] The Dow Chemical Company. *PRIMARY AMYL ACETATE*, 10 2002.

[134] Grant W Smith and Leonard V Sorg. The measurement of boundary tension by the pendant-drop method. i. the aliphatic alcohols. *The Journal of Physical Chemistry*, 45(4):671–681, 1941.

[135] RC Ernst, EE Litkenhous, and JW Spanyer Jr. The physical properties of the ternary system acetone-n-butyl alcohol-water. *The Journal of Physical Chemistry*, 36(3):842–854, 2002.

[136] GC Benson and VT Lam. Surface tensions of binary liquid systems. ii. mixtures of alcohols. *Journal of Colloid and Interface Science*, 38(2):294–301, 1972.

[137] William M Haynes, David R Lide, and Thomas J Bruno. *CRC handbook of chemistry and physics*. CRC press, 2016.

[138] George Karapetsas, Omar K Matar, Prashant Valluri, and Khellil Sefiane. Convective rolls and hydrothermal waves in evaporating sessile drops. *Langmuir*, 28(31):11433–11439, 2012.

[139] AJ Babchin, AL Frenkel, BG Levich, and GI Sivashinsky. Nonlinear saturation of rayleigh–taylor instability in thin films. *The Physics of fluids*, 26(11):3159–3161, 1983.

[140] N Alleborn and H Raszillier. Local perturbation of thin film flow. *Archive of Applied Mechanics*, 73(9):734–751, 2004.

[141] MRE Warner, RV Craster, and OK Matar. Surface patterning via evaporation of ultrathin films containing nanoparticles. *Journal of colloid and interface science*, 267(1):92–110, 2003.

[142] Eric Sultan, Arezki Boudaoud, and Martine Ben Amar. Evaporation of a thin film: diffusion of the vapour and marangoni instabilities. *Journal of Fluid Mechanics*, 543:183–202, 2005.